Pulsed Laser Deposition Growth of Heusler Half-Metallic Thin Films

---

A thesis submitted in partial fulfilment of the

requirements for the Degree

of Master of Science in Physics

in the University of Canterbury

by Chrissy Emeny

University of Canterbury

2014

Abstract

This thesis presents the growth, physical characterisation and magnetic properties of two thin film Heusler alloys, Co_2MnSi and Co_2MnGa, which were deposited on substrates of MgO and GaAs using the technique known as pulsed laser deposition (PLD).

These two materials are classified as half-metallic Heusler alloys, and are predicted to be strongly ferromagnetic at room temperature. These alloys are also predicted to have spin moments 100% polarised in one direction which originates from an energy gap in the minority band at the Fermi level (E_F). These attributes make Co_2MnSi and Co_2MnGa ideal for use in spintronic devices. The properties of half-metallic Heusler alloys are very sensitive to crystal structure disorder, which is detrimental to both the alignment of magnetic moments within the film and the level of spin polarisation. Films ordered in the $L2_1$ crystal structure are required to observe the full potential of the properties associated with half-metallic behaviour.

Growth quality of Co_2MnSi and Co_2MnGa single layer thin films was investigated by varying three main growth parameters: laser fluence, substrate choice and substrate growth temperature. Bi-layer Co_2MnGa thin films were also grown using PLD to determine whether a buffer layer of the same material grown under different conditions improved the deposited crystal structure of the film on top. *In-situ* Reflection High Energy Electron Diffraction (RHEED) imaging, Scanning Electron Microscope (SEM) images, X-ray Diffraction (XRD) and resistivity measurements using a Physical Property Measurement System (PPMS) were techniques used to characterise the physical properties of the thin films such as growth orientation, quality and atomic arrangement of the films' crystalline structure. Overall, PLD was used to successfully deposit Co_2MnSi and Co_2MnGa epitaxial thin films on both MgO and GaAs when a minimum substrate growth temperature of 450°C was chosen. Co_2MnSi thin films required a minimum fluence of 4.5 J/cm² for epitaxial growth whereas the crystal quality of Co_2MnGa did not appear to be very sensitive to variations in fluence. XRD analysis suggested all the films grown in this thesis were arranged in the B2 crystal structure, not $L2_1$.

The general trend of the temperature dependent resistivity of the Co_2MnSi series showed these thin films exhibit ferromagnetic behaviour as the resistivity monotonically increases with temperature. Observing this data with different variations of the temperature dependent resistivity equation confirmed the half-metallic nature of Co_2MnSi.

Investigation of the magnetic properties of Co_2MnSi and Co_2MnGa showed a magnetic hysteresis when the films were swept through an applied magnetic field at a constant temperature. The saturation magnetic moment (M_S) values at 300K decreased relative to values at 10K by 23% for Co_2MnSi and 34% for Co_2MnGa. Alignment disorder of the magnetic moments occurs as a ferromagnetic material approaches the Curie temperature. Co_2MnGa has a lower Curie temperature of 694K than 985K for Co_2MnSi which resulted in a larger decrease in M_S at 300K.

The M_S values of these Heusler alloys were predicted to be 5.07 μ_B/f.u. for Co_2MnSi and 4.07 μ_B/f.u. for Co_2MnGa. The highest M_S values determined from the thin films in this thesis were 4.65±0.83 μ_B/f.u. and 6.02±3.01 μ_B/f.u. for Co_2MnSi and Co_2MnGa respectively on MgO, and 3.54±1.36 μ_B/f.u and 3.60±0.77 μ_B/f.u. for Co_2MnSi and Co_2MnGa respectively on GaAs. Values for Co_2MnSi on MgO agree within uncertainty with the theoretically predicted magnetic moment, whereas Co_2MnSi on GaAs is 3% lower than this value. Values for Co_2MnGa agree for GaAs substrates but not for MgO substrates, this was a direct result of the high uncertainty in the thickness of films deposited on MgO, of up to 50% on films of 20-30nm thickness. For both materials on both types of substrates, there is a strong correlation between high M_S values and a minimum growth temperature of 450°C. Higher fluence was also a factor as thicker films produced more accurate values for M_S.

Including a buffer layer between the substrate and the deposited film in the case of Co_2MnGa films was shown to positively influence the physical properties of the thin film growth. Epitaxial thin films of Co_2MnGa with buffer layers resulted in thin films with lattice parameters closer to the bulk values than the films without buffer layers presented in this thesis. However, the addition of the buffer layer resulted in M_S values lower than those of the optimally prepared single layer films grown at 450°C.

Future work heavily relies on the growth of thicker films. Some of the films examined in this thesis were 10-20nm thick, much thinner than the target of ~ 100nm. In some cases,

the low thickness caused difficulties with determining the properties of the films due to an absence of film peaks from XRD results and a large uncertainty in the thickness determined from Rutherford backscattering (RBS) which resulted in an overestimation of the M_S values. Having a more diverse range of substrate growth temperature and fluence value combinations for each substrate choice would also be beneficial by providing more detail about the optimum growth parameters.

Acknowledgements

First and foremost I would like to thank my three supervisors, Roger Reeves, Simon Granville and Ian Farrell for every moment you contributed to this thesis: whether it was though your enthusiasm while enduring long hours in the labs, the help you gave me to understand the concepts of thin films and Heusler alloys or the tedious hours you all contributed to reviewing, correcting and guiding me through the progress of this thesis. I gratefully appreciate all the opportunities you have presented me over the course of this study.

I would like to thank Helen Devereux and Gary Turner for coming to my aid to find or fix whatever I required during the brief time I spent lurking in the Nanofabrication lab. On the same principle I also thank Callaghan Innovation, the Mac Diarmid Institute and the Department of Physics and Astronomy at Canterbury University.

It goes without saying that I want to thank all the friends and family who helped make this thesis undyingly easier than it would have been alone – especially Pubudu, Simon, Susie, Amber and the Alexs' for all the support, help and necessary distractions leading up to the deadline.

Lastly, to my parents and my better half – Thank you for not only making this possible, but for always being proud of my achievements.

Contents

List of tables

List of figures

Chapter 1

Introduction

Technology dependence in society has led to a complete change in how we live our lives, as computers in the forms of smart phones, tablets and notebooks have become a daily requirement for basic tasks. Rapid industry development to make these devices smaller, lighter and faster has seen the 1965 prediction of Moore's law develop into a realistic trend [1]. The concept that the number of transistors on an integrated circuit board will double every 18 months has led to smaller and more powerful devices, the progress of which is expected to plateau as early as 2015 [1]. Transistors on an atomic scale cannot be shrunk further and will incur a fundamental limit for electronics which sends and processes information via electron charge alone. The integration of new technology is the key to surpassing this limit and improving the existing and future development of computer based devices. The most potential lies in incorporating electron spin as well as charge to send information.

Spin transport electronics, commonly referred to as spintronics, is a new field of technology developed over the past 30 years that can take advantage of a new dimension in the parameter space of electronics. This technology exploits the intrinsic spin of the electron and its associated magnetic moment, as well as using the fundamental electronic charge, to find new applications in solid-state devices [2][6][9].

Electrons are spin ½ fermions, which occupy one of two states, spin-up or spin-down. The definition of electron spin is based on the alignment of the spin direction relative to a reference such as an applied magnetic field or the magnetised orientation of a ferromagnetic film [2].

The field of spintronics opens the pathway for a new generation of devices by combining existing microelectronics with spin-dependent effects that arise from the interaction between the magnetic properties and charge carriers in a material. By adding the spin degree of freedom, applications in spintronics aim to achieve modified versions of existing

commercial devices such as spin-FETs (field effect transistors), spin-LEDs (light-emitting diodes) and spin-RTDs (resonant tunnelling diodes) [3].

Presently available magneto-electronics devices already taking advantage of spin properties include: Giant magneto-resistance (GMR) read heads for computer storage disks which operate at 300K, the effect of tunnelling magneto-resistance (TMR) in magnetic tunnel junctions (MTJ) used for non-volatile magnetic random access memory and magnetic sensors [4].

GMR is a quantum mechanical magneto-resistance effect in thin films due to alternating layers of ferromagnetic and non-magnetic conductive layers which cause the electrical resistance of the material to change relative to the magnetization alignment of the ferromagnetic layers. TMR is a magneto-resistive effect which occurs in magnetic tunnel junctions where two ferromagnets are separated by a thin insulating layer. Depending on the magnetisation alignment, electrons can tunnel from one ferromagnet to the other [2].

Magnetic sensors function by utilising a range of different spintronic effects such as GMR or TMR. Some possible uses of magnetic sensors are: the remote detection of electric fields, as solid state compasses, for metal detection and non-destructive testing such as finding flaws in material structures using eddy currents.

It is desirable for spintronic devices to be based largely on semiconductors as they will be able to form heterostructures with existing semiconductors which will allow them to easily integrate into present circuit technologies [2][3][12]. Spin polarised current injectors are a key component of a spintronic device. When conventional electrical current with no preferred spin orientation is passed through a sufficiently thick magnetic layer, the current becomes polarised with one dominant spin alignment. Such a magnetic layer which contacts a semiconductor is able to operate as a spin injector, passing spin polarised current into the semiconductor. In order to utilise both the charge and the spin of the electron, devices need to transport spin polarised current into a non-ferromagnetic layer without degrading the degree of spin polarisation across the interface [2].

This thesis presents the growth and analysis of a series of Co_2MnSi and Co_2MnGa thin films, two materials with promise to form advanced magnetic sensors or as spin

injectors[2][6][8][11]. Both are classified as half-metallic ferromagnets from a family known as Heusler alloys [4]. These materials exhibit up to 100% spin polarisation at the Fermi level when ordered in an $L2_1$ crystal structure [4][5][9][12]. The nature of the electronic bands in this particular structure is such that the electron spin orientation in one band direction is dominant, leaving the other band direction completely empty [4]. Overall this effect causes one of the spin band directions to be metallic while the other is insulating [5]. Heusler alloys are ideal for use in spintronics as the spin orientation can be clearly defined in one direction, and a material with such a very high spin polarisation is able to make GMR or TMR based magnetic sensors with very high sensitivity. Half-metallic ferromagnetic materials are unique since usually the *s* and *p*-type valence electrons contribute to both spin directions at the Fermi level [6].

Pulsed laser deposition was chosen as the most suitable method of producing thin films of Co_2MnSi and Co_2MnGa on lattice matched substrates to preserve the half-metallic ferromagnetic properties of these materials. Substrate choice, growth temperature and laser fluence were varied in order to produce high quality films that maintained the magnetic properties associated with 100% spin polarisation when the thin films are ordered in the $L2_1$ crystal structure.

In chapter 2 the background of Heusler alloys and the properties of the two materials Co_2MnSi and Co_2MnGa are discussed in detail. The experimental procedures and theory used to produce and characterise these thin films are provided in chapter 3. Chapter 4 presents a discussion of the physical quality of the film structure, the magnetisation results and resistivities of a range of single layer Co_2MnSi thin films produced by PLD by varying fluence, substrate choice and substrate temperature. Lastly, in chapter 5 the physical quality of the film structure and magnetisation results of a range of Co_2MnGa thin films produced by PLD using different growth parameters are discussed. These films present a variation of single layer growth and bi-layer growth which includes a buffer layer of Co_2MnGa between the film and the substrate.

Chapter 2

Background

2.1 Heusler alloys

Heusler alloys are a unique family of intermetallic compounds discovered a century ago by German engineer and chemist, Friedrich Heusler [8]. Some of these alloys were found to possess strong ferromagnetic properties [7][8]. Possible Heusler alloy combinations are shown in fig 2.1.

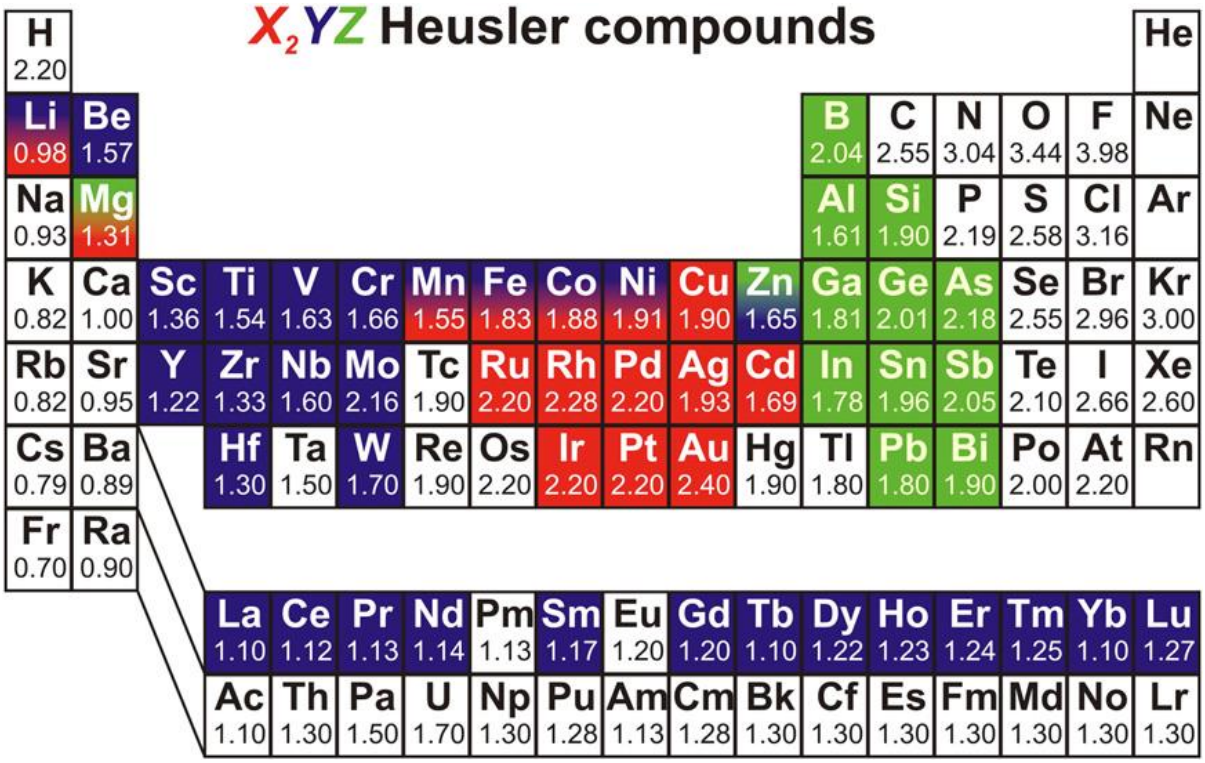

Fig 2.1: Possible Heusler alloy combinations [8].

These alloys are defined by the general formula X_2YZ: The X and Y components are elements of the transition metal group (i.e.: X = Cu, Co, Ni, and Y = Mn, Fe, V) and the Z component is selected from the group III-V elements (i.e.: Z = Al, Ge, Si, Ga, Sn, Sb) as shown in fig 2.1. The desired crystallographic structure with the best magnetic property is the $L2_1$ ordered

phase with the cubic unit cell consisting of four interpenetrating fcc sub-lattices [3][11]. Aligned along the corners in the [111] direction, each sub-lattice is occupied by only one atomic species i.e., Co, Mn, Co and Si/Ga [13] as shown in fig 2.2. In the resulting structure each atom has an eightfold bcc nearest neighbour coordination with highly symmetric site occupation. Due to the freedom of many possible element compositions, Heusler alloys can be exploited to develop new materials with superior physical properties such as improved thermal conductivity, electrical resistivity, heat capacity and magnetic properties [9].

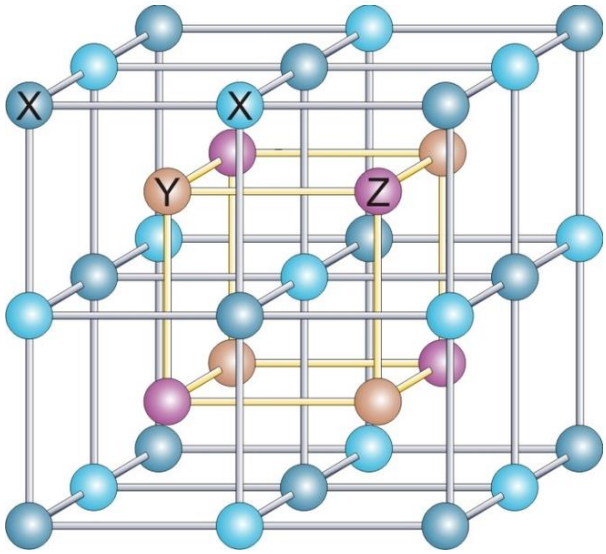

Fig 2.2: Basic $L2_1$ structure of a Heusler alloy corresponding to the general formula X_2YZ. The unit cell consists of interposed fcc lattices with 4 atoms as the basis: X exists at (0 0 0) and (½ ½ ½), Y and Z exist alternatively at (¼ ¼ ¼) and (¾ ¾ ¾).

Some Heusler alloys are expected from theoretical calculations to be half-metals which are materials with 100% spin polarisation at the Fermi level (E_F) [4][5][9]. The nature of the electronic bands for the density of states at the Fermi level in this particular structure is such that the electron spin orientation in one band direction is dominant, leaving the other band direction completely empty [4]. Fig 2.3 shows the density of states for a normal metal consists of random spin orientations and there is no energy gap at the E_F, whereas for a semiconductor a gap exists. In the case of a half-metallic ferromagnet, the majority spin band (in this case the spin-up band) shows typical metallic behaviour whereas the minority band (in this case the spin-down band) shows semiconducting behaviour with a gap at E_F. Overall this effect causes one of the spin band directions to be metallic while the other is

insulating [5], allowing for the spin orientation to be clearly defined in one direction, spin-up or spin-down. Half-metallic ferromagnets are considered to be hybrids between metals and semiconductors and are unique since usually the s and p-type valence electrons contribute to both spin directions at the Fermi level [6]. One way to notice the effects of a single dominant spin direction in a material is by measuring the thermal variation of its resistivity at low temperature [11].

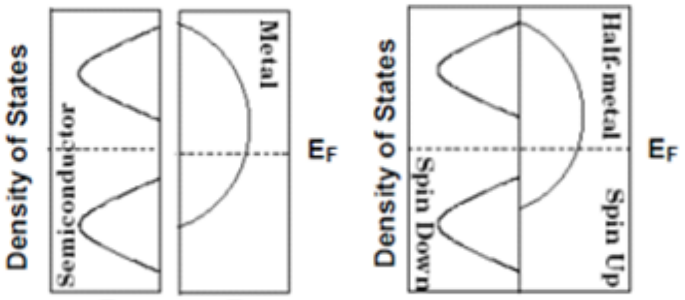

Fig 2.3: Schematic representation of the density of states for a half-metallic ferromagnet with respect to normal metals and semiconductors [3]. The sides of each diagram represent the two different spin-resolved electron densities of states.

Ferromagnetism in Heusler alloys is extremely complex and not yet completely understood [15]. Co_2MnZ Heusler alloys in particular are quite sensitive to atomic site disorder and there are two other competing crystallographic structures with less well ordered site occupancy [16]. The B2 structure exists where there is random occupation of the Y and Z sub-lattice sites, and the A2 structure exists when there is random occupation of all four sub-lattices [8][16].

The correlation between structural site order and ferromagnetic order can be described in terms of the local Heisenberg model with nearest neighbour and next-nearest-neighbour exchange interactions [15]. For all Co-based Heusler half-metals the situation is very complex. There are three magnetic atoms in each formula unit. The interactions which affect half-metallic-behaviour and ferromagnetism are the Mn-Mn exchange interaction, and ferromagnetic Co-Co and Co-Mn interactions [10][17][18]. Site disorder in these phases leads to non-ferromagnetic states. In a perfectly ordered $L2_1$ structure there are no Mn-Mn nearest neighbours and the strongest exchange interaction in the unit cell is a ferromagnetic next-neighbour-superexchange across the Co orbitals. If ordered as a B2 structure, Mn-Mn nearest neighbours would exist, and the very strong Mn-Mn anti-

ferromagnetic interactions would compete with ferromagnetic superexchange interactions [10][15].

The $L2_1$ structure is also responsible for the high Curie temperatures of Heusler alloys which can be on the order of 900K (fig 2.4). A high Curie temperature is very desirable as the temperature dependence of spin polarisation scales with the Curie temperature. A low Curie temperature would result in only a marginal fraction of full spin polarisation at room temperature, which is the operating temperature environment for many electronic devices [9][10].

The expected properties of Heusler alloys can be estimated by counting the number of valence electrons of the X_2YZ combination rather than the constituent elements. In particular, half-metallic Heusler alloys follow the Slater-Pauling rule, where the magnetic moment of the material scales linearly with the number of valence electrons (fig 2.4) [12].

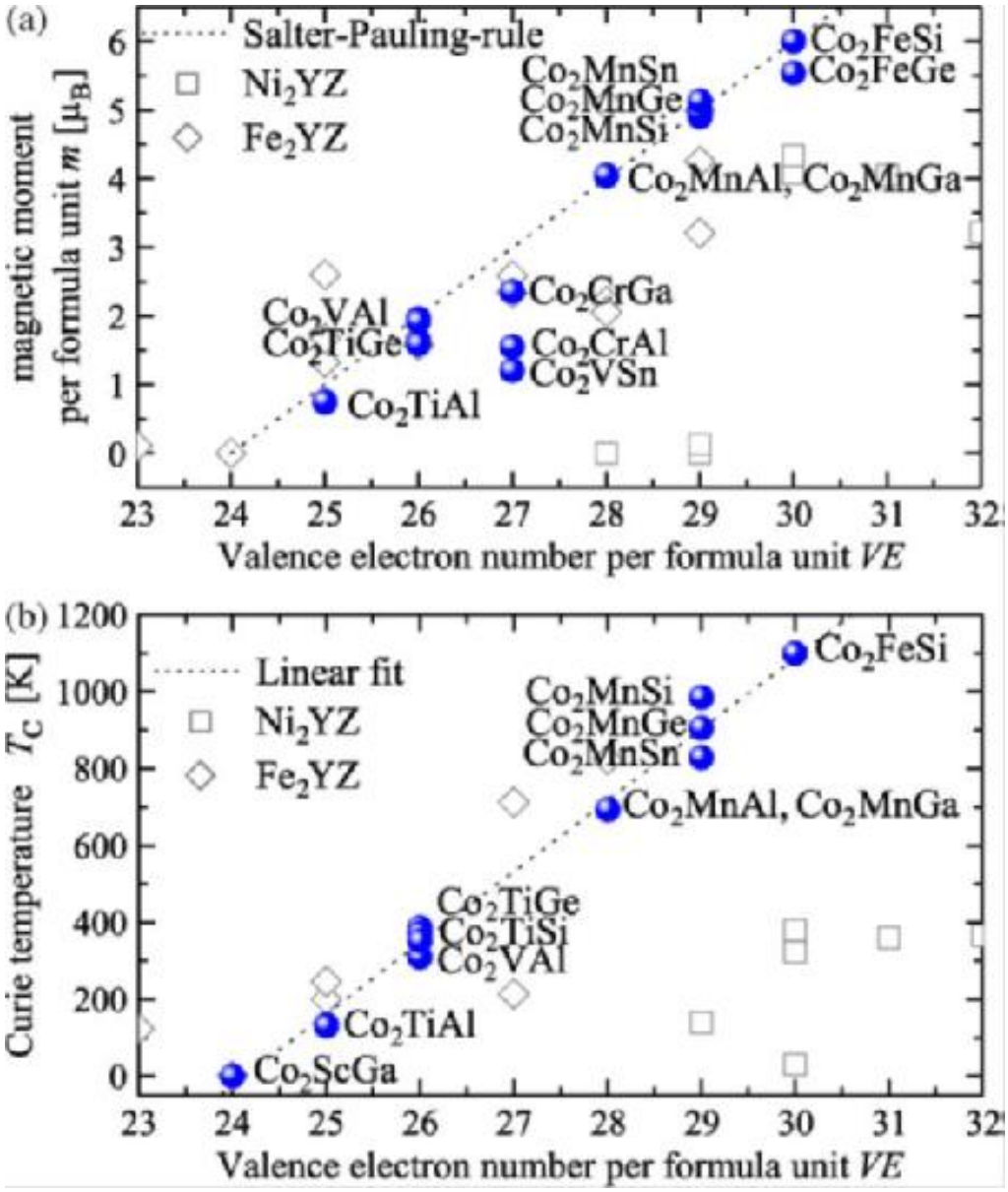

Fig 2.4: [12] (a) Demonstrates the relationship between theoretical saturation magnetic moment of Heusler compounds and the total number of valence electrons in each Heusler alloy. The Slater-Pauling rule is demonstrated in (b) and relates the linear temperature dependence of the Curie temperature to the valence electron count.

2.2 Cobalt manganese silicon, Co_2MnSi

As previously mentioned in section 2.1, the structure of Co_2MnSi consists of four interposed face-centred-cubic (fcc) sub-lattices in an $L2_1$ crystal structure (fig 2.5).

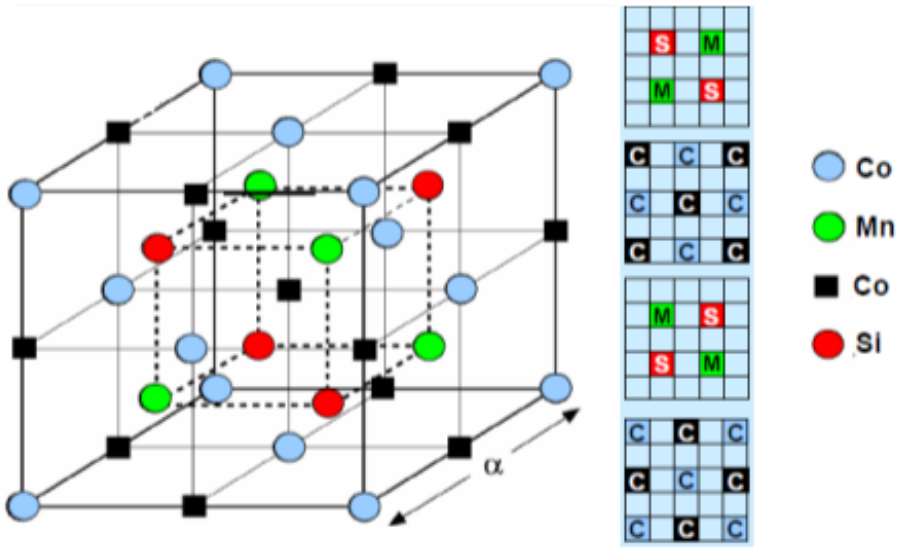

Fig 2.5: Crystal arrangement of the Co, Mn and Si components in Co_2MnSi. The side panel shows the atomic population of the (0 0 0) and (½ ½ ½) planes of Co atoms, and the (¼ ¼ ¼) and (¾ ¾ ¾) planes of alternating Mn and Si atoms.

Co_2MnSi possesses the highest Curie temperature of the Co_2MnZ series at 985K [10]. This material would also exhibit the strongest spin polarisation of the series at room temperature, making Co_2MnSi the best candidate for TMR devices or polarised spin current injectors. The Slater-Pauling rule predicts the magnetic moment to be 5.07μ_B/f.u. [10][12]. Experimentally this has been achieved and values varying from 5.10 - 4.95 μ_B/f.u. have been published [9][10][11].

In a half-metallic ferromagnet, an energy gap exists in the minority spin band at the Fermi energy shown in fig 2.3. Co_2MnSi is predicted to have a large minority band energy gap ~0.4 eV [9][13].

The crystal structure and lattice matching of Co_2MnSi relates well to many semiconductors such as GaAs and Si (Table 2.1), showing it is possible to integrate Co_2MnSi into present semiconductor devices as a spin injector.

The probable growth orientation of Co_2MnSi on any substrate will tend to align with the least strained orientation. Choosing a well lattice matched substrate is important to achieve a thin film which deposits epitaxially relative to the substrate. Given that the lattice mismatch between (100) orientated MgO and Co_2MnSi is on the order of 25%, the deposited film is more likely to align with the (101) crystal plane of MgO (fig 2.6) which has an atomic spacing of 5.957Å and corresponds to a smaller lattice mismatch of 5%.

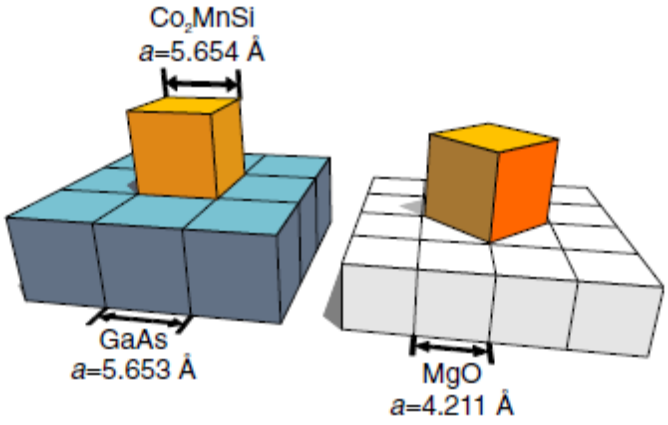

Fig 2.6: [12] Epitaxial preferred deposition orientation of Co_2MnSi thin films on GaAs and MgO. The left image is aligned with GaAs (100), and the right is with MgO (101).

2.3 Cobalt manganese gallium, Co_2MnGa

The structure of Co_2MnGa is identical to Co_2MnSi and consists of four interposed face-centred-cubic (fcc) sub-lattices in an $L2_1$ crystal structure where the previous Si atoms are now replaced with Ga (fig 2.7).

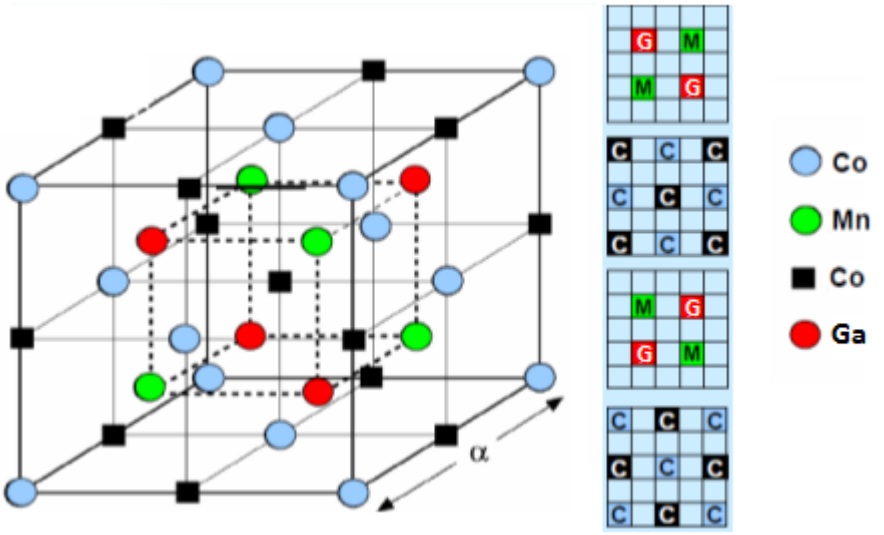

Fig 2.7: Crystal arrangement of the Co, Mn and Ga components in Co_2MnGa. The side panel shows the atomic population of the (0 0 0) and (½ ½ ½) planes of Co atoms, and the (¼ ¼ ¼) and (¾ ¾ ¾) planes of alternating Mn and Ga atoms.

There is ambiguity in published papers as to whether Co_2MnGa should be defined as having half-metallic behaviour [10][12][20]. When comparing Co_2MnGa to Co_2MnSi in fig 2.4, the Curie temperature is often considered when determining if 100% spin polarisation will be present at room temperature given that spin polarisation degrades as the material temperature approaches the Curie temperature. However, Curie temperature is not the main factor when determining half-metallicity as Co_2MnSn is considered to not be a half-metal [19] despite its high Curie temperature (fig 2.4). Theoretical evidence of the density of states at E_F suggests that Co_2MnGa meets the borderline requirements of being a half-metallic Heusler alloy [20]. There are conflicting papers which state without evidence that Co_2MnGa both is and is not half-metallic [10][12][13] [14][20].

Given that Co_2MnGa has the same structure as Co_2MnSi, they have very similar properties due to the ordering of Mn and Co lattice sites [10]. However Co_2MnGa is of a different elemental series and has a 30% lower Curie temperature of 694K [10]. Despite this large difference Co_2MnGa still has a relatively large predicted magnetic moment of $4.06\mu_B$/f.u. [12] (fig 2.4), which has been measured in experiments as 3.2 – 3.5 μ_B/f.u. [10][12][20][21], and a higher theoretical energy gap in the minor electron states near the Fermi level of 0.8eV [13].

The lattice mismatch of Co_2MnGa to the previously mentioned semiconductors, GaAs and Si (Table 2) is slightly higher than for Co_2MnSi, especially in GaAs. Minimising the lattice mismatch is crucial for the integration of these materials into common existing semiconductor devices. Having a larger lattice mismatch can produce varying strain between the two materials which can be detrimental to some films while enhancing the properties of others. Thin films typically do not have the same high crystalline quality that can be achieved in bulk materials due to the smaller volume of the stoichiometric film relative to atomic defects, and as such, thin films do not always have the same properties as their bulk counterparts. Although the 100% spin polarisation of half-metallic Heusler alloys exists due to the $L2_1$ structure of the material, slight lattice defects which result in an atomic spacing which is not identical to the bulk will not necessarily inhibit the ordering of a $L2_1$ structure from forming, but they may degrade some properties such as the value of the magnetic moment.

Given that Co_2MnGa also has a large lattice mismatch with MgO along the (100) plane, the film most likely will align with the (101) plane of the substrate (fig. 2.6) with an improved lattice mismatch of only 3% relative to Co_2MnSi.

Atomic spacing of possible lattice matched substrates (Å) [10]		Lattice mismatch (%) where Co_2MnSi: a = 5.654Å [10]	Lattice mismatch (%) where Co_2MnGa: a = 5.77Å [10]
Si (100)	5.431	4%	6%
MgO (100)	4.212	25%	27%
MgO (101)	5.957	5%	3%
GaAs (100)	5.653	0.02%	2%

Table 2.1: Comparison of possible lattice matched substrates relative to Co_2MnGa and Co_2MnSi.

Chapter 3

Experimental background and details

3.1 Pulsed Laser Deposition (PLD)

3.1.1 Technique and motivation:

PLD is a relatively simple technique that can reproduce complex bulk target materials into thin films that are stoichiometrically accurate, with smooth surface morphology that possess a high quality crystalline structure. The first notable application of PLD was the successful stoichiometric thin film growth of the complex high temperature superconductor, Y-Ba-Cu-O in 1987 [22], which was a material considered too complex to be produced by existing methods at that time. The consistency in stoichiometry of films grown using PLD is a direct result of the highly non-equilibrium nature of short-pulse laser ablation [23]. The rate of heating and cooling processes in the target material during growth are on shorter timescales than the phase separation of the bulk material, which produces thin films with higher levels of crystallographic and chemical purity and makes PLD a powerful technique for investigating properties of a material to a high degree of accuracy [23].

PLD growth takes place in a vacuum chamber. A high energy pulsed laser beam is focussed through a high transmission laser window onto a rotating target where it ablates the surface of the material. The target absorbs the laser energy, causing excitation of the surface atoms. This converts the majority of the beam energy into kinetic energy to eject the material as a plume of ionised particles. The system geometry is chosen such that the incident laser angle and the kinetic energy of the beam direct the ejected plume towards a growth template known as a substrate. The substrate is heated which allows the atoms to move and relax onto the surface to form a thin atomic layer which will have the same orientation as the substrate under suitable conditions.

The best quality PLD is performed under high vacuum (HV) to avoid having the ejected material impact gas molecules such as nitrides, oxides and water vapour in the growth environment. Such impacts would cause the ejected material to scatter away from the substrate and in some circumstances, cause impurities in the film.

The main disadvantage of PLD that makes the technique less desirable for commercial applications is the small volume of emitted material in the plume which leads to low area coverage of the deposited film. An issue which is not unique to PLD but can also have a negative impact on film production is the creation of particulates. Particulates are more apparent when growing at a high fluence.

Particulates are large clusters of molten material that can be ejected when the laser pulse strikes the target. High fluence can result in a heavily particulated film whereas a low fluence can result in no surface particulates. These clusters of material tend to be due to previously molten material in the channel of the ablation ring that has re-solidified into more fragile structures. The clusters travel to the substrate with the plume and settle on top of the deposited layer of film. Low fluence does incur low growth rate which is undesirable when creating films on the order of ~100nm, but it is easily compensated for by increasing growth time. A low deposition rate technique known as Eclipse PLD is another method which reduces film particulates during growth. The large particulates can be blocked by putting an obstacle in the direct path from the plume origin to the substrate, eclipsing the plume. An ambient background gas is introduced into the chamber which allows the small clusters, atoms, and ions to diffuse around the eclipsing object and collect on the substrate reducing the population of particulates on the film surface [24]. The eclipse method was not used for samples grown in this thesis as surface particulates were not an issue when investigating the quality of film growth.

The plume of ejected material is generally conical in shape and emitted normal to the target surface. This shape can result in low area coverage of the deposited film as the edge of the plume contains the least concentration of material relative to the centre. The varying concentration distribution of the ejected material manifests as a film thickness variation that is thinnest in regions furthest from the plume centre. This issue is reduced in this thesis by using small 0.5 x 5 x 10 mm substrates which are aligned centrally within the plume.

More sophisticated PLD systems raster the laser spot across the target in order to steer the plume over a larger area to produce a larger film.

Other techniques that could have been considered for the growth of Heusler thin films from literature are molecular beam epitaxy (MBE) and radio frequency (RF) sputtering. MBE requires molten material to be beamed towards the substrate using effusion cells with shutters to control the flux of the material. This technique is limited to materials with low melting points and deposits material at a slower rate than PLD. There is a higher probability of producing non-stoichiometric films as the individual flux of each constituent of the material needs to be controlled. RF sputtering is simply PLD without the laser. Atoms are ejected from the target material by bombardment with an ionised gas. The ablated target ions are directed toward a heated substrate, which form an epitaxial thin film. A radio frequency source is used to allow non-conductive material to be produced as thin films by reducing charge build-up of the insulating target. Magnets can be placed near the target to concentrate the plasma and enhance sputtering. However stray magnetic fields produced by ferromagnetic targets have been found to disturb the sputtering process.

PLD is preferred to these methods as bulk stoichiometric Co_2MnSi and Co_2MnGa targets can easily be replicated as epitaxial thin films in a short timeframe of this work by varying three easily controlled parameters: a lattice matched substrate, laser fluence and substrate growth temperature. A HV growth environment reduces the probability of defects in the film which degrade the properties of the material. The film thickness can be easily controlled by increasing the length of the growth time, as very thin films dramatically increase small errors affecting the accuracy of the sample analysis. The PLD setup used to grow the thin films investigated in this thesis is an ultra-high vacuum (UHV) chamber based at Canterbury University in the Department of Physics and Astronomy which operates at average chamber pressure of ~10^{-7} Torr. The chamber includes an *in-situ* RHEED system and allows the substrate temperature to be set as high as 900°C. The UHV environment will greatly reduce the concentration of impurities which are detrimental to the formation of the $L2_1$ crystal structure required for Co_2MnSi and Co_2MnGa thin films to reproduce magnetic moments similar to bulk values.

3.1.2 Experimental conditions

The UHV chamber is comprised of two sections. A small volume load lock which is used to insert and remove samples and targets from the system using a transfer arm (fig 3.1). Secondly a large volume main growth chamber which houses a six target carousel for the growth of multilayer films. The target stage can be varied in height to get the optimum target to substrate distance. A column located directly above the target stage holds the substrate and can be varied in height to alter the distance from the target and optimise the RHEED beam grazing angle. A shutter is mounted just below the substrate holder column and protects the substrate from ablated material while aligning the laser spot and pre-ablating the target. A heater with an upper limit of 900°C is located behind the substrate holder. The following elements are highlighted in the close-up of the main chamber shown in fig 3.2.

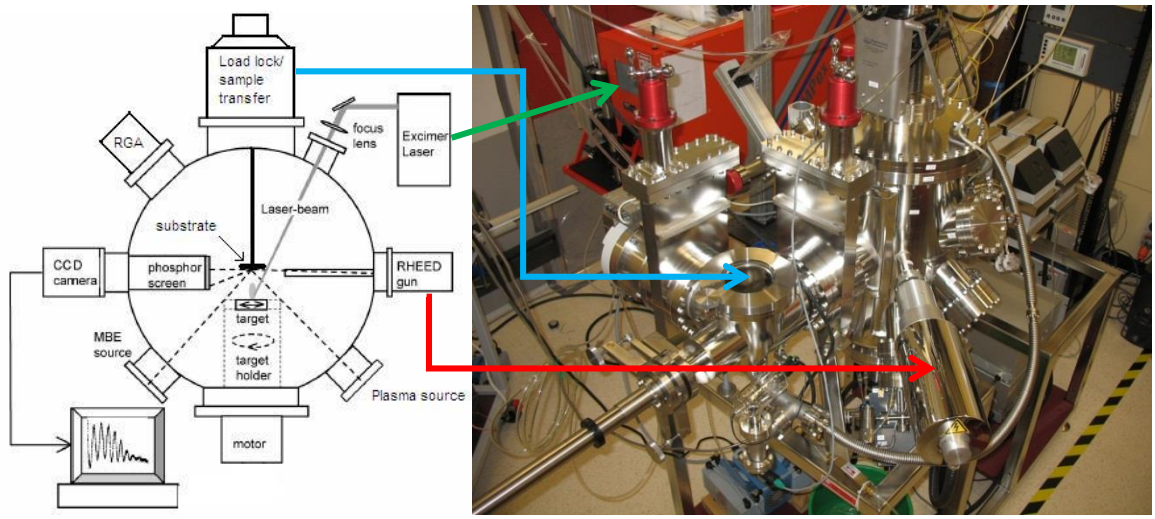

Fig 3.1: Schematic diagram and photograph of the UHV PLD system [23] when orientated from above. Coloured lines are inserted to identify system elements relevant to the growth techniques used in this thesis.

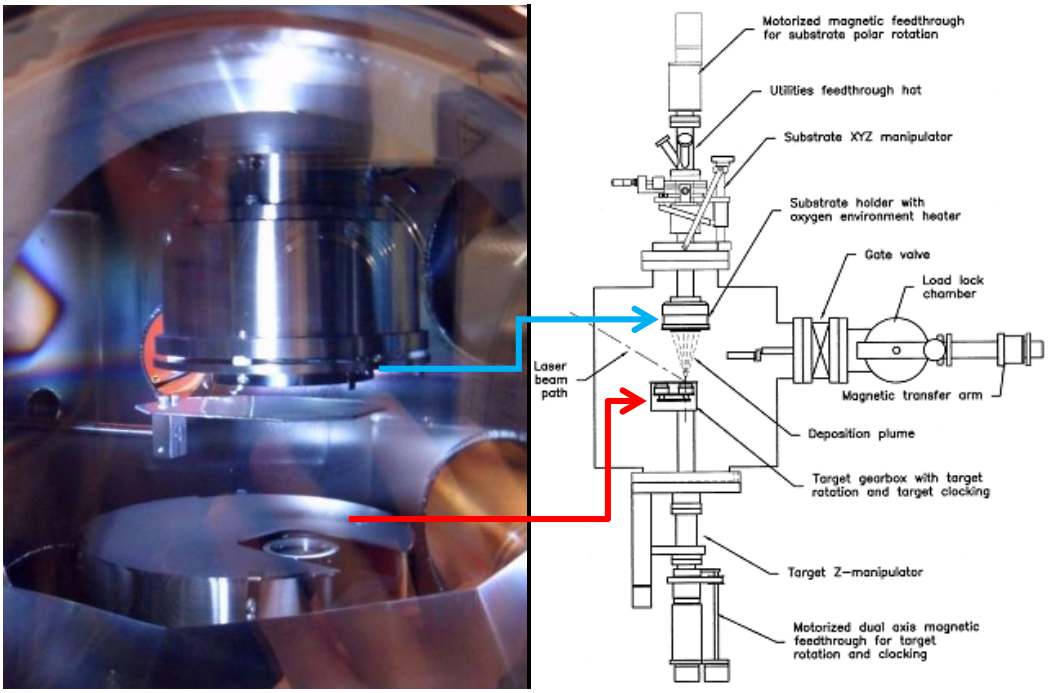

Fig 3.2: Schematic diagram of the UHV PLD system when vertically orientated [25]. The photograph is taken through one of three chamber windows and clearly shows the stage with the target holder below, the substrate holding column above and the shutter between them.

The excitation source used to ablate the Heusler targets was a Lambda Physik Compex 205 (KrF) excimer laser which was directed toward the chamber window by four mirrors. The laser emits 25ns pulses at a UV wavelength of 248nm up to 300mJ. The pulse frequency for the growth was standardised to 10Hz. A high UV transmission plano-convex quartz lens with a 50cm focal length was used to focus the square beam of the laser onto the target in the chamber through a laser window with a known transmission.

The average chamber pressure of ~10^{-7} Torr (where 760 Torr is ~1 standard atm) was maintained by using two separate pumping systems. An ion pump directly connected to the main chamber achieves a pressure below ~10^{-8} Torr when the gate value to the load lock is closed. During growth, the gate value connecting the load lock and the main chamber is open. Under these conditions the ion pump is closed to avoid coating the pump with ablated material, and a turbopump attached to the load lock is used to maintain the vacuum of the main chamber and the load lock.

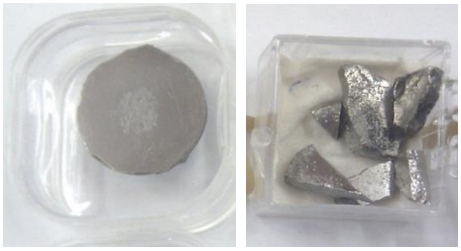

Fig 3.3: Images of the targets used in to produce the thin films in this thesis. The left image is the Co_2MnGa target with dimensions ~ϕ22mm x ~5mm. The right image is the Co_2MnSi target, which is shown to scale relative to the Co_2MnGa target, and was accidentally shattered into six pieces before this series of films were grown.

The targets used in the system were provided by Dr Cristiana Grigorescu of the Romanian National Institute of Research and Development in Optoelectronics. Unfortunately the Co_2MnSi target was fragmented and had to be arranged in the target carousel in such a way that the fragments did not move when rotated during growth and the largest piece was set in the centre of the target holder and used as the ablation source.

Single side polished GaAs (100) and MgO (100) substrates produced by MTI Corp were chosen as the latticed matched substrates. MgO (100) was factory cleaved in dimensions of 0.5 x 5 x 10 mm. The GaAs (100) substrates were factory cleaved in dimensions of 0.5 x 10 x 10 mm and were then hand cleaved into two 0.5 x ~5 x 10mm halves in the PLD growth lab at Canterbury University

3.1.3 Sample preparation and growth:

All sample preparation takes place in a cleanroom with a positive pressure atmosphere while dressed in protective clothing to reduce sample contamination.

MTI Corp substrates were cleaned prior to growth using a three step wash in an ultrasonic bath. Solvents used in the following order were: trichloroethylene, acetone and methanol for ten minutes each.

Nitrogen gas was used to dry the substrate surface to reduce solvent residue before placing the unpolished face onto a molybdenum (Mo) plate heated to 150°C and spread with a thin

layer of molten indium tin (InSn). Mo is suitable for high temperature growth as the material has a very low vapour pressure with increasing temperature which stops the material from emitting Mo atoms that would contaminate the film. The thin layer of indium tin also possesses a low vapour pressure and is molten above temperatures of 117°C. This layer acts as a thermal contact to the Mo plate while holding the substrate in place by surface tension alone.

The Mo plate is secured onto a shuriken style mounting disk by three pins and is turned clockwise to lock in place on the transfer arm with the substrate pointing downwards. When the transfer arm enters the main chamber, the central column is lowered onto the transfer arm and counter-clockwise twists the mounting disk to lock the disk onto the main column.

Before growth, the chamber undergoes an outgassing process with the substrate at 800°C while monitored by a residual gas analyser (RGA). The RGA is a mass spectrometer used to determine the concentration of elements present in the chamber. This outgassing process evaporates unwanted impurities in the substrate and reduces water vapour in the chamber. When the RGA indicates the concentration of water vapour present in the chamber has decreased to be equal to the concentration of hydrogen the outgassing procedure is complete. This process can take between 1-2 hours. Hydrogen is always present in the growth environment, the size of the element is sufficiently small enough to bypass the vacuum seals of the chamber.

The target is always pre-ablated before growth for an average of 5 minutes using a laser energy of 200mJ at 20Hz, and the pre-growth substrate is observed using RHEED. By rotating the substrate through 360° and viewing all possible substrate orientation images, the best image parallel to the RHEED beam which showed the (100) substrate orientation was selected to be monitored during growth. Growth was initialised by opening the shutter and ended by turning off the laser. *In-situ* RHEED images were taken during the growth process to document changes in the film and post growth to re-investigate different orientations of the sample over 360°.

Growth parameters such as stage and column height, substrate choice, growth temperature and laser fluence for each sample grown in the two Heusler alloy series are tabulated at the beginning of chapter 4 for Co_2MnSi and chapter 5 for Co_2MnGa.

The samples in this thesis are labelled using the format PLDX_Y, where X represents the unique substrate and film combination and Y is the growth number of that particular combination series, i.e: for PLD105_05 the substrate and film combination is Co_2MnSi grown on MgO, and the sample is the 5^{th} film grown in this series.

3.2 Reflection High-Energy Electron Diffraction (RHEED)

RHEED is a technique used to characterize crystalline materials by gathering information from the top few atomic surface layers of the sample only, which distinguishes this method from other material characterization methods that also rely on diffraction of high-energy electrons.

A RHEED system requires an electron source (gun), photoluminescent detector screen and a sample with a smooth surface. Tungsten filaments are the primary electron source for the electron gun of most RHEED systems due to the low work function of tungsten. In a typical RHEED setup, the tungsten filament is the cathode and a positively biased anode draws electrons from the tip of the tungsten filament. Phosphor screens exhibit luminescence and are widely used as detectors. These detectors emit green light from areas where electrons hit their surface and CCD cameras are used to capture the patterns. The sample surface must be extremely clean for high resolution RHEED images as contaminants on the sample surface interfere with the electron beam and degrade the quality of the RHEED pattern. Because gas molecules diffract electrons and affect the quality of the electron gun, RHEED experiments are performed under vacuum. As such the vacuum conditions limit the types of materials and processes that can be monitored in situ with RHEED.

The electron gun generates a beam of electrons which graze the sample surface at a very small angle, such as ~3° for the system at Canterbury University. Incident electrons only

diffract from atoms at the surface of the sample as they have very limited penetration ability and can escape depths of a few nm [26]. Diffracted electrons interfere constructively at specific angles to form regular patterns on the detector according to the position of atoms on the sample surface. Two types of diffraction contribute to RHEED patterns. Some incident electrons undergo kinematic scattering, which is a single, elastic scattering event at the crystal surface. These electrons account for the high intensity spots and rings common to RHEED patterns as shown in Fig: 3.4 which will be later discussed in section 3.2.1.

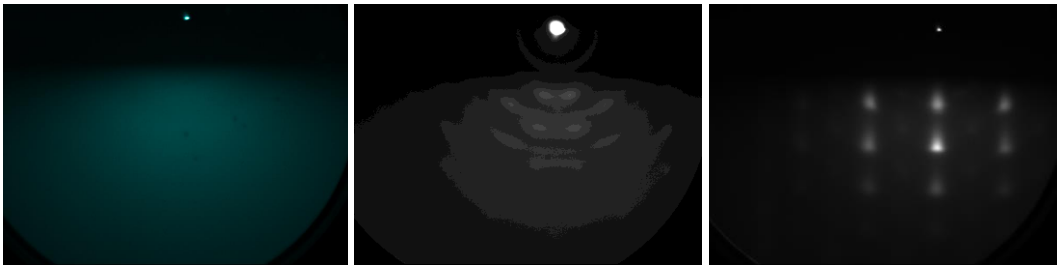

Fig 3.4: (left to right) an amorphous film, a polycrystalline film and a film with high intensity spots which is due to 3D growth.

Dynamic scattering occurs when electrons undergo multiple diffraction events in the crystal and lose some of their energy due to interactions with the sample. If long range order exists in the crystal structure, some inelastically scattered electrons penetrate the film crystal structure and fulfil Bragg diffraction conditions. These electrons reach the detector and cause diffraction lines called Kikuchi lines which connect the intense diffraction points on a RHEED pattern caused by kinematic scattered electrons.

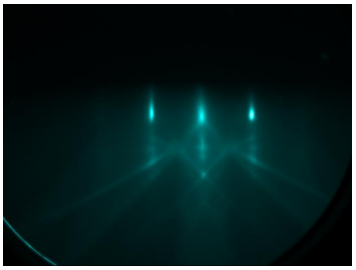

Fig 3.5: Diagonal intersecting Kikuchi lines on RHEED image of an MgO substrate.

The RHEED system mounted on the UHV chamber at Canterbury University consists of a RHEED gun from STAIB instruments. The current and voltage are set to ~1.3A at 20kV for

RHEED images to be visible during growth. These images are captured using a CCD camera with 656x495 pixel resolution.

3.2.1 Understanding RHEED images:

There are four basic types of film growth: amorphous growth, polycrystalline growth, 3D growth (Fig 3.4) and epitaxial growth (Fig 3.6).

An amorphous sample is a non-crystalline film that lacks the repeating order characteristic of a crystal. As such there is no RHEED image as the conditions for diffraction cannot be satisfied. A polycrystalline film is composed of many crystallites, also referred to as grains, of varying size and orientation. The variation in direction can be random or directed in a particular orientation which does not match the substrate template, and results in semi-circular diffraction patterns in RHEED images.

The structure of 3D growth and epitaxial growth are closely related. 3D film growth is where an island of material forms on the surface and is subsequently covered by another island of material [3]. This type of growth causes voids in the surface layer, known as pits, to form and results in a rough surface which is represented by spot features in RHEED images. All films begin with 3D growth.

Epitaxial growth occurs when the islands of material form separately. As the population of islands increase, they can merge into each other and form small pits which new material is likely to settle into, to form a complete smooth film surface which results in streak features in RHEED images.

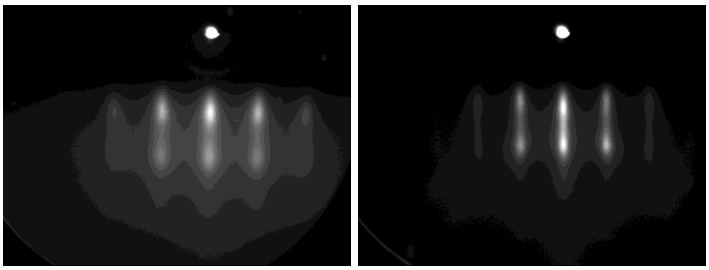

Fig 3.6: (left) RHEED image showing a combination of spots and streaks which is a result of small surface pits not yet filled in, creating a partially rough surface whereas the RHEED image (right) demonstrates clean streak features associated with epitaxial growth.

3.3 X-Ray Diffraction (XRD)

XRD is a non-destructive diffraction technique used to investigate the crystallographic composition of a thin film.

The technique utilises Bragg's law of diffraction where:

$$n\,\lambda = 2d\sin\theta$$

When an X-ray beam with a wavelength, λ passes through the surface of a crystal lattice at a certain angle, θ, diffraction is able to occur due to constructive interference when the distance, d between successive lattice spacings in the beam path differs by a complete number of wavelengths.

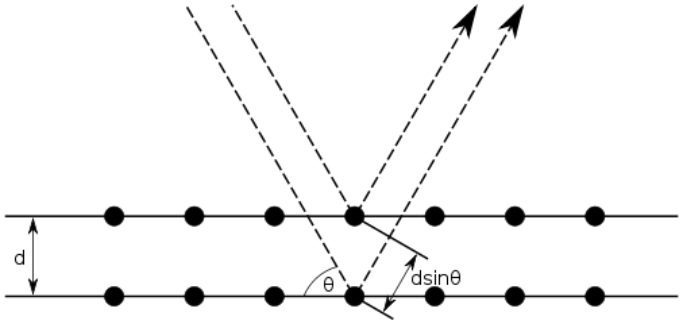

Fig 3.7: Bragg's law, showing incident radiation penetrating the crystal lattice and being diffracted by the spacing of the atoms within the lattice by $d\sin\theta$.

The diffractometer used to analyse the films in this thesis was a Bruker D8 Advance system located at Callaghan Innovation in Wellington (Fig 3.8). The operating voltage of the system was 40kV with a 35mA current, and includes a 0.23° parallel plate diffracted beam collimator and an incident beam Goebel mirror to block unwanted X-ray radiation transitions. The X-ray radiation is produced by a Cobalt Kα source with a wavelength of 1.789Å.

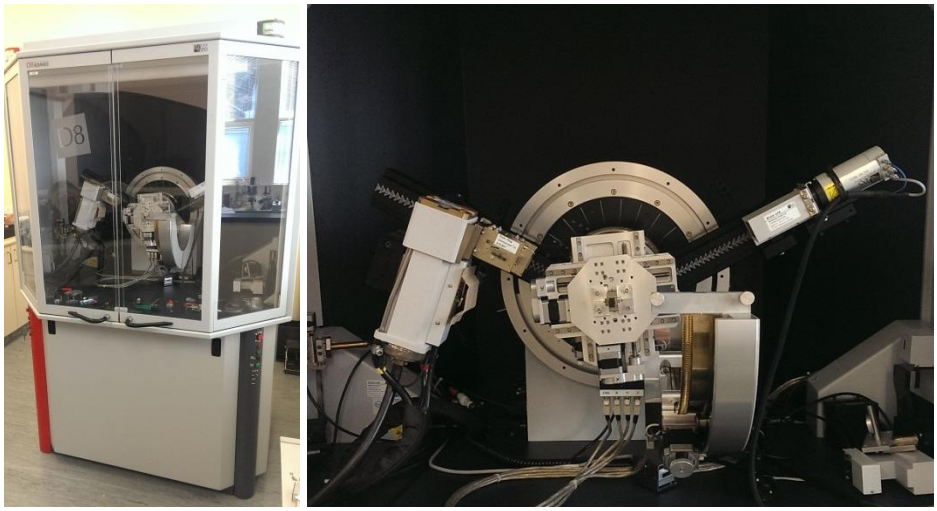

Fig: 3.8: Bruker D8 Advance system diffractometer, highlighting the rotatable axis of the X-ray source relative to the detector.

To measure the XRD for highly oriented thin films with high accuracy, a small misalignment of the sample relative to the situation of constructive interference shown in fig 3.7 must first be corrected for. To do this, the sample is fixed horizontally and the X-ray source and detector of the D8 diffractometer are controlled independently. The film height relative to the incoming beam of radiation is optimised by adjusting the stage height to a position where a horizontal incident X-ray grazes the surface of the film. Next, the intensity of a known substrate or film peak is maximised by optimising the incident and 2θ angles.

Once optimised, the incident angle of the X-ray source is swept over a range to investigate the quality of orientation for the crystallites. The peaks can be quickly identified as single crystal or polycrystalline by using the rocking curve full width half maximum (FWHM) as an indication of the level of crystal orientation in the peak. When applied to the resolved diffraction peak - the sharper the peak, the more orientated the crystal phase of the sample.

Using the parameters that result in an optimised alignment, unlocked coupled scans can then be acquired to investigate any orientated materials present in the sample and their relative intensities.

Diffracted film peaks resolved in the unlocked coupled scans were analysed using Bruker's EVA software and the chemical and crystallographic details were compared to standard values given by the International Centre for Diffraction Data database.

3.4 Scanning Electron Microscope (SEM) images

Scanning electron microscopes utilise electrons to produce highly magnified images of a film's surface. They operate by scanning a focused high energy beam of electrons along a sample surface. The electrons interact with the atoms in the sample, causing the atoms to be excited and emit secondary electrons which are detected by the system to form an image. Secondary electrons tend to be emitted near surface features such as steep slopes and edges which create a contrast that makes SEM images appear 3D. The brighter the region of the image, the more secondary electrons the detector collects.

For electrons to be absorbed and emitted, the sample must be conductive. All the thin films investigated in this thesis meet this criteria. If a sample is not conductive, the surface can be covered with a thin layer of conductive material such as gold which is known as a "capping layer".

SEM images in this thesis were captured while the sample was held under vacuum using a Raith 150 scanning electron microscope which is located in the Nanotechnology laboratory of the Electrical and Computer Engineering Department at Canterbury University. Images were typically captured up to 50 000x magnification with a resolution limit of ~50nm due to vibrations in the system.

3.5 Rutherford Backscattering Spectroscopy

Rutherford Backscattering Spectroscopy (RBS) is an analytical technique used to determine the structure and composition of materials by measuring the backscattering of a beam of high energy ions (typically protons or alpha particles) impinging on a sample [27].

The backscattered ions are collected in a detector that measures the relative energies and angle of scattering. The ions lose energy in two forms; scattering off the sample nuclei and small angle scattering with the electrons in the sample. By comparing the energy lost from small angle scattering with the density of electrons in the film it is possible to calculate the thickness of the film.

All RBS measurements of the samples were performed by Dr. Simon Granville at Callaghan Innovation in Wellington and incur an experimental ±10nm error for each stated thickness value in this thesis.

3.6 Magnetisation measurements using a Superconducting Quantum Interference Device (SQUID)

Ferromagnetism is a property dependant on both chemical composition and crystalline structure, and occurs in a material when the magnetic moments of the individual atoms interact to align in a preferential direction resulting in a net magnetic moment. The alignment of these moments can be reversed or randomised by demagnetisation, which is accomplished by either applying an opposing magnetic field or heating a sample above its Curie temperature. Above the Curie temperature thermal fluctuations have enough energy to overcome the exchange interactions that cause ferromagnetism [28].

When the magnetisation of a ferromagnetic material at a constant temperature is plotted relative to applied field strength, the plot is characterised by two dominant curves which are often symmetrical and saturate at high fields. These curves are non-linear and the

behaviour is not reversible. This lack of reversibility is defined as magnetic hysteresis (Fig 3.9).

The ferromagnetic hysteresis characteristics of a material are typically defined through a process of magnetisation and demagnetisation. This allows the identification of useful parameters relating the field strength and structure of a ferromagnetic material such as; the remnant magnetisation (M_R), the saturation magnetisation (M_s) and the coercive field (H_c). These parameters are illustrated on the magnetic hysteresis loop shown in Fig 3.9.

The M_s of the sample is defined as the magnetisation when all the magnetic dipoles in the sample align parallel to an applied magnetic field. If the applied field is removed from a saturated ferromagnetic sample of constant temperature, the magnetisation will reduce and stabilise to the M_R value. The magnitude of an opposing applied field required to reduce the magnetisation to zero is defined as H_C.

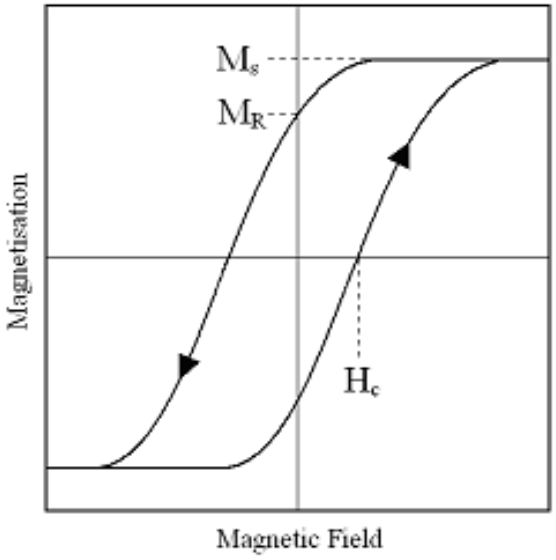

Fig 3.9: The magnetisation hysteresis of a ferromagnetic sample highlighting the saturation magnetisation (M_s), remnant magnetisation (M_R) and coercive field (H_C) [29].

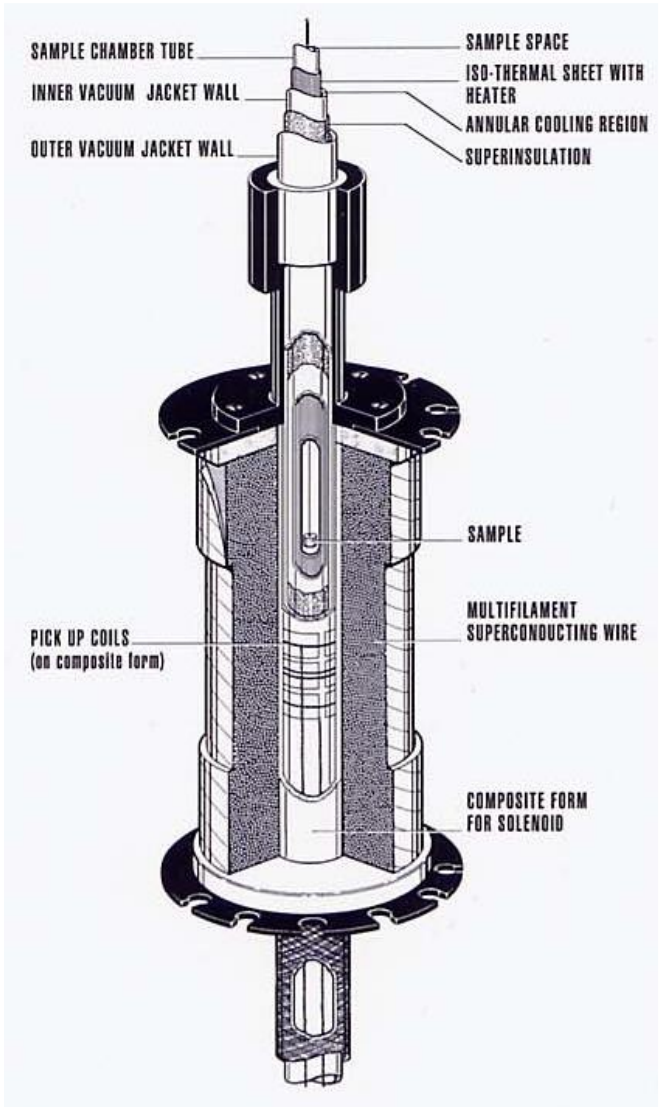

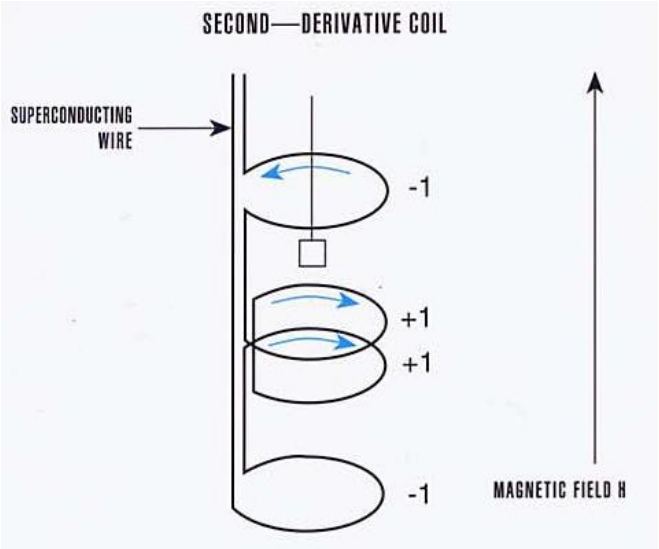

Fig 3.10: Detailed description of the sample housing and location of the second order gradiometer superconducting detection coil [28].

All the magnetic measurements of the Heusler thin films studied in this thesis were acquired using a Quantum Design Superconducting Quantum Interference Device (SQUID) magnetometer located at Callaghan Innovation in Wellington. The SQUID is the most sensitive instrument for measuring magnetic materials, with sensitivity down to 10^{-8} electromagnetic units (emu). The SQUID used in this thesis has a practical resolution of 10^{-7} emu. This device was used to characterise the magnetic properties of the Heuslers by applying up to a 70 000 Oersted field in sweeps to magnetise the sample and investigate how well the sample resists demagnetisation through parameters shown in Fig 3.9.

The SQUID does not directly detect the magnetic field from the sample, but rather acts as an extremely sensitive current to voltage converter. The sample is moved through four superconducting detection coils which are inductively coupled to the SQUID sensor in a second order gradiometer configuration to reduce the effect of noise or offsets caused by the external magnet (fig 3.10). As the sample moves through the coils, the magnetic moment of the sample induces an electric current in the detection coils through Faraday's law. Because the system is a closed loop, any change in the magnetic flux of the coils produces a proportional change in the persistent current in the detection circuit.

This change in the current in the detection coils produces a corresponding variation in the output voltage in the SQUID which is proportional to the magnetic moment in the sample.

The standard method for mounting a sample for measurement in the SQUID magnetometer is to secure the sample inside a plastic straw. Straws are used as the plastic material has only a weak diamagnetic signature, and the straws are long enough to result in a negligible change of flux as the sample is moved through the SQUID coils. An additional advantage is that straws are transparent so the initial position of the sample in the coils can be determined.

Once the sample is mounted, the straw is attached to the end of a long rod which is lowered into the detection coils which house the SQUID. A magnet surrounding the detection coils is used to apply the field.

Once the field and temperature are stabilised at chosen values, a single measurement is taken by moving the sample through the detection coils. The induced voltage across the

coils is measured at regular intervals along the scan length and the completed scans can be repeated multiple times to average the voltage signals and to increase the signal to noise ratio. The most accurate magnetic moment value is determined from the SQUID output signal by combining the systems computer fitting software with accurate location mapping of the sample. The fitting equations are based on the response expected for a magnetic dipole moving through the second order gradiometer coil configuration [28]. Temperature dependent measurements were taken by repeating this process from 400K to 2K by cooling the sample with gas from a liquid helium reservoir.

Once the magnetisation data of the films is obtained the diamagnetic contribution of the substrate was removed by linearising the saturation regions of the film to view the ferromagnetic component independently as shown in Fig: 3.11.

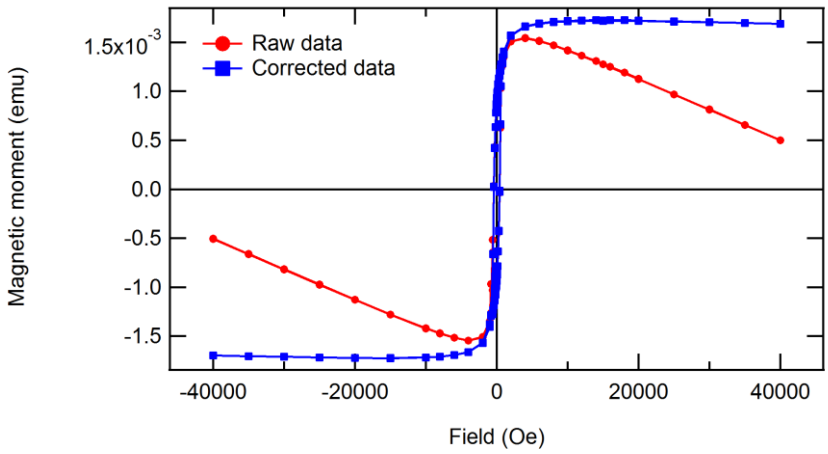

Fig 3.11: The raw data output from the SQUID for a field loop of a Co_2MnSi film grown on MgO before (blue line), and after the data is corrected with the substrate diamagnetism removed (red line).

Output values from the system are in centimetre – gram – seconds (CGS) units, and record the total magnetic moment of the sample in units of electromagnetic units (emu) and the field strength is recorded in Oersted (Oe).

The magnetic moment, m_{emu} can also be converted to SI units by dividing the emu value by the volume, V given in cm^3 and using the relationship where 1 $emu.cm^{-3}$ = 1000 $A.m^{-1}$. The sample area was measured using a microscope and the thickness was determined by using RBS measurements with an uncertainty of ±10nm.

The conversion from CGS units to SI units is as follows;

$$\text{Magnetisation: } M \text{ (A.m}^{-1}\text{)} = \frac{m_{emu} \times 10^3}{V}$$

Units of Bohr magnetons per formula units (μ_B/f.u.) are commonly referred to in the literature to describe the magnetic moment of a ferromagnetic thin film, and as such the values presented in this thesis were converted to units of (μ_B/f.u.) using the relationship:

$$\text{Magnetic moment } (\mu_B\text{/f.u.}) = \frac{\#\ \text{Bohr magnetons}}{\#\ unit\ cells} = \frac{m_{emu} \times V_{\text{unit}}}{\mu_B \times V}$$

Where V_{unit} is the volume of the unit cell of the Heusler material and the Bohr magneton is a constant where 1 μ_B = 9.274 x10^{-24} A.m^2.

Material	Unit cell volume, a^3 (cm^3)	Unit cell mass (amu)	Density (g.cm^{-3})
Co_2MnSi	4.518x10^{-23}	200.889	7.387
Co_2MnGa	4.795x10^{-23}	242.527	8.402

Table 3.1: Listed are some useful parameters used when converting CGS units to Bohr magnetons per formula unit (μ_B/f.u.).

3.7 Resistivity measurements using a Physical Property Measurement System (PPMS)

A Quantum Design Physical Property Measurement System was used to measure the temperature dependent resistivity of the Co_2MnSi samples in this thesis. The samples were prepared for the system and measured by Dr. Simon Granville and Dr. Ian Farrell.

In particular, the DC resistivity option of the PPMS was used. This option acquires precision measurements by passing a known current through the sample and measuring the voltage drop across the sample in one direction.

Resistivity measurements were obtained by measuring the resistive voltages of the sample using a four-terminal alternating current method, where two leads pass a current through

the sample, two separate leads are used to measure the potential drop across the sample, and Ohm's law is used to calculate the sample resistivity. The voltage leads draw a near zero current, virtually eliminating the effects of lead and contact resistance, so the current through the sample and the potential drop across the sample can be known to a high degree of accuracy [30].

The samples were prepared for measurement by evaporating four square silver contacts on each edge of the sample using a mask. These contacts allowed wires to be attached with a two-component Epotek Ag epoxy onto the surface of the sample which was performed under a microscope. The PPMS uses a resistivity puck to mount the samples into the system with four contacts, one positive and one negative contact for current and voltage. The sample leads were soldered on to the four gold-plated puck contact pads of the puck.

The sample wires can be soldered onto the resistivity puck using different geometries to measure the resistivity of the sample.

In this thesis two geometries were used, direct line geometry and van der Pauw geometry.

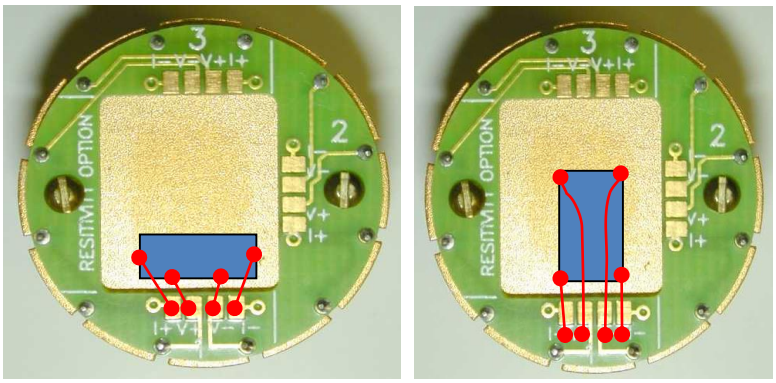

Fig 3.12: (left) Resistivity puck with a sample mounted for four wire resistance measurements using direct line geometry. (Right) Resistivity puck with samples mounted for four wire resistance measurements using van der Pauw geometry [31].

Direct line geometry is when the contacts are connected in a line along the sample surface as shown in fig 3.12. The leads for positive and negative current are mounted at the ends of the sample. The leads for positive and negative voltage are connected between the positions of the current leads.

This geometry allows resistivity in Ohm.cm to be calculated from the resistance (R) if the length (l) of the sample and the cross-sectional area (A) of the contacts are known, where:

$$\rho = \frac{R \times A}{l}$$

The van der Pauw geometry uses two resistance measurements to determine resistivity directly. It is important for the film thickness to be uniform. Using the two resistance measurements in the van der Pauw geometry, the resistivity can be calculated following the relationship: [32]

$$e^{-\pi R_{AB,CD} d/\rho} + e^{-\pi R_{BC,DA} d/\rho} = 1$$

This can be simplified and rearranged to calculate the resistivity of a sample of a known thickness, d:

$$\rho = \frac{\pi d}{2} \frac{R_A + R_B}{2} f\left(\frac{R_B}{R_A}\right)$$

For each film, we have measured R_A as a function of temperature, and R_B only at room temperature. Since the difference between R_A and R_B should be based only on the orientation and size of the contacts, these values will not change as a function of temperature. Thus, R_A and R_B will have a constant relative ratio, and R_B can be determined for any temperature from the measured R_A data. Therefore, the measurements give sufficient information to use the equation above to calculate the resistivity. The function of the ratio of the two resistances, f, is determined from the graph in fig 3.13 and ranges between 0.93 and 1 for the resistance values of Co_2MnSi.

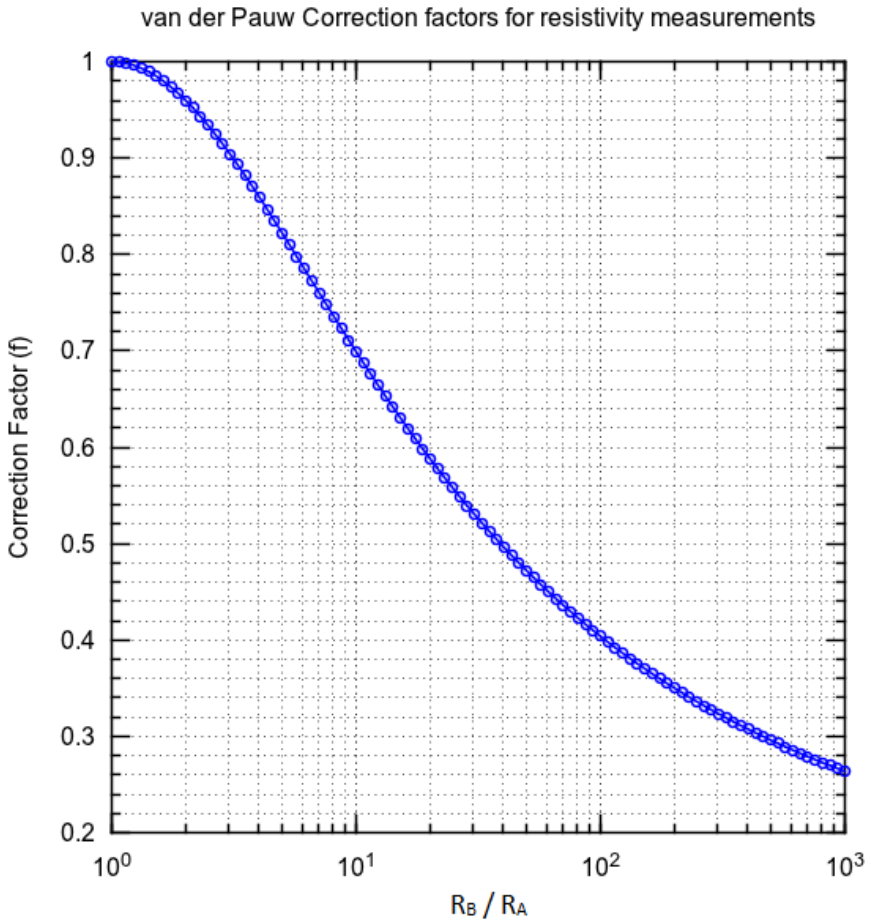

Fig 3.13: Determining the value of the van der Pauw correction factor by the magnitude of the ratio of the two resistance channels, R_A and R_B.

Chapter 4

Co_2MnSi

4.1 Growth parameters and sample list

A series of thin films of Co_2MnSi were grown using PLD. The growth quality of these films was investigated by varying three parameters: substrate choice, substrate growth temperature and laser fluence.

In total, seven films were grown on MgO substrates and six films were grown on GaAs substrates. The substrate temperature was set from 200˚C up to 700˚C during sample growth and the laser fluence ranged from ~ 2 - 7 J/cm². Average growth time was standardised at a minimum of 1 hour. This value was increased only if *in-situ* RHEED imaging suggested the deposition rate was too slow and the film would be too thin to provide an accurate analysis of the samples properties. Prior to each growth, the Co_2MnSi target was pre-ablated. The KrF laser was set at 200mJ with a pulse rate of 10Hz for 5 minutes to remove any impurities or oxidation on the target surface which could contaminate the sample during growth.

In literature, there is much debate as to which fluence produces high quality films [5][9][10][19]. In the following experiments a variety of high and low fluence values were set during growth. The value of the fluence can be very difficult to control precisely as the KrF laser used to ablate the target requires gas in order to lase. The quantity of gas in the laser depletes with every growth, as such there is an upper limit of available laser power that is restricted by how much gas is present in the laser during each use. Where possible, the laser was run on a setting which maintained a constant output energy by varying the laser voltage. When the required energy for a sample growth approached the upper limit, the laser would instead be set to a constant voltage. This leads to a slightly decreasing energy output during growth as the gas depletes but avoids the laser achieving maximum voltage, which would cause the system to cease operating mid growth. Each stated fluence value

has an associated uncertainty. These errors originate from the equipment used to measure the chamber structure and the aligned placement and transmission of the optics. This includes the laser window which was measured to lose an average transmission of 7% per hour of growth. The extent of the laser window transmission loss was not understood initially and was underestimated for the growth of PLD107_01 – PLD107_03, and PLD105_03 – PLD105_05. Due to the heavy coating depositing on the laser window, these film growths could not be assumed to be uniform.

This unintentionally resulted in laser fluence values lower than 3 J/cm², which were considered to be detrimental to the growth of half-metal thin films [19]. The laser window was removed when transmission was estimated to be below 40% and the actual transmission of the window was measured using the KrF laser and a UV detector with a power meter. The window was then repeatedly cleaned using concentrated HCl until the transmission returned to 90%. For samples which required a constant voltage to achieve the desired fluence, an additional error is included for the slight loss of energy from depleting gas over the course of the growth time.

Sample	Substrate type	Substrate temperature (˚C)	Growth time (hr)	Film thickness ±10 (nm)	Fluence (J/cm²)	Fluence uncertainty (J/cm²)
PLD105_03	MgO	200	1	41	3.28	0.23
PLD105_04	MgO	450	1	23	2.60	0.21
PLD105_05	MgO	700	1	11	2.35	0.20
PLD105_06	MgO	700	1	90	6.50	0.38
PLD105_07	MgO	700	1	66	4.57	0.28
PLD105_08	MgO	450	1	56	5.09	0.31
PLD105_09	MgO	200	2	107	6.53	0.39
PLD107_01	GaAs	200	1	62	3.51	0.24
PLD107_02	GaAs	450	1	29	2.68	0.20
PLD107_03	GaAs	700	1	26	2.65	0.21
PLD107_04	GaAs	575	1	65	4.37	0.29
PLD107_05	GaAs	575	2	153	7.06	0.41

Table 4.1: The varied growth parameters for the series of thin films Co_2MnSi samples grown using PLD.

4.2 Structural characterisation

4.2.1 RHEED images

In-situ RHEED was used to closely monitor the sample growth during the first two minutes and an image taken every ten seconds regardless of the image details.

The initial growth layers are useful for comparing how quickly the material deposited by observing how quickly the substrate reflection image changes. The spacing of the n=1 diffraction features from the images can be measured to observe the initial strain relaxation when the film was depositing directly onto the substrate relative to the film deposited on film growth layers.

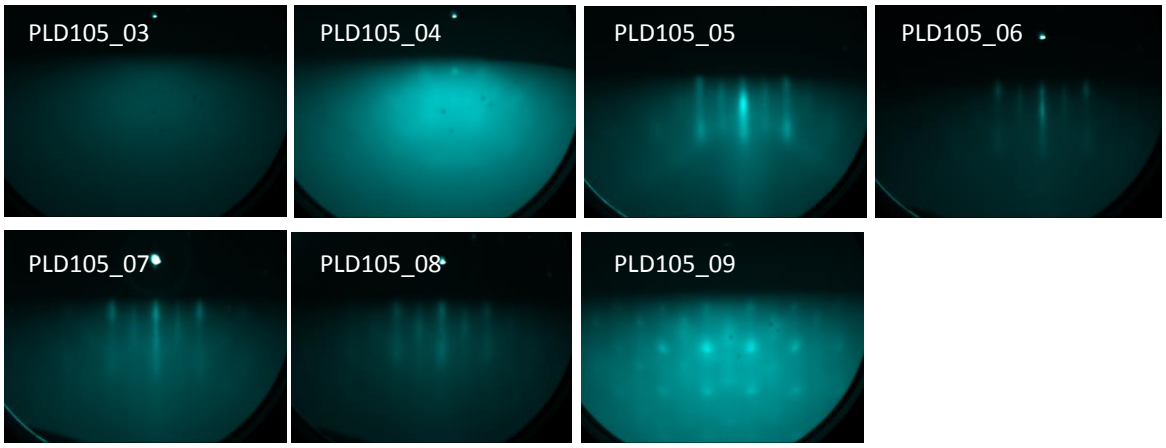

Fig 4.1: RHEED images taken at the film growth termination for the Co_2MnSi series grown on MgO.

A thin film is characterised by a blurry RHEED image due to the deposited film not being a continuous layer [3]. This feature is highlighted the RHEED image of PLD105_05 (fig 4.1), which is ~11 ± 10nm, the thinnest epitaxially grown sample in the MgO substrate series. Observing this property gives quick estimation of the PLD deposition rate during growth. Overall the other samples display sharper image details, especially the RHEED image of PLD105_06 (fig 4.1) which is ~9 times thicker than PLD105_05 and is more likely to have a regular crystal structure due to complete deposited growth layers.

The thickest samples for Co_2MnSi on MgO were prepared using high fluence and high substrate temperature. A trend developing from the growth parameters in table 4.1 suggest that high fluence values and temperatures 450°C and higher produce thin films with sharp streak features in the RHEED images. Streak patterns are a characteristic associated with epitaxial surface growth.

Low fluence and low temperature appear to be detrimental to the sample growth quality of any Co_2MnSi films grown on MgO. Image 4a of PLD105_04 was grown with low fluence at 450°C and produced RHEED images with circular details associated with a polycrystalline film surface. Image 9a of PLD105_09 was grown using the highest fluence for twice the minimum growth time and resulted in the thickest deposited film but the low substrate temperature resulted in a polycrystalline film similar to PLD105_04. Film PLD105_09 was improved by annealing the sample at 700°C for 1 hour. This was shown by the development of diffuse spots in the RHEED image. The following evidence supports the developing trend that using the combination of high fluence and high substrate growth temperature for MgO can produce RHEED images which suggest the thin films are epitaxially orientated at the surface.

A high fluence tends to produce a thicker film than a low fluence with the same deposition time. There is more target material ablated per pulse by the higher energy per unit area which contributes to more deposited material per pulse.

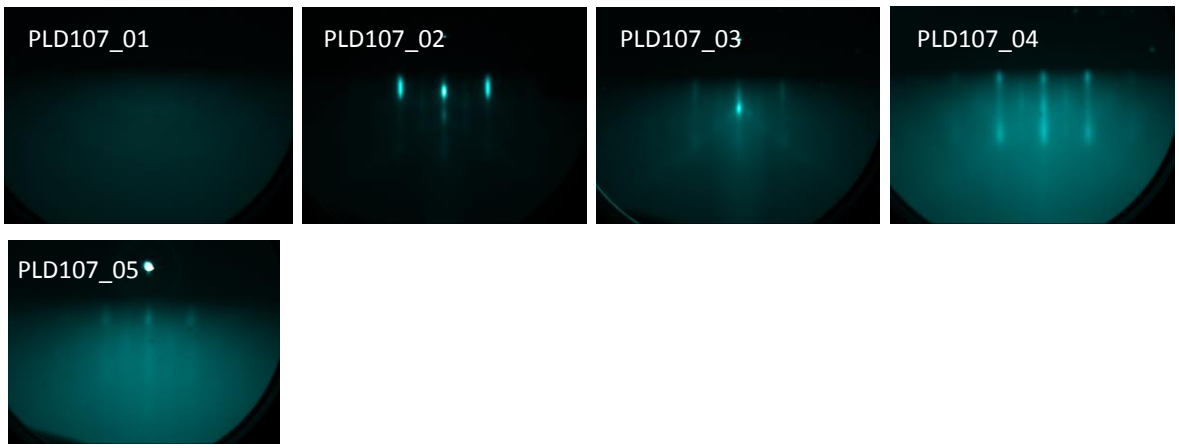

Fig 4.2: RHEED images taken at the film growth termination for the Co_2MnSi series grown on GaAs.

The RHEED images for PLD107_02 and PLD107_05 (fig 4.2) include spot features that are associated with 3D growth. The RHEED images suggest these films have rough surfaces consisting of islands of material and voids. Since these images also include streak features, the surface layer mostly likely consists of regions where there are deep rough pits randomly distributed within a relatively smooth surface layer of deposited film.

Some interesting trends arising from the growth parameters of these films from table 4.1 suggest that using a substrate growth temperature of 450°C or higher produces RHEED images with streak features. The films did not appear very sensitive to fluence changes. A range of fluence values from 2.6 to 7 J/cm² did not appear to affect the features developing in the RHEED images to the same extent as Co_2MnSi on MgO. As expected the thin films that were grown with a high fluence produced thicker films than those grown with a low fluence. This thickness trend shown in table 4.3 clearly increases with fluence for all the samples in this series.

PLD107_05 was grown using a laser fluence ~3 J/cm² higher than PLD107_04 and developed both spots and streak RHEED features (fig 4.2). In the RHEED image of PLD107_04 only streak features are present and the structure of the streak shape appears to broaden towards the bottom of the image. The RHEED images for Co_2MnSi grown on GaAs suggest these thin films did not develop uniformly smooth surface layers. The population and distribution of pits in these film surfaces could be responsible for the presence of spots and non-uniform streak RHEED features.

Kikuchi lines are present in the RHEED image of PLD107_03. These diffraction lines are attributed to long range crystalline order within a thin film [3] and are not present in other RHEED images for this growth series. GaAs (001) has a 0.02% lattice mismatch with Co_2MnSi compared to a 5% lattice mismatch and different orientation for the same film grown on MgO (101).

Thin films grown on GaAs in this series do not appear to be very sensitive to fluence, whereas thin films grown of MgO required a fluence of ~5 J/cm² or higher to develop streaks in the RHEED images. Overall the most influential parameter for producing thin films which develop epitaxial long range ordered RHEED features appears to be the 700°C substrate growth temperature for both MgO and GaAs substrates.

4.2.2 SEM images

SEM imaging of the Co_2MnSi thin films grown on MgO substrates at 50 000x magnification are displayed below:

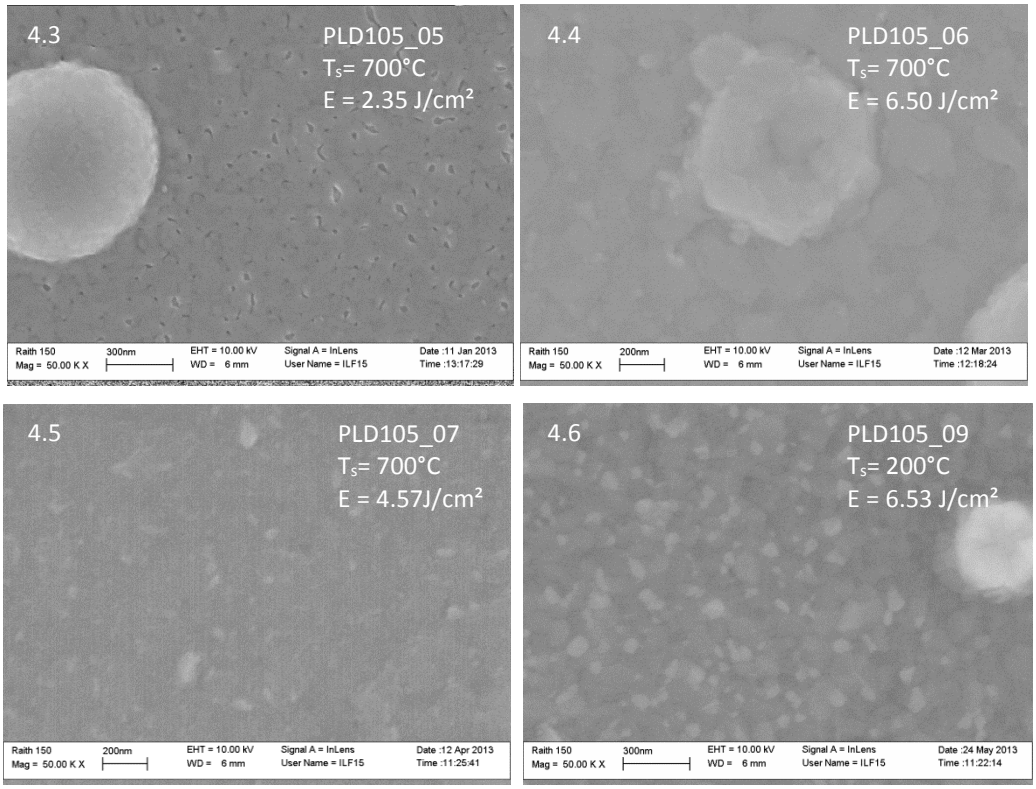

Fig 4.3 – 4.6: SEM images of PLD105 film surfaces. The sample and image details are listed in table 4.2.

In the previous section, four thin film samples of Co_2MnSi on MgO developed streak features associated with epitaxial growth in the post growth RHEED images (fig 4.1). The surfaces of PLD105_05, 06, and 07 in fig 4.3-4.5 featured above, are moderately smooth at 50 000x magnification which revealed a combination of small scale pits, raised channels and large grains. Overall the film surface layer is predominantly a complete layer. This is contrasted in fig 4.6 by PLD105_09, a polycrystalline film improved by annealing at 700°C for one hour. The surface is very rough with large ~0.5µm pits visible from 10 000x magnification.

Of these four, PLD105_07 resolved Co_2MnSi film peaks in the XRD scan presented in the following chapter. Using the FWHM and the position of this peak, the crystallite size was calculated to be 13nm which relates closely to the pits and channels which are on average ~20nm wide. Overall the surface of the films had a high density of particulates.

Sample	Fluence (J/cm^2)	T_s (°C)	Thickness ±10 (nm)	RHEED detail	Crystallite size (nm)	SEM detail
PLD105_03	3.28	200	41	Amorphous	-	Featureless surface. High density of various particulate sizes
PLD105_04	2.60	450	23	Polycrystalline	-	Rough grainy surface. High density of ~0.5µm particulates
PLD105_05	2.35	700	11	Streaks	-	Smooth surface with many ~20nm wide pits. High density of various particulate sizes
PLD105_06	6.50	700	90	Streaks	-	Smooth surface with ~100nm raised channels. High density of various particulate sizes
PLD105_07	4.57	700	66	Streaks	13	Grainy surface. moderate density of ~0.5µm particulates
PLD105_08	5.09	450	56	Streaks	-	Grainy surface. High density of ~0.5µm particulates
PLD105_09	6.53	200	107	Polycrystalline pre-anneal, with diffuse spots afterwards	-	Rough jagged surface with few ~0.5µm wide pits. High density of various particulate sizes

Table 4.2: Summary of growth parameters, RHEED details and SEM image features of Co_2MnSi grown on MgO.

SEM images of the Co_2MnSi thin films grown on GaAs substrates are shown in fig 4.7 – 4.10. The samples which developed streak features in the RHEED images revealed smooth surfaces in the SEM images. For PLD107_03, 25 000x was the highest magnification acquired. All other images are presented at 50 000x magnification.

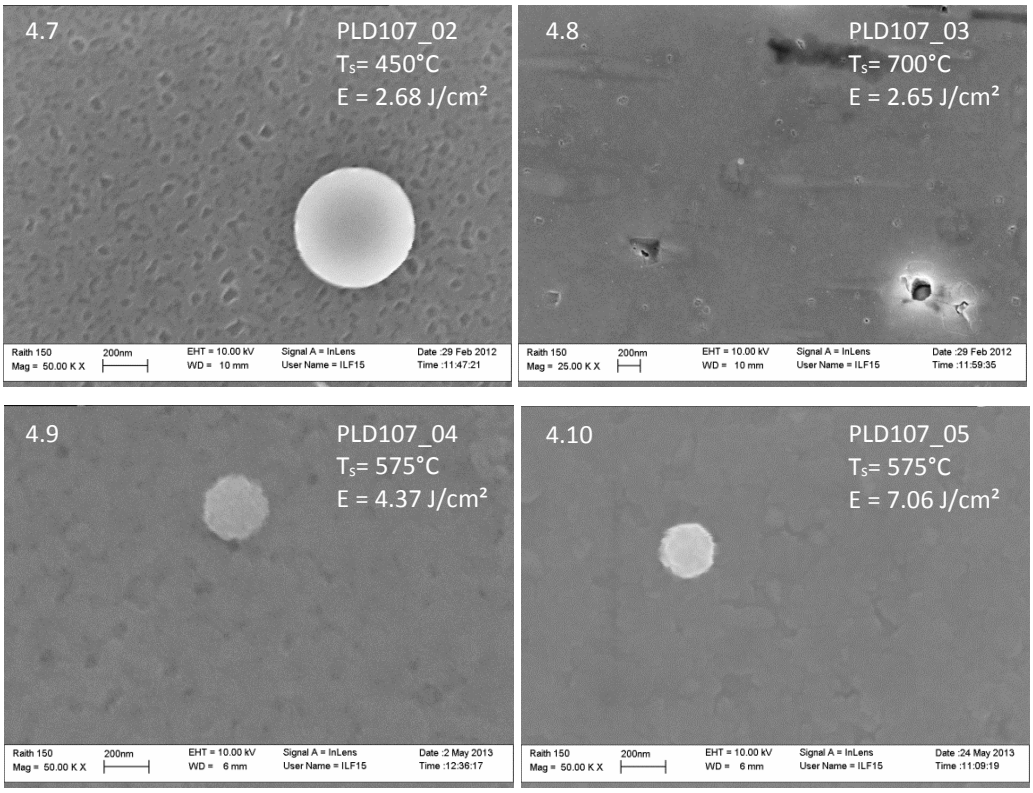

Fig 4.7 – 4.10: SEM images of PLD107 film surfaces. The image details are listed in table 4.3.

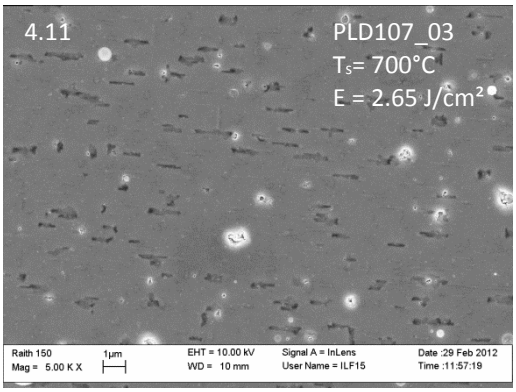

Fig 4.11: SEM image of PLD107_03 at 5 000x magnification. This film developed unusual rectangular shaped shallow surface pits which were not present on the surface of any other sample.

There is a very high population of rectangular pits on the film surface of PLD107_03 (fig 4.11). At higher magnifications, these pits appear to be filled and extremely shallow, leaving the majority of the surface area as a complete layer. Evidence of this layer is supported by the Kikuchi lines featured in the post growth RHEED image (fig 4.2 – PLD107_03) which are associated with long range crystalline order in thin films.

Sample	Fluence (J/cm²)	T_s (˚C)	Thickness ±10 (nm)	RHEED detail	Crystallite size (nm)	SEM detail
PLD107_01	3.51	200	62	Amorphous	-	Many ~125nm wide pits, low density of particulates
PLD107_02	2.68	450	29	Spots with streaks	-	Many ~50nm wide pits, high density of large 200 - 450nm particulates
PLD107_03	2.65	700	26	Faint streaks with Kikuchi lines	-	Few ~180nm rectangular shaped pits, many small ~25nm surface pits filled in or extremely shallow. High density of various particulate sizes
PLD107_04	4.37	575	-	Streaks	-	Smooth surface with raised ~100nm wide channels. Moderate density of various particulate sizes
PLD107_05	7.06	575	153	Spots with faint streaks	-	Smooth film surface. High density of large ~1μm wide particulates

Table 4.3: Summary of growth parameter, RHEED details and SEM images features of Co_2MnSi grown on GaAs. No crystallite sizes could be calculated for PLD107 series as the film peaks for Co_2MnSi could not be resolved from the GaAs substrate peaks.

Overall the SEM images of the Co_2MnSi series grown on MgO and GaAs appeared very smooth unless the films were grown using a substrate growth temperature of 200°C. Films grown using this temperature were shown to develop amorphous or polycrystalline crystal structures from *in-situ* RHEED. Surface pits were only present for PLD107_03, however these appeared shallow and are most likely a result of the film thinness due to the low laser energy of 2.65 J/cm² that was used during growth of this sample.

4.3 X-ray diffraction characterisation

X-ray diffraction Θ and 2Θ scans were performed on samples to determine the crystal orientation of the Co_2MnSi thin films.

For the PLD107 series, the film peaks were not resolvable from substrate peaks due to 0.02% lattice mismatch between Co_2MnSi and GaAs. The substrate peaks are easily characterised by their uniformly Gaussian profiles as shown in the GaAs reference scan (fig 4.12) which is the scan of a GaAs substrate annealed at 450°C for 1 hour to replicate the condition of substrates post film growth.

The peaks attributed to the GaAs substrate are (200) reflection peaks (at 36.92° and 37.00°), and the (400) reflection peaks (at 78.53° and 78.73°) from the Co $K\alpha_1$ and Co $K\alpha_2$ X-rays respectively. The small shoulder near these peaks at 36.75° and 78.12° is attributed to the GaAs reflection. All the peaks in fig 4.12 and fig 4.13 have been shifted to align with the largest GaAs substrate peak reflection caused by Co $K\alpha_1$ radiation. The intensity of each scan was normalised to the GaAs Co $K\alpha_1$ peak to better highlight the developing shoulder in the located in the region of the bulk Co_2MnSi (200) peak and (400) peak respectively.

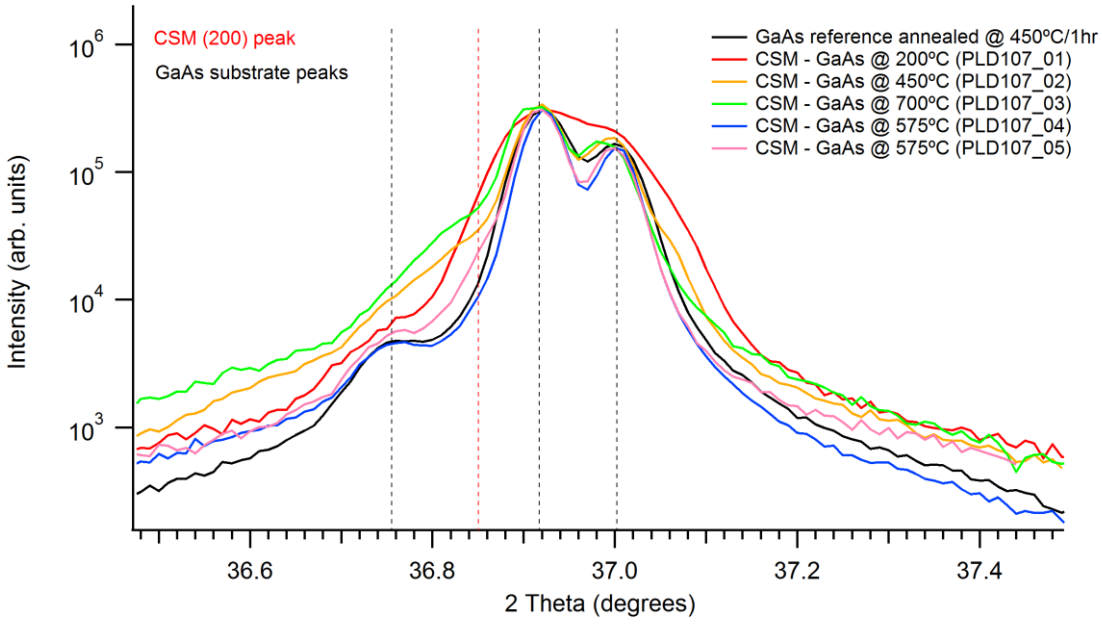

Fig 4.12: XRD of the (200) peak region for Co_2MnSi grown on GaAs substrates.

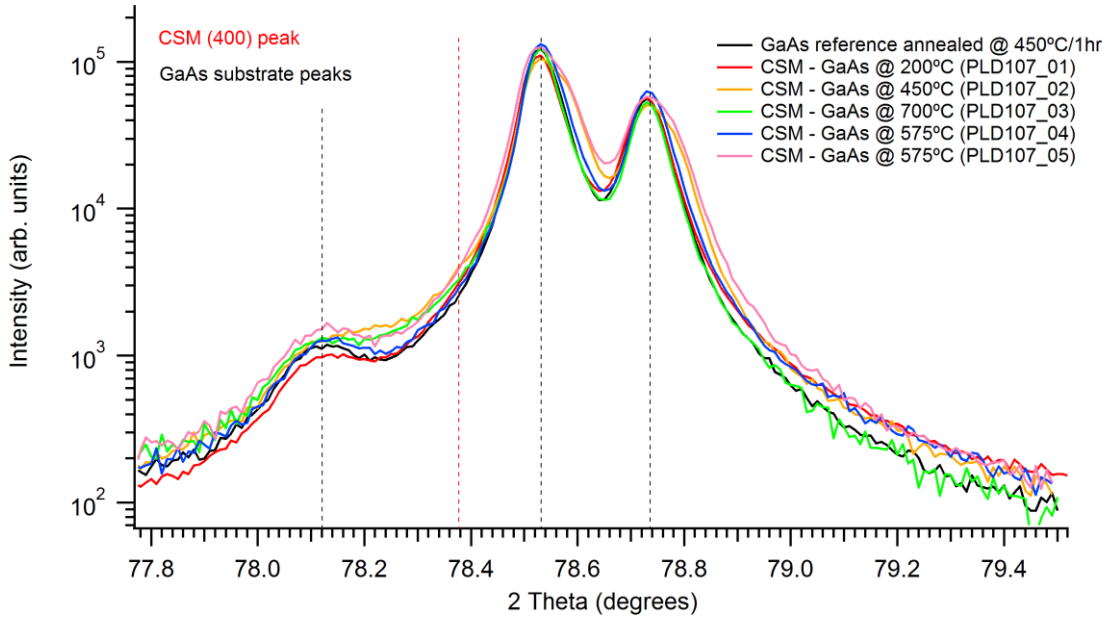

Fig 4.13: XRD of the (400) peak region for Co_2MnSi grown on GaAs substrates.

When looking at the (200) and (400) reflection peaks of GaAs in fig 4.12-4.13, there is a visible shoulder detail developing on the left hand side where the bulk Co_2MnSi superlattice (200) and fundamental (400) peaks [33] should be located (precisely at 36.89° for (200) and 78.51° for (400)). The effect is strongest the region where the (200) bulk Co_2MnSi is located in fig 4.12, however the (400) bulk Co_2MnSi region has a much higher background due to the (400) bulk GaAs peak which could be contributing to the relative weak appearance of this region.

As the Co_2MnSi peaks cannot be separated from the GaAs substrate diffraction peaks, no thorough analysis can be attempted. However it is interesting to note that PLD107_02 and PLD107_03 are the thinnest samples in the Co_2MnSi series on MgO, and are on the order of 20 ±10 nm. This low thickness could be responsible for a high strain between the film and the substrate which allows these peaks to appear more resolved than the thicker films on the order of 60 – 150 ±10 nm. These thicker films would have relaxed to values closer to the atomic spacing of bulk Co_2MnSi.

Given the small 0.05% margin of strain between the Co_2MnSi film peaks and the atomic spacing of the bulk Co_2MnSi (table 4.7), the film peaks could easily be overshadowed or incorporated into the substrate Co $K\alpha_1$ X-ray peaks as suggested by the distortion and

broadened Gaussian profile for the (400) GaAs peak shown by PLD107_01 and PLD107_05 in particular.

For the GaAs (200) reflection peak in fig 4.12, a merging of the Co $K\alpha_1$ and Co $K\alpha_2$ X-ray peaks occurs in PLD107_01. This 200°C temperature growth was shown to produce a polycrystalline film from the post growth RHEED image (fig 4.2 – PLD107_01). The film deformation caused by the non-uniform strain in the polycrystalline growth structure of this sample supports an irregular broadening of these features.

The XRD peaks in fig 4.12 - 4.13 have been shifted independently of each other to align with the strongest GaAs reference substrate peak for (200) and (400). The applied shifts are as follows:

Sample	(200) 2Θ peak location (°)	Required (200) 2Θ peak shift (°)	(400) 2Θ peak location (°)	Required (400) 2Θ peak shift (°)
PLD107_00 (reference)	36.92	-	78.53	-
PLD107_01	36.89	+0.03	78.50	+0.03
PLD107_02	36.93	-0.01	78.54	-0.01
PLD107_03	36.90	+0.02	78.53	+0.00
PLD107_04	36.92	+0.00	78.54	-0.01
PLD107_05	36.98	-0.06	78.54	-0.01

Table 4.4: Peak shifts applied to the XRD scans of Co_2MnSi on GaAs.

There was an absence of film peaks in all the Co_2MnSi samples grown on MgO except for PLD105_07 shown in fig 4.14. The absence of film peaks was not a result of thickness, as samples thicker than PLD105_07 were produced. Despite other samples in the series also suggesting epitaxial growth from *in-situ* RHEED, an influential parameter could be high growth temperature of 700°C which was a parameter unique to PLD105_07 in this series.

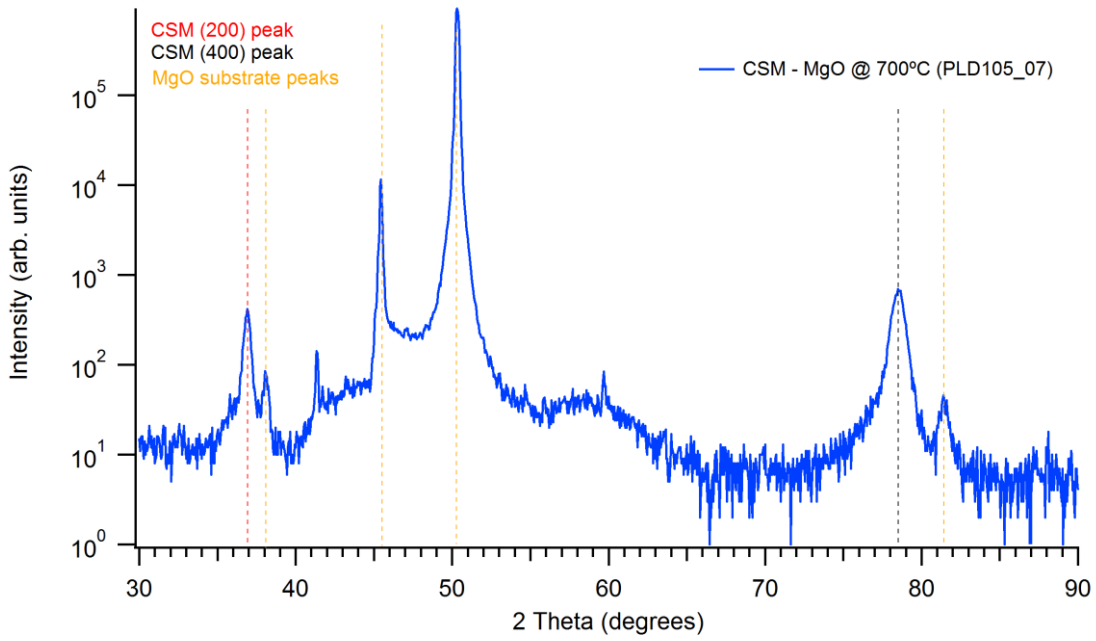

Fig 4.14: Full 2Θ XRD scan of PLD105_07, a Co_2MnSi thin film grown on a GaAs substrate.

The peaks of PLD105_07 correspond to the bulk Co_2MnSi peaks for the superlattice (200) and fundamental (400) reflections [33]. The minor peaks beside the film peaks are mostly likely due to shifted MgO substrate peaks as two strong peaks located at 43.16° and 89.54° were not present in the scan.

The sharp gaussian peaks in fig 4.14 of PLD105_07 are a characteristic associated with epitaxial growth, and the presence of a (111) peak or a (200) peak is attributed with highly aligned single crystals [33]. An $L2_1$ structure is characterised by strong (111), (220), (311) or (331) peaks [21][33][34]. The only film peaks resolvable in this sample are the fundamental (400) peak and the superlattice (200) peak which indicates the film is orientated as a B2 crystal [33]. This is confirmed by comparing the relative peak intensities of the (200) and (400) reflections, as the (400) peak dominates. This usually occurs in Heusler films orientated in a B2 crystal structure, as the intensity of the peaks is determined by disorder of the Mn and Si atoms in the diffracting plane [15].

Bulk Co_2MnSi crystal has a lattice constant of 5.654Å [10]. A film lattice constant can be calculated from the position of the (200) and (400) XRD film peaks and thus the strain can be calculated. Table 4.5 displays the XRD results for the Co_2MnGa films grown on MgO

substrates, there are no results for films grown on GaAs substrates as no film peaks were resolved.

Sample	Substrate	Growth temp (°C)	Dominant peak orientation	200 peak (°)	200 strain (%)	400 peak (°)	400 strain (%)	Dominant peak FWHM (rad)	Crystallite size (nm)	Peak area
PLD105_07	MgO	700	400	36.9	0.05	78.506	0.09	0.0162	13	632.47
PLD107_xx	GaAs	-	200	-	-	-	-	-	-	

Table 4.5: Summary of the (200) and (400) film peak locations, the strain of these peaks was calculated relative to the expected film peaks of Co_2MnSi.

The dominant FWHM in table 4.5 refers to the most intense Co_2MnSi film peak reflection in a sample scan and was used to calculate the crystallite sizes quoted in chapter 4.2.2 for the SEM images of the samples.

Calculating this value gives useful indication of the crystallite size of films which could not be resolved in SEM at higher magnifications.

Crystallite size is determined using Scherrer's formula [29]:

$$D = \frac{0.94\lambda}{\beta cos\theta}$$

Where D is the average dimension of the grains, λ is the wavelength of the radiation, β is the FWHM of the film peak in radians and Θ is the angle at which the peak is located.

4.4 Magnetic measurements

The magnetic moments of the Co_2MnSi samples were investigated at 10K and 300K in magnetic fields up to 60KOe using the SQUID magnetometer at Callaghan Innovation.

Field loops were performed on PLD107_01 and PLD107_03 of the PLD107 sample series and all the PLD105 sample series except for PLD105_06 and PLD105_09.

Fig 4.15 – 4.18 show the field loop data for seven samples of the Co_2MnSi series grown on MgO substrates. Following in fig 4.19 – 4.22 are the field loops for two samples of the Co_2MnSi series grown on GaAs substrates.

The choice of substrate affected the value of the saturation magnetisation (M_S) measured for the films. In general, M_S was the largest for Co_2MnSi thin films grown on MgO substrates and lowest for thin films grown on GaAs substrates. The maximum M_S found at 10K for each substrate was 4.65±0.83 μ_B/f.u. and 3.54±1.36 μ_B/f.u. for MgO and GaAs respectively.

The MgO value agrees within uncertainty with the theoretically predicted Co_2MnSi magnetic moment of 5.07 μ_B/f.u.[6], whereas Co_2MnSi on GaAs is 30% lower than this value. Both results agree with other M_S values published in literature which range from 4.95 – 5.10 μ_B/f.u [9][10].

There are three magnetic hysteresis loop shape profiles shown by the Heusler alloys investigated in this thesis. The loops which are non-uniform and particularly distorted at $\pm H_C$ are observed from samples that have a high population of disordered growth orientations in the film structure such as for amorphous and polycrystalline films (fig 4.16, PLD105_03). The next profile is defined by the curved edges of the hysteresis loop before the saturation of the magnetic moments in the sample (fig 4.16, PLD105_07). This shape is a result of the broadening loop due to the large $\pm H_C$ values. Lastly, the square hysteresis shape (fig 4.16, PLD105_08) is most desirable for device applications due to the well-defined and sharp change in the magnetisation near H_C. The hysteresis loop shape appears very angular due to the steep increase and decrease rate of the magnet moments which causes the small $\pm H_C$ value.

The magnitude of H_C decreases from 10K to room temperature for all of the films (fig 4.15 – 4.22). This result is due to the properties of ferromagnetism as magnetic moments can be demagnetised by applied temperature as well as applied field strength. The moments in the film at 300K have more thermal energy than the moments at 10K and less overall applied field strength is required to demagnetise the film.

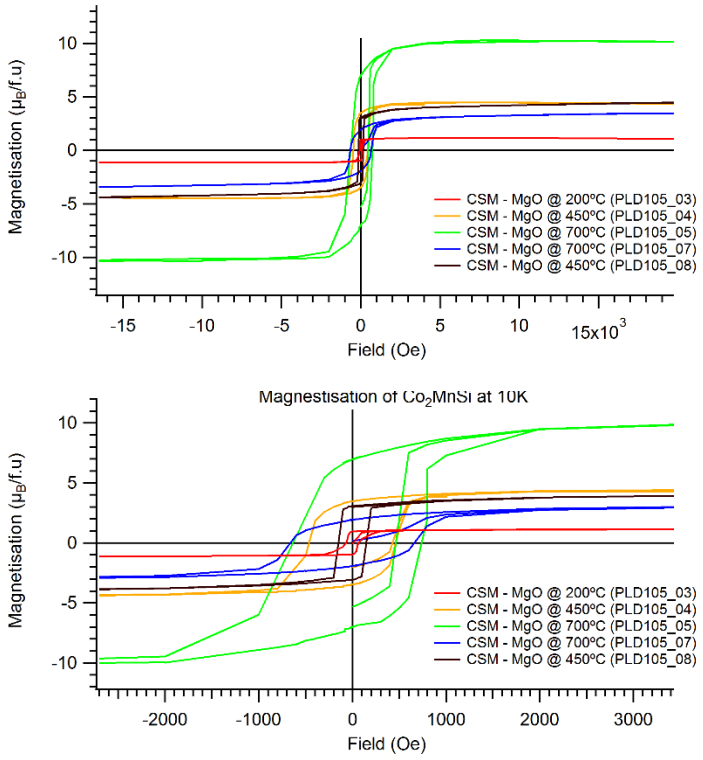

Fig 4.15 – 4.16: Hysteresis loops of Co_2MnSi on MgO measured at 10K (above) with a close-up view of the hysteresis loop shape and values of H_C (below). The magnetisation of PLD105_05 is overestimated due to the 11±10nm thickness of the sample.

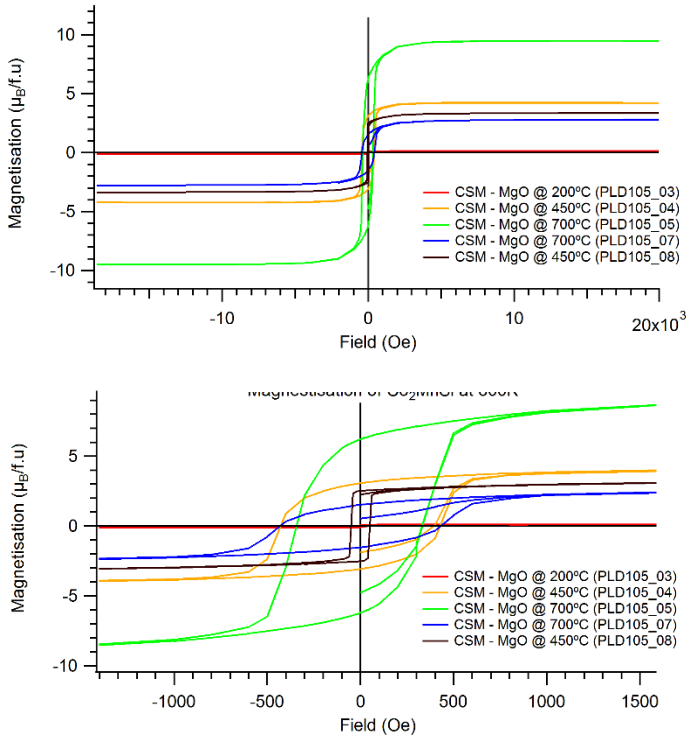

Fig 4.17 – 4.18: Hysteresis loops of Co_2MnSi on MgO measured at 300K (above) with a close-up view of the hysteresis loop shape and values of H_C (below).

The majority of the magnetic hysteresis loops for Co_2MnSi on MgO at 300K are curved in shape (fig 4.17 and 4.18), these loops have high M_S values and the largest H_C values for this series. The highest M_S values were produced by the samples grown at 450°C, in particular PLD105_08 has a very square loop profile and was grown using a combination of a 450°C substrate temperature with a high fluence of 5.09 J/cm².

PLD105_05 was the only sample to result in an M_S higher than the stated theoretical value with an M_S of 10.20 μ_B/f.u. recorded at 10K. This discrepancy shows the importance of film thickness when calculating the magnetisation in units of μ_B/f.u. This film thickness was estimated using RBS to be 11± 10nm and as such the film is too thin to calculate an accurate M_S or M_R value for the magnetic properties.

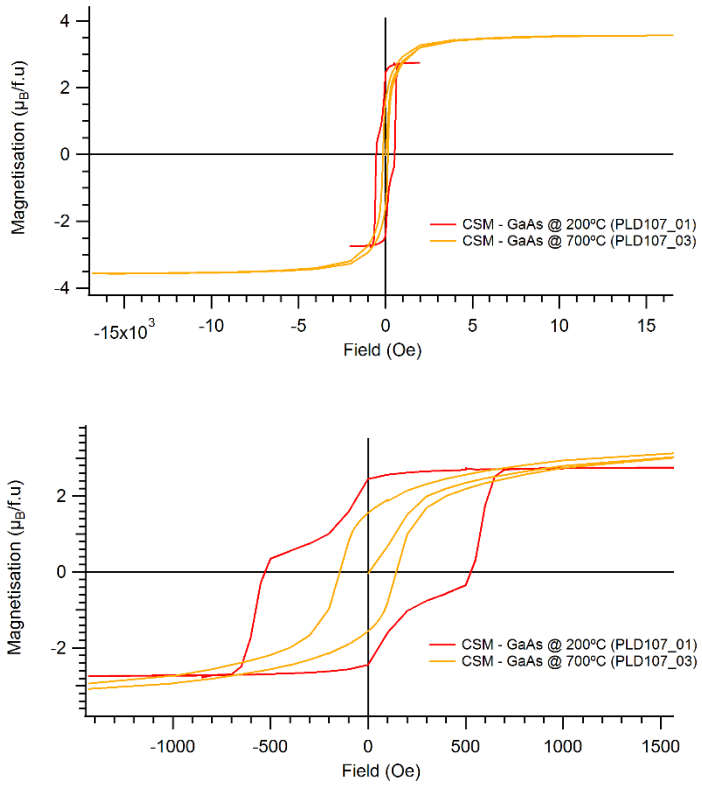

Fig 4.19 – 4.20: Hysteresis loops of Co_2MnSi on GaAs measured at 10K (above) with a close-up view of the hysteresis loop shape and values of H_C (below).

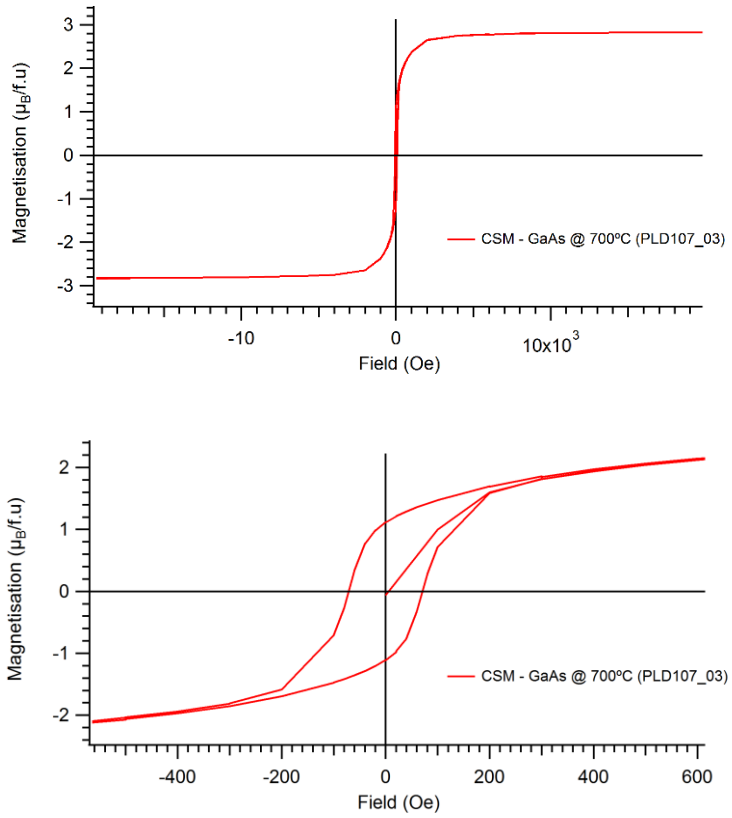

Fig 4.21 – 4.22: The hysteresis loop measured at 300K of PLD107_03 (above) with a close-up view of the hysteresis loop shape and values of H_C (below).

The magnetic moments of PLD107_01 and PLD107_03 were examined at 10K (fig 4.19 – 4.20). The loop shape of PLD107_03 has curved features which are consistent with the previous Co_2MnSi 700°C films grown on MgO (fig 4.15 – 4.16). The distorted loop shape of PLD107_01 is expected for a polycrystalline film. The values of H_C are similar to PLD105_04 (fig 4.16) and the M_S value is 38% smaller. Only one magnetic hysteresis loop of Co_2MnSi grown on GaAs was examined at 300K (fig 4.22). The loop shape has curved features which are consistent with the previous Co_2MnSi 700°C films grown on MgO with little change other than the expected reduction in M_S and H_C

Each sample of Co_2MnSi grown on MgO and GaAs resulted in a magnetic hysteresis loop at 10K which is a feature unique to material with ferromagnetic behaviour [28]. Due to the high Curie temperature of Co_2MnSi this behaviour was expected regardless of the quality of the film crystal structure [10][28]. For films such as PLD105_03 and PLD105_04 (fig 4.15 – 4.16) which were determined to be amorphous and polycrystalline respectively from post growth RHEED images (fig 4.2), the magnetic hysteresis loops are very weak and distorted

in shape near ±H_C. Overall, all the Co_2MnSi samples examined show ferromagnetic behaviour at 300K, with a decrease in M_S compared to the 10K magnetic hysteresis loops of approximately 23% on average, with 85% being the largest decrease for amorphous PLD105_03 and 5% being the lowest decrease for polycrystalline PLD105_04.

Sample	T_S (°)	10K					300K				
		M_S (μ_B/f.u.)	M_R (μ_B/f.u.)	H_C (KOe)		M_R/M_S	M_S (μ_B/f.u.)	M_R (μ_B/f.u.)	H_C (KOe)		M_R/M_S
PLD105_03	200	1.15	0.95	-66.9	67.6	0.83	0.14	0.10	-11.4	39.9	0.70
PLD105_04	450	4.47	3.45	-500.1	500.8	0.77	4.24	3.07	-426.5	426.3	0.72
PLD105_05	700	10.20	6.94	-501.8	597.1	0.68	9.49	6.22	-342.3	329.6	0.65
PLD105_07	700	3.56	1.93	-659.9	663.5	0.54	2.80	1.52	-430.9	428.5	0.54
PLD105_08	450	4.65	3.07	-149.6	147.8	0.66	3.36	2.51	-50.1	50.2	0.75
PLD107_01	200	2.75	2.44	-528.4	524.5	0.89	-	-	-	-	-
PLD107_03	700	3.54	1.56	-145.6	144.9	0.44	2.82	1.12	-71.2	71.1	0.39

Table 4.6: Summary of the substrate growth temperature and magnetic property values of the Co_2MnSi series. The sample name PLD105 and PLD107 relates to thin films grown on MgO and GaAs respectively.

4.5 Resistivity measurements

The resistivity of Co_2MnSi on MgO and GaAs was investigated to observe how strongly the material opposes the flow of electric current with temperature. A low resistivity indicates a material that readily allows the movement of electric charge which is crucial for making devices [36]. In practice, pure bulk crystals of metals have lower resistivities than thin films due to the higher quality of the crystal structure and fewer defects in the material [36].

The resistances of seven samples were found by PPMS measurements and converted to resistivities. PLD105_06 was mounted on the resistivity puck using straight line geometry whereas the remaining six samples were mounted using the van der Pauw geometry, as the geometry of these samples was unfavourable for straight line contacts.

Sample	R_1 (from R_{AB}) (Ω)	R_2 (from R_{BC}) (Ω)	RBS Thickness (nm)
PLD105_06	Measured in straight line geometry using sample area = 2.9mm²		90
PLD105_07	26.28	22.82	66
PLD105_08	11.62	6.540	56
PLD105_09	1.180	0.486	107
PLD107_01	43.94	37.45	62
PLD107_02	72.00	65.00	29
PLD107_03	87.04	80.65	26
PLD107_04	30.35	26.45	65

Table 4.7: Measured van der Pauw geometry resistances at room temperature that are used to convert the resistivity values to converting to resistivity of the Co_2MnSi series.

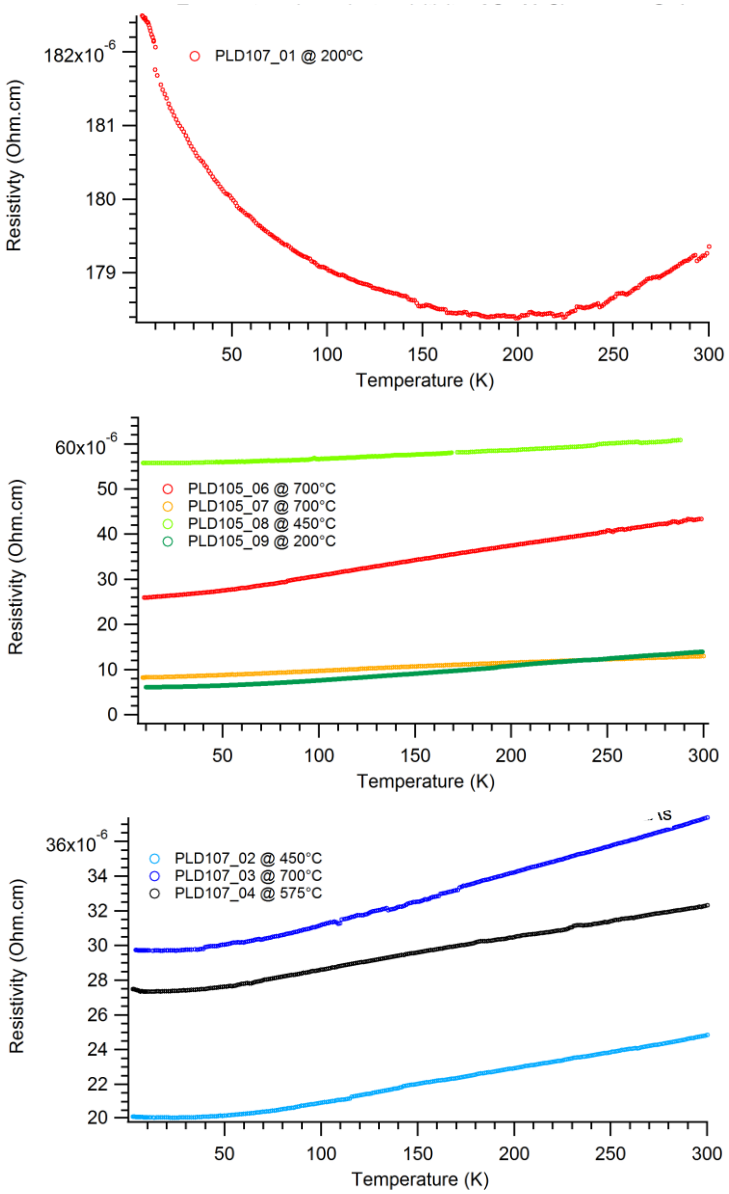

Fig 4.23 – 4.25: The temperature dependence resistivity of seven Co_2MnSi films. The general trend of a monotonically increasing resistance is observed for six of the seven films which is the expected dependence for a ferromagnetic metal [36][37][38].

The highest resistivity of the series was measured for PLD107_01 grown at 200°C (fig 4.23). The crystal structure of this material was shown to be amorphous from *in-situ* RHEED imaging (fig 4.3, PLD107_01) which implies the sample's crystal structure is the most defected in this series. The extremely non-linear curve (fig 4.23) is further evidence of the amorphous crystal structure [39]. The lowest resistivities are given by PLD105_09 and PLD107_02 for MgO and GaAs respectively (fig 4.24-2.5). Although the growth conditions of these two samples were completely different, both showed spot features in the *in-situ* RHEED imaging (fig 4.2, PLD105_09, fig 4.3, PLD107_02).

The basic relationship to describe the resistivity of a magnetic metal consists of three components; a residual resistivity $\rho_R(T)$, a quadratic term $\rho_m(T)$ due to electron-magnon scattering, and a term $\rho_P(T)$ due to electron-phonon scattering [36]:

$$\rho(T) = \rho_R(T) + \rho_m(T) + \rho_P(T)$$

The residual resistivity, ρ_0, is a constant which is temperature independent and caused by defects in the crystal lattice for the particular material.

The phonon term is present in all metals, and is given by the Bloch-Grüneisen formula [36]:

$$\rho_P(T) = A(\frac{T}{\theta_D})^5 \int_0^{\theta_D/T} \frac{x^5}{(e^x - 1)(1 - e^{-x})} dx$$

The constant A is a parameter which depends on the velocity of electrons at the Fermi surface and the Debye temperature, Θ_D was initially defined as 456K which was calculated in literature for Co_2MnSi [40].

In metal ferromagnets, a quadratic term exists due to electron-magnon scattering or "spin flips". In half-metals, which have a predicted 100% spin polarisation at the Fermi level, an energy gap exists for one spin direction [4]. This gap exponentially suppresses the electron-magnon scattering of the conduction electrons at low temperatures, and this effect is represented empirically in the magnon-scattering term by multiplying this term by a Boltzmann factor [36]:

$$\rho_M(T) = CT^2 e^{-\Delta/T}$$

where the parameter C is a measure of the strength of the scattering process and Δ is the energy gap in the density of states of the unoccupied minority spins.

The following equations for the temperature-dependent resistivity were investigated by choosing a constant set of parameters and observing how these equations modelled the data.

Equation A:

$$\rho(T) = \rho_0 + A(\frac{T}{\theta_D})^5 \int_0^{\theta_D/T} \frac{x^5}{(e^x-1)(1-e^{-x})} dx$$

(Residual resistivity with the phonon term)

Equation B:

$$\rho(T) = \rho_0 + CT^2$$

(Residual resistivity with the magnon term and no energy gap)

Equation C:

$$\rho(T) = \rho_0 + CT^2 e^{-\Delta/T}$$

(Residual resistivity with the magnon term including the energy gap)

Equation D:

$$\rho(T) = \rho_0 + CT^2 + A(\frac{T}{\theta_D})^5 \int_0^{\theta_D/T} \frac{x^5}{(e^x-1)(1-e^{-x})} dx$$

(All the terms with no energy gap)

Equation E:

$$\rho(T) = \rho_0 + CT^2 e^{-\Delta/T} + A(\frac{T}{\theta_D})^5 \int_0^{\theta_D/T} \frac{x^5}{(e^x-1)(1-e^{-x})} dx$$

(All the terms including the energy gap)

As the resistivity of metals is dominated by electron-phonon scattering, equation E typically leads to linear temperature dependence at temperatures higher than the energy gap [36][37][38]. If the thin film samples of Co_2MnSi do have 100% spin polarisation at the Fermi level, then the addition of an energy gap to the electron-magnon scattering term is needed to obtain a good fit to the measured resistivity data at low temperature to exponentially suppress the characteristic ~T^2 dependence present in ordinary metallic ferromagnets [36].

Fitting the conventional pure electron-magnon and electron-phonon terms without the energy gap should fail to produce an adequate fit for a half-metallic ferromagnet.

In order to determine which equation best models the temperature-dependent resistivity of the thin films, the resistivity data for PLD107_02 was compared with equations A-E in fig 4.26. Following the assumption that Co_2MnSi is a half-metallic ferromagnetic alloy, the parameters were chosen such at equation E was well matched to the data. By keeping these parameters constant the variance between the different equation models are clearly shown in fig 4.26. The thin film PLD107_02 was selected as this sample resulted in the lowest measured resistivity values of the series, indicating this sample has the least defected crystal structure and should provide a more accurate comparison to bulk Co_2MnSi parameter values in the literature [36].

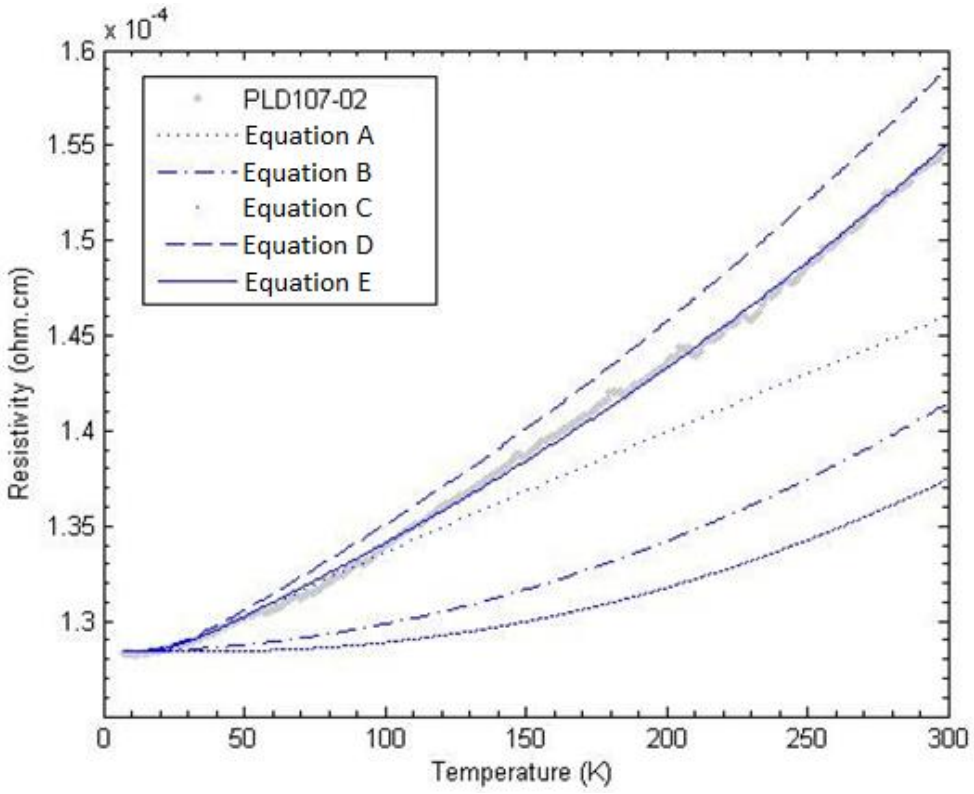

Fig 4.26: Comparing the difference between the five equation combinations using constant parameters which allowed equation E to best fit the data. The purpose of this graph is to observe the effects of the terms in equations A-E, as such no parameter values are stated.

Equation A represents the electron-phonon dominated resistivity relationship for non-magnetic metals, which is characterised by linear temperature dependence at

temperatures higher than 50K and saturation towards residual resistivity at lower temperatures. This equation shows that the Debye temperature is crucial for accurate low resistivity fitting.

Equation B relates to the $\sim T^2$ electron-magnon dominated resistivity of a ferromagnetic metal without an energy gap at E_F. The steeply curving quadratic nature of the equation does not correlate well to the data of PLD107_02.

The addition of an energy gap to exponentially suppress the quadratic term at low temperatures improves the shape of equation C relative to the data. Including the energy gap without the phonon term that is present in all metals highlights that equation C becomes more linear at high temperatures.

The electron-magnon and electron-phonon terms in equation D are not sufficient to model the curve of the resistivity. Without the quadratic electron-magnon $\sim T^2$ relationship, Equation D fails to relate to the data at both low and high temperature resistivity.

Including an energy gap within the electron-magnon term shown in Equation E is necessary to accurately model a ferromagnetic half-metal compared to a ferromagnetic metal. At low temperatures the complete absence of minority "spin-flips" suppresses the quadratic term. Above the energy gap, the quadratic $\sim T^2$ term is no longer exponentially suppressed and the equation models a shallow curve which correlates well with the data.

By observing the nature of the different equations, it is clear that equations D and E are the most accurate models for the temperature-dependent resistivity of PLD107_02. This is expected given that the phonon term is present in all metals. The addition of an energy gap in the electron-magnon term in Equation E produces the best model of the resistivity data. This confirms that the resistivity data of Co_2MnSi behaves like a half-metallic ferromagnet material. It is interesting to note that having an energy gap implies that perfect spin polarisation of electrons at the Fermi level is only present for temperatures below this gap. In order to extract a value for the energy gap by modelling equation E, the Debye temperature of the thin film must be known to a high degree of accuracy.

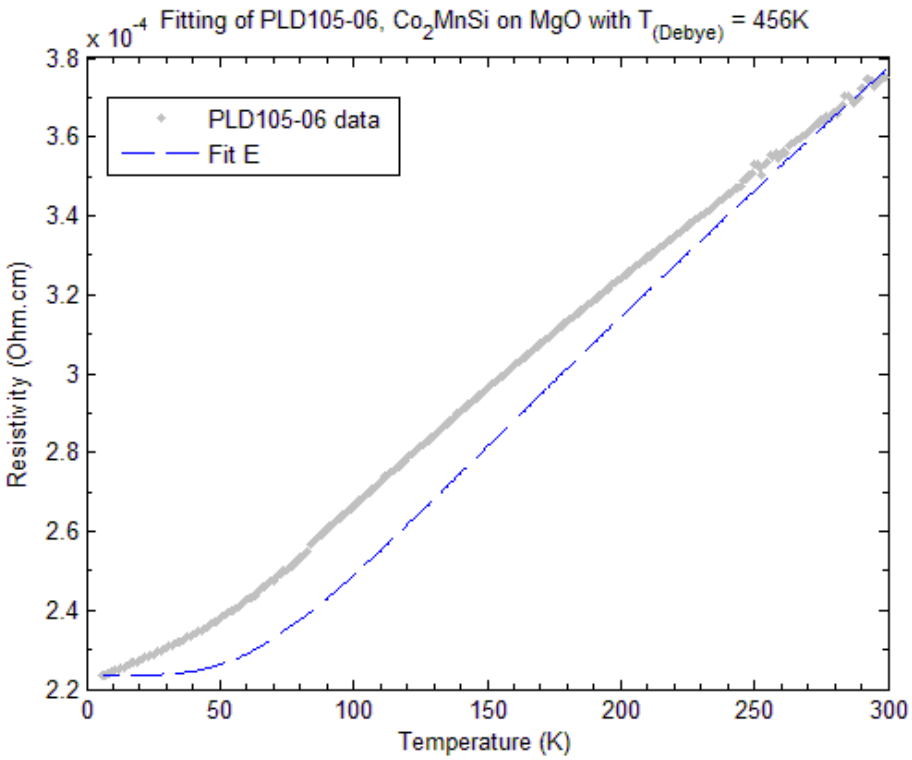

Fig 4.27: Comparison of PLD107_02 and equation E when using the bulk Debye temperature of Co_2MnSi $\Theta_D = 456K$.

The bulk Debye temperature of Co_2MnSi is stated as 456K in literature [40]. The fitting parameters for equation E were determined by eye in fig 4.27 while the Debye temperature of Co_2MnSi was set at 456K. Using this constant value for the Debye temperature resulted in poor correlation between equation E and the resistivity data at low temperature. In this situation, use of the bulk Co_2MnSi Debye temperature is not appropriate as thin films tend to be more defected than bulk crystals.

For thin films, the Debye temperature is expected to be ~ 50% to 70% less than the bulk value at the surface [40]. Considering the majority of the Co_2MnSi thin films grown on MgO in this thesis are only 11-107nm thick, the Debye temperature of these films will be affected by this condition.

The Debye temperature relative to bulk Co_2MnSi may vary anywhere within a 20% range. This variance will contribute a large margin of error to any parameter values (table 4.8) found using this method of analysis.

The bulk Debye value of 456K is calculated using the bulk modulus of Co_2MnSi, but not the shear modulus. Inclusion of this factor increased the bulk value of Co_2MnSi to 718K [39]. Assuming the surface Debye value is 50% of the bulk Co_2MnSi value at the most, and at the least 30% of this value, four possible Debye temperatures were chosen:

$\Theta_{D(bulk\ Co_2MnSi)}$ = 456K [40]: $\Theta_{D(50\%)}$ = 228K and $\Theta_{D(30\%)}$ = 136.8K

Θ_D = 718K [39]: $\Theta_{D(50\%)}$ = 359K and $\Theta_{D(30\%)}$ = 215.4K

The following temperature dependent resistivity graphs (fig 4.28 - 4.34) each of the four Debye temperatures to show how the variation of this parameter affects the modelling of equation E:

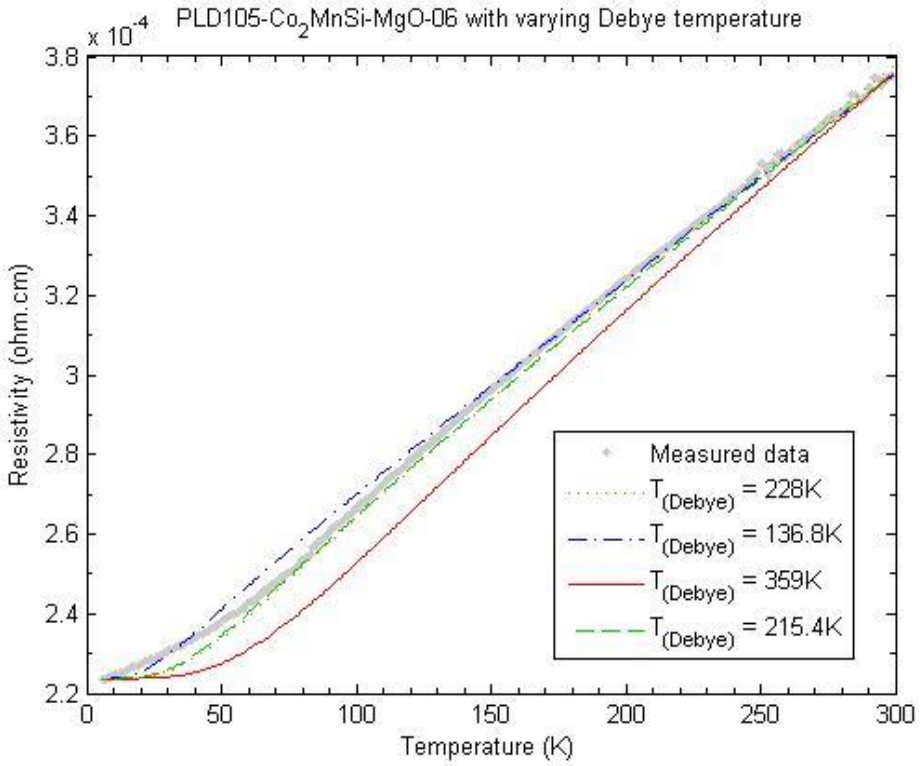

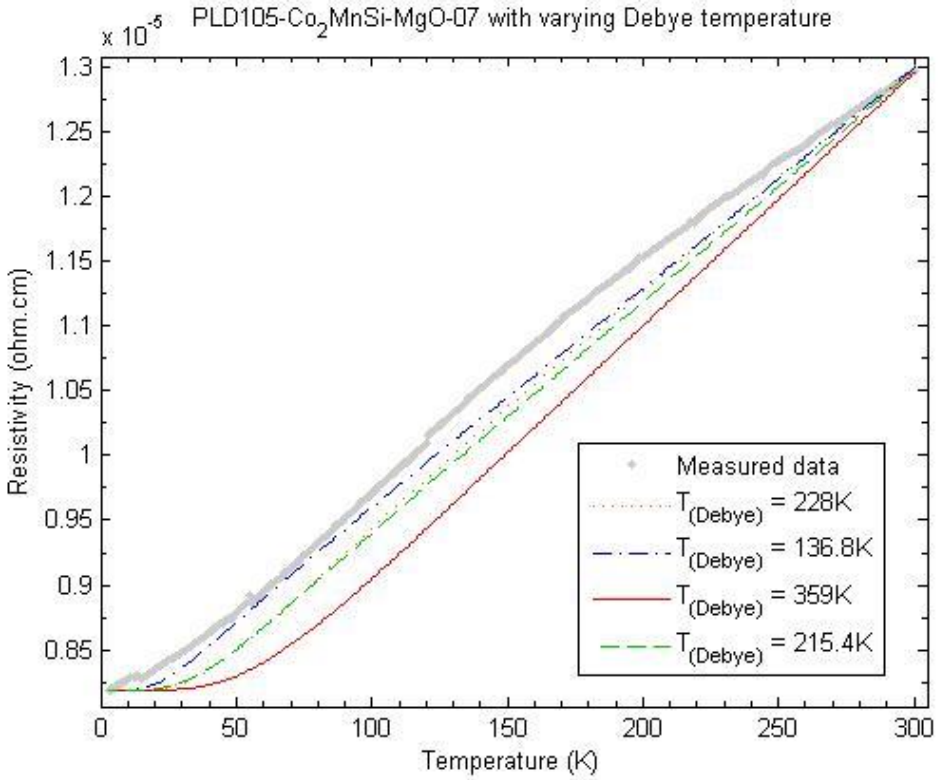
PLD105-Co2MnSi-MgO-07 with varying Debye temperature
x 10-5
Resistivity (ohm.cm)
Temperature (K)
Measured data
T(Debye) = 228K
T(Debye) = 136.8K
T(Debye) = 359K
T(Debye) = 215.4K

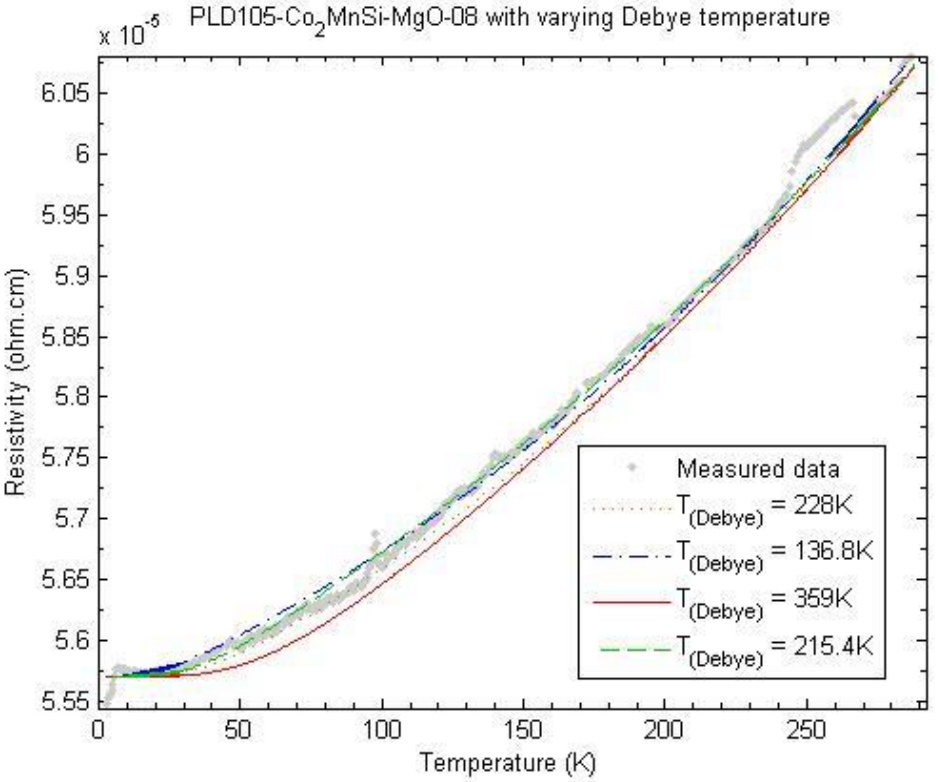
PLD105-Co2MnSi-MgO-08 with varying Debye temperature
x 10-5
Resistivity (ohm.cm)
Temperature (K)
Measured data
T(Debye) = 228K
T(Debye) = 136.8K
T(Debye) = 359K
T(Debye) = 215.4K

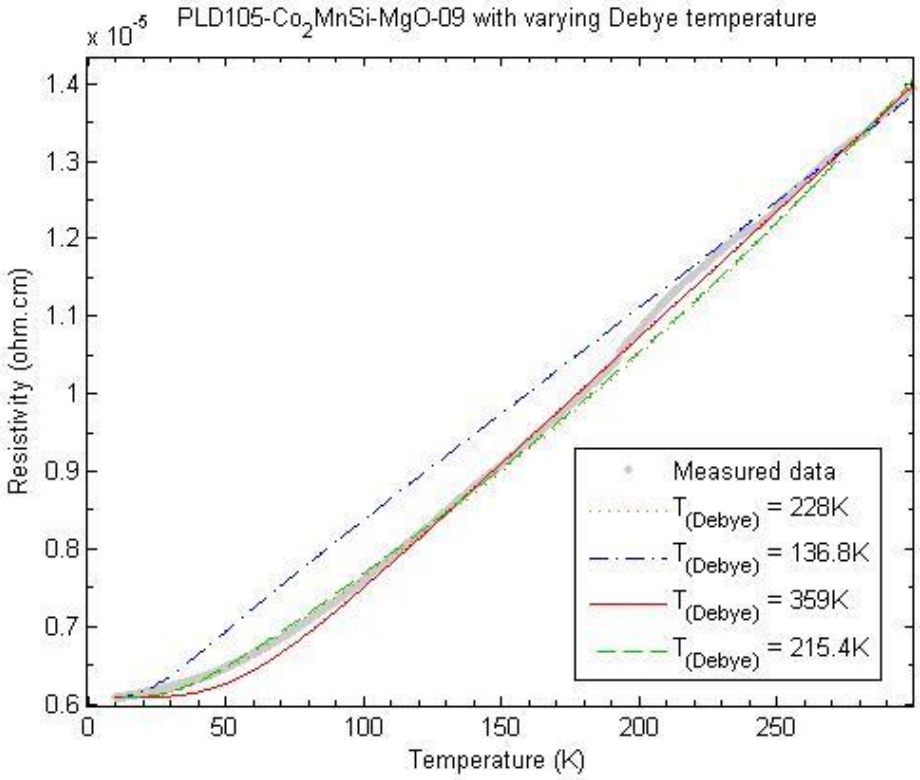
PLD105-Co2MnSi-MgO-09 with varying Debye temperature
x 10^-5
Resistivity (ohm.cm)
Temperature (K)
Measured data
T(Debye) = 228K
T(Debye) = 136.8K
T(Debye) = 359K
T(Debye) = 215.4K

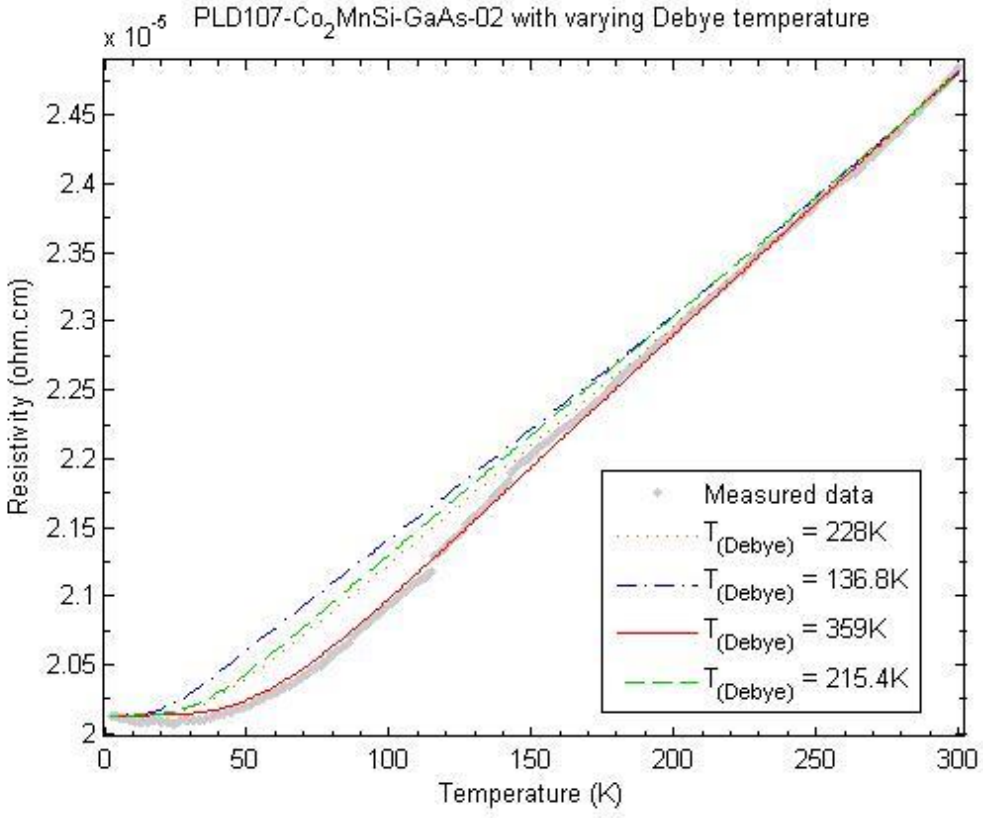
PLD107-Co2MnSi-GaAs-02 with varying Debye temperature
x 10^-5
Resistivity (ohm.cm)
Temperature (K)
Measured data
T(Debye) = 228K
T(Debye) = 136.8K
T(Debye) = 359K
T(Debye) = 215.4K

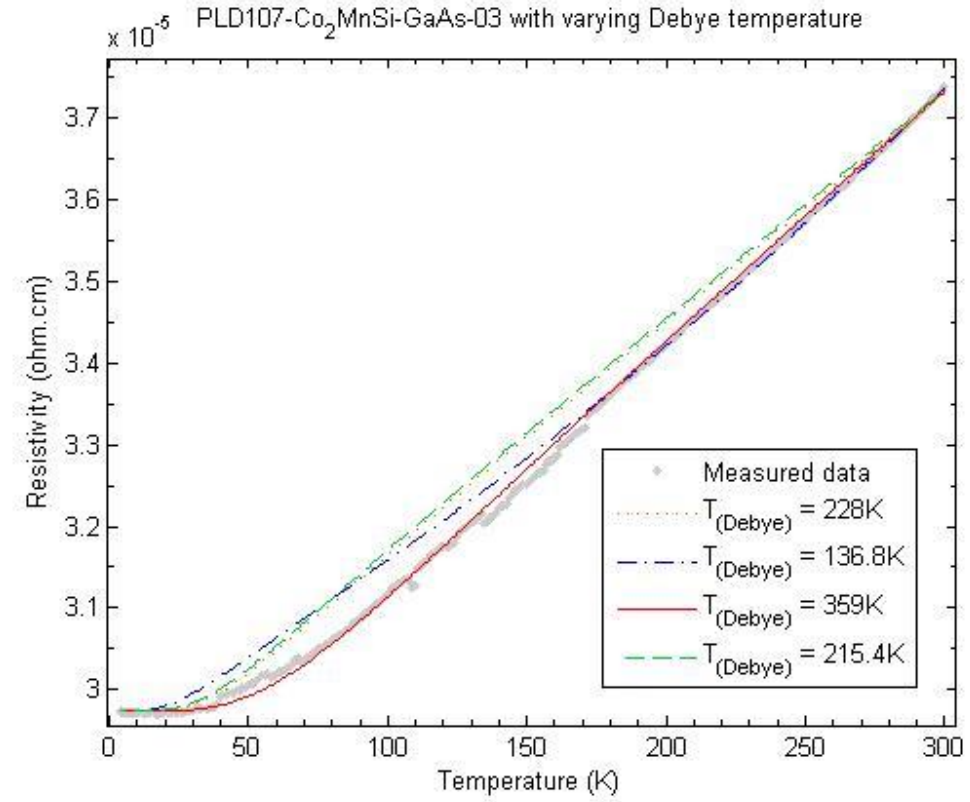
PLD107-Co2MnSi-GaAs-03 with varying Debye temperature
x 10-5
Resistivity (ohm.cm)
Temperature (K)
Measured data
T(Debye) = 228K
T(Debye) = 136.8K
T(Debye) = 359K
T(Debye) = 215.4K

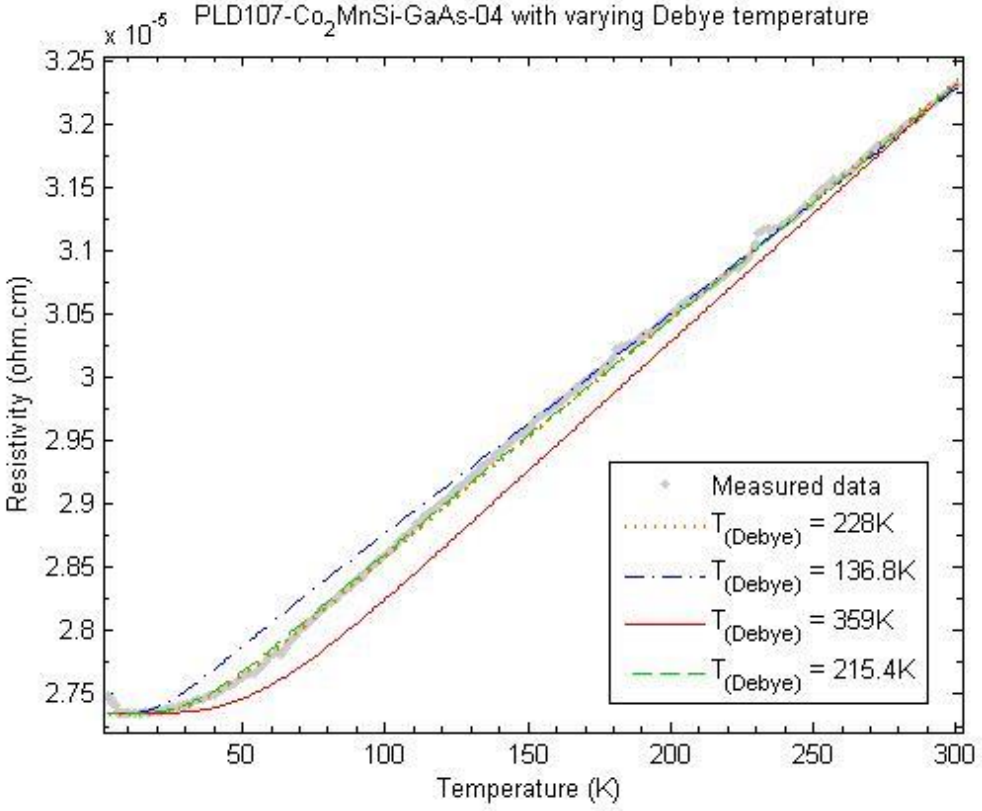
PLD107-Co2MnSi-GaAs-04 with varying Debye temperature
x 10-5
Resistivity (ohm.cm)
Temperature (K)
Measured data
T(Debye) = 228K
T(Debye) = 136.8K
T(Debye) = 359K
T(Debye) = 215.4K

Fig 4.28 – 4.34: Repeating the fitting process for the four Debye temperatures for Co_2MnSi grown on MgO (PLD105) and GaAs (PLD107) respectively. The fitting parameters are listed in table 4.8.

Sample	Θ_D = 228K				Θ_D = 136.8K				Θ_D = 359K				Θ_D = 215.4K			
	ρ0 (ohm. cm) 10^{-6}	A (ohm .cm) 10^{-5}	C (ohm .cm) 10^{-12}	Egap (K)	ρ0 (ohm. cm) 10^{-6}	A (ohm. cm) 10^{-5}	C (ohm. cm) 10^{-12}	Egap (K)	ρ0 (ohm. cm) 10^{-6}	A (ohm .cm) 10^{-5}	C (ohm .cm) 10^{-12}	Egap (K)	ρ0 (ohm.cm) 10^{-6}	A (ohm .cm) 10^{-5}	C (ohm .cm) 10^{-12}	Egap (K)
PLD105_06	223.7	48.3	5	100	223.7	28.0	5	100	223.7	78.8	5	100	223.7	45.0	5	100
PLD105_07	8.187	1.50	0. 5	100	8.187	0.85	3	100	8.187	2.30	5	100	8.187	1.32	5	100
PLD105_08	55.70	0.88	42	100	55.70	0.54	40	100	55.70	1.77	30	100	55.70	1.01	30	100
PLD105_09	6.082	1.69	40	100	6.082	1.38	5	100	6.082	3.76	10	100	6.082	1.60	40	100
PLD107_02	20.13	1.28	9	100	20.13	0.76	9	100	20.14	2.26	5	100	20.13	1.27	6	100
PLD107_03	29.74	2.27	5	100	29.74	1.05	30	100	29.74	3.76	5	100	29.74	2.15	5	100
PLD107_04	27.35	1.47	5	100	27.35	0.85	5	100	27.35	2.40	5	100	27.35	1.37	5	100

Table 4.8: Fitting parameters obtained for different Debye values of Co_2MnSi grown on MgO and GaAs.

Sample	Fluence (J/cm^2)	T_s (˚C)	Thickness (nm)	Debye value
PLD105 _06	6.50	700	90	Between 215.4k and 136.8K
PLD105 _07	4.57	700	66	136.8K
PLD105 _08	5.09	450	56	Between 228K and 215.4K
PLD105 _09	6.53	200	107	Between 359K and 215.4K
PLD107_01	3.51	200	62	n/a
PLD107_02	2.6773	450	29	359K
PLD107 _03	2.6451	700	26	359K
PLD107_ 04	4.3723	575	-	228K

Table 4.9: The optimum Debye value which best modelled the data is stated for each sample. The growth parameters for Co_2MnSi thin films on MgO and GaAs are summarised for comparison.

Comparing the optimum Debye values summarised in table 4.9, there was no clear trend as to whether the thin film samples better modelled a 50% or 70% decrease of the Debye temperature at the film surface. The quality of the crystalline structure is strongly

influenced by the chosen growth parameters rather than the thickness of the sample, resistivity will be an important in order to produce thin films of Co_2MnSi that

Optimising the resistivity of the samples requires thin films of Co_2MnSi with improved crystal quality regardless of the Debye temperature value. This is highlighted by the non-linear curve temperature dependent resistivity of PLD107_01 in fig 4.23 relative to the other Co_2MnSi thin films. Determining which growth parameters result in less defective crystalline thin films is the next important step.

4.6 Summary

The physical and magnetic properties of Co_2MnSi and Co_2MnGa thin films grown on both MgO and GaAs substrates were investigated. A combination of *in-situ* RHEED and SEM images determined that all the samples grown with a minimum of both a ~4.5 J/cm² fluence and 450°C substrate temperature produced epitaxial Co_2MnSi films for both MgO and GaAs substrates. The same results were found to produce epitaxial Co_2MnGa films, although growth orientation did not appear to be very sensitive to changes in fluence.

X-ray diffraction scans only resolved the fundamental (400) Co_2MnSi peak and superlattice (200) Co_2MnGa peak for PLD105_07 which was grown on MgO at 700°C with 4.57 J/cm². Due to the very small lattice mismatch of 0.02%, the Co_2MnSi film peaks could not be clearly resolved from the GaAs substrate peaks. There was evidence of peak shoulders and general broadening of the GaAs (200) and (400) peak reflections which suggested the existence of Co_2MnSi film peaks despite these peaks being un-resolvable for analysis.

From magnetisation measurements, the M_S values of Co_2MnSi thin films grown on MgO and GaAs were found to be 4.65±0.83 μ_B/f.u. and 3.54±1.36 μ_B/f.u. respectively. The MgO value agrees within uncertainty with the theoretically predicted Co_2MnSi magnetic moment of 5.07 μ_B/f.u.[6], whereas Co_2MnSi on GaAs is 3% lower than this value. Both results agree with other M_S values published in the literature which range from 4.95 – 5.10 μ_B/f.u [9]. Overall the thin films grown at 450°C with a high fluence produced the highest magnetic moments for both M_S and M_R with the smallest H_C fields.

The temperature dependent resistivity of the Co_2MnSi grown on MgO and GaAs was investigated from 10K to 300K. The general trend confirmed these thin films exhibit ferromagnetic behaviour as the resistivity monotonically increased with temperature. The general equation describing the resistivity behaviour of a metal was compared to the temperature dependent data. Observing different variations of the equation confirmed that adding a term for the spin flips by including a parameter for the energy gap in the minority state was necessary to produce a good fit to the Co_2MnSi data. This evidence supports the half-metallic nature of Co_2MnSi.

The growth parameters which produced the highest M_S values were found to be thin films grown at 450°C for both MgO and GaAs. The variance of the M_S value did not appear to be very sensitive to fluence, but a film on the order of ~50nm thick was necessary to produce reliable M_S results.

Chapter 5

Co_2MnGa

5.1 Growth parameters and sample list

A series of thin films of Co_2MnGa were grown using PLD. The growth quality of these films was investigated by varying three parameters: substrate choice, substrate growth temperature and laser fluence.

In total, three films were grown on MgO substrates and three films were grown on GaAs substrates. The substrate temperature was set to 450˚C and 700˚C during sample growth and the laser fluence ranged from ~ 2 - 6 J/cm². Average growth time was standardised at a minimum of 1 hour. This value was increased only if *in-situ* RHEED imaging suggested the deposit rate was too slow and the film would be too thin to provide an accurate analysis of the samples properties. Prior to each growth, the Co_2MnGa target was pre-ablated. The KrF laser was set at 200mJ with a pulse rate of 10Hz for 5 minutes to remove any impurities or oxidation on the target surface which could contaminate the sample during growth.

A combination of single layer and bi-layer films were grown using PLD to investigate whether a buffer layer of material between the film substrate improved the deposited crystal structure of the film. The $L2_1$ crystal structure is an important factor for producing half-metallic Heusler thin films with 100% spin polarisation as the density of states of Co_2MnGa is considered to just meet the criteria for half-metallic behaviour at E_F. The introduction of buffer layers can improve film relaxation and overall structure and are intended to positively influence the physical and magnetic properties of Co_2MnGa thin films grown in this thesis. The buffer layer was chosen as a combination of low and high temperature growth as high temperature growth in literature was associated with films that had strong magnetic properties and low temperature growth was associated with well-matched stoichiometrically accurate high quality films [35].

For each bi-layer sample, the growth time of the main film layer was standardised to be 1 hour. This time was chosen to allow direct comparison between single layer and bi-layer films in terms of deposition rate and film thickness. The growth time of the buffer layer was chosen to be 12 minutes or 20% of the main layer, as the buffer layer need to be thick enough to influence the relaxation of the main film layer. *In-situ* RHEED imaging usually shows the most rapid change from the initial substrate image during the first 12 minutes of the growth, suggesting this timeframe is important for developing a well relaxed deposited film on a substrate.

Sample	Substrate type	Substrate temperature (˚C)	Growth time (hr)	Film thickness ±10 (nm)	Fluence (J/cm²)	Fluence uncertainty (J/cm²)
PLD115 _01	MgO	700	1	68	5.18	0.33
PLD115 _02	MgO	450	1	30	2.76	0.22
PLD115 _03	MgO	450 Buffer/ 700	0.2/1	20	1.95	0.18
PLD116_01	GaAs	700	1	65	4.79	0.31
PLD116 _02	GaAs	450	1	36	3.30	0.25
PLD116_03	GaAs	450 Buffer/ 700	0.2/2	47	6.29	0.39

Table 5.1: The three varied growth parameters for the series of thin films Co_2MnGa samples grown using PLD.

5.2 Structural characterisation

5.2.1 RHEED images

In-Situ RHEED was used to closely monitor the sample growth during the first two minutes and an image taken every ten seconds regardless of the image details.

The initial growth layers are useful for comparing how quickly the growth commenced by observing how quickly the substrate reflection image changes. The spacing of the n=1 diffraction features from the images can be extracted to observe the initial relaxation strain when the film began layered growth rather than directly on the substrate.

Fig 5.1 shows the end of the growth RHEED images for the Co_2MnGa thin film series grown on MgO substrates. The growth parameters of these films are listed in table 5.1.

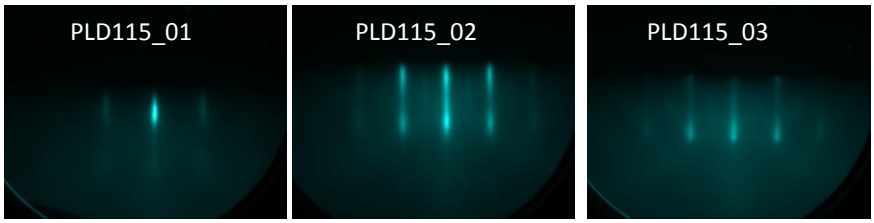

Fig 5.1: RHEED images taken at the film growth termination for films PLD115_01, PLD115_02 and PLD115_03.

Each sample developed RHEED images with streak features, which are a characteristic associated with epitaxial surface growth. The suggested sample thickness from the clarity of the streak features in each samples RHEED image is correlates well with the measured RBS values. The streak features in images PLD115_02 and PLD115_03 are noticeably blurrier than PLD115_01, which is approximately double the thickness of the other two samples and is more likely to consist of well orientated complete layers of film.
The streak features in the RHEED images suggest that the samples do not appear to be very sensitive to this range of substrate growth temperature or fluence, however as expected a higher fluence does produce a thicker film due to more target material being ablated per pulse by a higher energy per unit area.

Fig 5.2 shows the end of the growth RHEED images for the Co_2MnGa thin film series grown on GaAs substrates. The growth parameters of these films are listed in table 5.1.

Fig 5.2: RHEED images taken at growth termination for films PLD116_01, PLD116_02 and PLD116_03.

The main film layers of PLD116_01 and PLD116_03 were both grown using a combination of a 700°C substrate temperature with a high fluence. Extra diffraction lines have developed between the n=0 and n=1 lines (fig 5.2) which are attributed to Heusler thin

films considered to have high quality crystalline structure [21]. Co_2MnGa and GaAs differ in atomic spacing by 2% which may be an optimal lattice mismatch between the film and the substrate. The strong Kikuchi diffraction lines featured in fig 5.2 of PLD116_01 are associated with long range crystalline order in a thin film [3]. Faint Kikuchi lines appear to be developing in the RHEED image of PLD116_03, the lower intensity of these lines are most likely a result of PLD116_03 being a thinner film than PLD116_01.

PLD116_02 is only film with a main layer grown using a 450°C substrate temperature and features faint lines developing between the n=0 and n=1 lines similar to the strong extra lines featured in the RHEED images of PLD116_01 and PLD116_03. The RHEED images suggest a higher growth temperature is necessary for the intensity of the extra lines to develop and be clearly visible.

Overall the RHEED study suggests higher quality Co_2MnGa films are grown on GaAs substrates rather than MgO. For GaAs substrates the use of a buffer layer did not seem to be particularly necessary as the lattice mismatch is small. Unfortunately for MgO substrates where a buffer layer might have been useful, a direct comparison cannot be made as these films were grown using a laser fluence that is too low to compare directly with the single layer film.

5.2.2 SEM images

SEM images of the Co_2MnGa thin films grown on MgO substrates at various magnifications are displayed below:

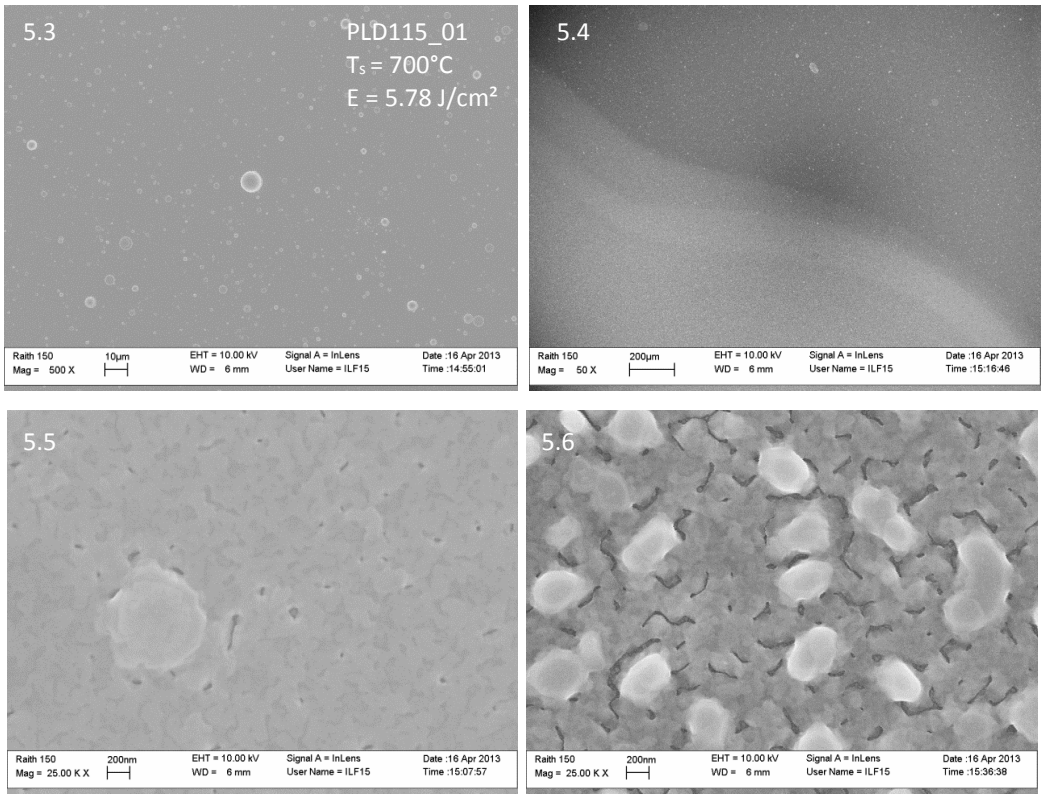

Fig 5.3 – 5.6: SEM images at different magnifications and surface locations of PLD115_01.

The SEM images of PLD115_01 show a heavily particulated film (fig 5.3) with regions of inhomogeneity that are highlighted by the clear boundaries of different film growth (fig 5.4). The inhomogeneity continues at 50 000x magnification (fig 5.5 – 5.6) the most likely reason for this variation is a combination of the spatial variation inherent to PLD combined with variations in the thermal contact.

The crystallite size for PLD115_01 of 18nm is larger than the other Co_2MnGa samples in this series. This size seems reasonable as the majority of the film surface is smooth (fig 5.3, fig 5.5) with a low population of pits. The region of poor thermal contact which produced a very rough surface was small and isolated relative to the whole film surface (fig 5.4, fig 5.6).

The following SEM images for the film PLD115_02 are shown at two magnifications in fig 5.7 - 5.8.

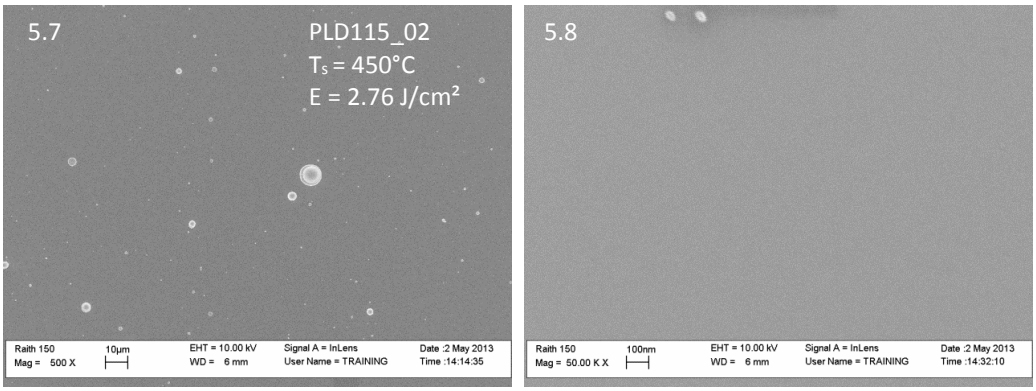

Fig 5.7 – 5.8: SEM images at 500x and 50 000x magnifications of PLD115_02.

The smooth surface appearance and low population of particulates on PLD115_02 is a result of the low growth fluence. The crystallite size of PLD115_02 was calculated to be 11nm. Some features approximately ~20nm in size can sometimes be seen at 50 000x magnification but smooth features on the order of ~10nm are too small to be easily resolved and produce grainy dull images. Two particulates were captured at the top left corner of fig 5.8. The ripples along the edges of these particulates are caused by noise in the system which limits the magnification resolution.

The SEM images of the film PLD115_03 are shown in fig 5.9 – 5.10 at 500x and 50 000x magnifications. The images show smooth shallow channels and a moderate density of particulates of various sizes.

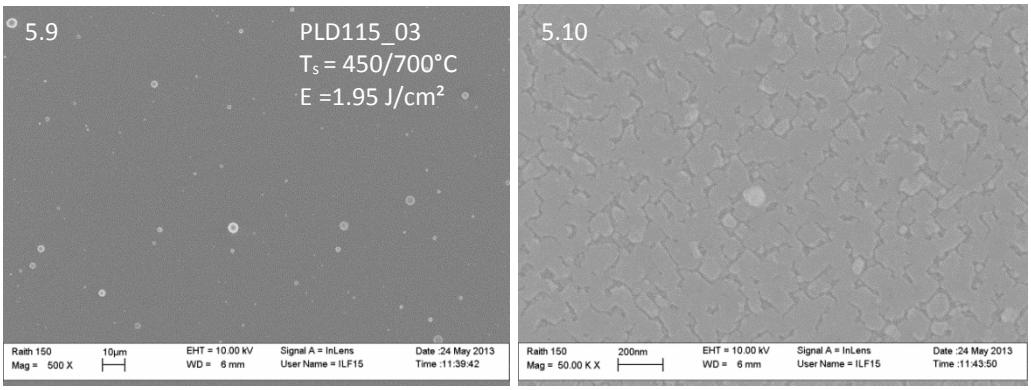

Fig 5.9 –5.10: Surface images of PLD115_03 at two magnifications. The channels have rippling edges at 50 000x magnification caused by noise.

The crystallite size of PLD115_03 was calculated to be 11nm throughout the film. Despite the low fluence, there is some larger scale structure on the film surface that was resolvable

at 50 000x magnification (fig 5.10). This structure is quite smooth and very shallow, and appears to be of a similar structure to PLD115_01 as both main layer films were grown at 700°C.

Table 5.2 summarises the general features of the PLD115 series and their SEM characteristics. Each film was confirmed to have a smooth surface with a complete growth layer with little or no pits.

Sample	Fluence (J/cm²)	T_s (˚C)	Thickness ±10 (nm)	RHEED detail	Crystallite size (nm)	SEM detail
PLD115_01	5.18	700	68	Streaks	18	Few ~20nm wide pits. High density of various particulate sizes
PLD115_02	2.76	450	30	Streaks	11	Smooth featureless surface. Moderate density of various particulate sizes
PLD115_03	1.95	450 Buffer/ 700	20	Streaks	11	Smooth channel features. Moderate density of various particulate sizes

Table 5.2: Summary of growth parameters, RHEED details and SEM image features of Co_2MnGa thin films grown on MgO.

SEM images of Co_2MnGa films grown on GaAs substrates are shown in fig 5.11 – 5.16 at various magnifications.

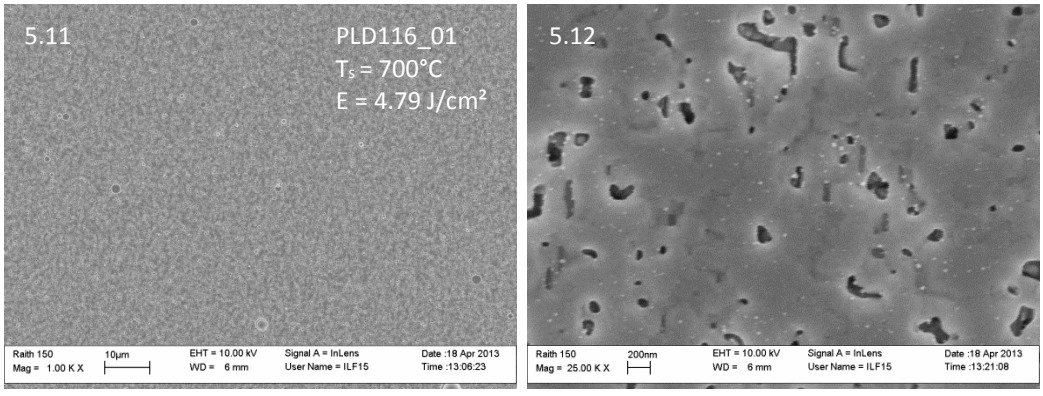

Fig 5.11 – 5.12: SEM images of the film PLD116_01 at 1000x and 25 000x magnifications.

Surface images of PLD116_01 show a very low density particulated film with many small pits (5.11). The surface film layer appears to be extremely thin as large channel structures can be resolved underneath sections closest to the pits. There is a high density of pits in the surface of the film which average ~20nm in size.

The crystallite size of PLD115_01 throughout the film was calculated to be 18nm, this seems reasonable given the average size of the pits are ~20nm, and the channel structures closely resemble PLD115_01 which also had a crystallite size of 18nm.

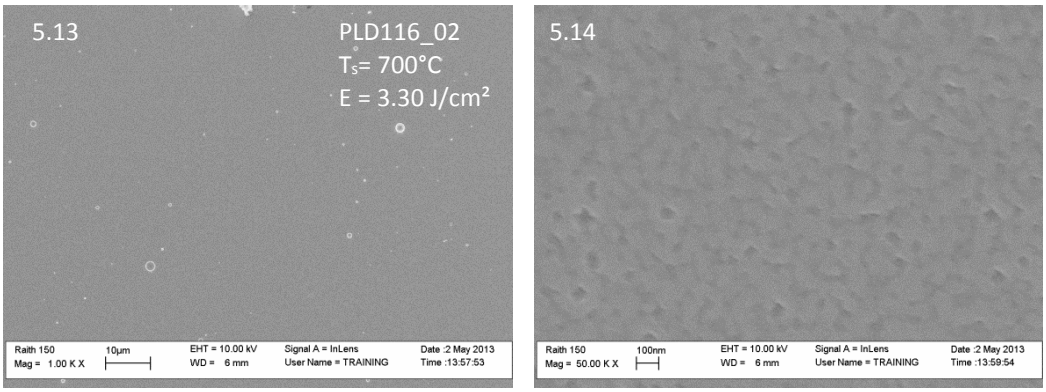

Fig 5.13 - 5.14: SEM images of the film PLD116_02 at 1000x and 50 000x magnifications.

Surface images of PLD116_02 show a moderate density particulated film with no pits (5.13). The surface layer is much smoother but retains the shape of the channel structures (5.14).

The crystallite size of PLD115_02 was calculated to be 17nm. The film surface appears smooth and forms a complete layer across the entire film with no pits. The shallow channel structure on the film surface is similar those in other SEM images of the Co_2MnGa thin film series.

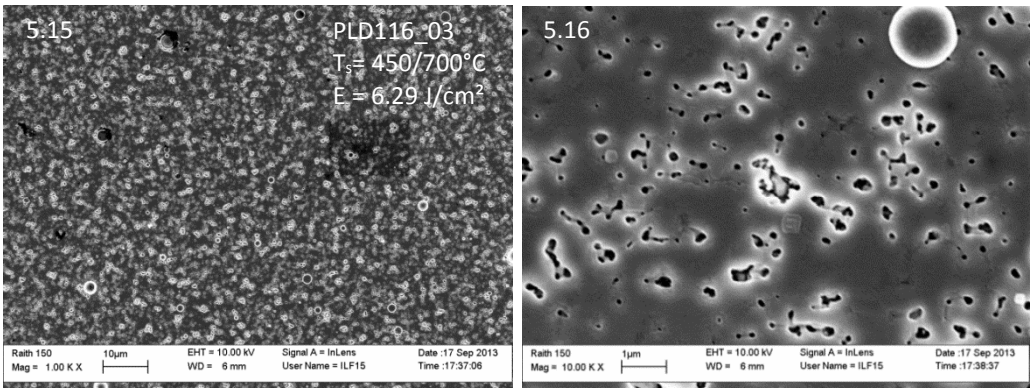

Fig 5.15 – 5.16: SEM images of the film PLD116_03 at 1000x and 10 000x magnifications.

Surface images of PLD116_03 present a very low density particulated film with many deep small scale pits (left). The film surface layer appears very dense with large grain-like structures visible near the pits in the film surface. The average pit size is ~100nm.

The crystallite size for PLD116_03 is 13nm and relates well to the large grain structures beneath the pitted film surface layer. Both PLD116_01 and PLD116_03 have regular surface pits across the entire film surfaces which are resolvable at 1000x magnification (fig 5.12, fig 5.16).

Table 5.3 summarises the general features of the PLD116 series and their SEM characteristics. Both PLD116_01 and PLD116_03 had regular small scale pits across the entire film surface.

Sample	Fluence (J/cm²)	T_s(˚C)	Thickness ±10 (nm)	RHEED detail	Crystallite size (nm)	SEM detail
PLD116_01	4.79	700	65	Streaks	18	Many ~20nm wide pits. Low density of small ~1µm particulates
PLD116_02	3.30	450	36	Streaks	17	Moderately smooth surface with resolved channel features and no pits. Moderate density of ~0.5µm particulates
PLD116_03	6.29	450 Buffer/ 700	47	Streaks	13	Many ~100nm wide pits. Low density of small ~1µm particulates

Table 5.3: Summary of growth parameter, RHEED details and SEM images features of Co_2MnGa grown on GaAs.

Pits tended to be a common feature in Co_2MnGa thin films grown on GaAs. They were only present in the SEM image of PLD115_01 grown on MgO where there was a region of poor thermal contact (fig 5.4, fig 5.6). Overall the MgO film surfaces appeared very smooth and uniform. The surface pits were predominantly apparent in the GaAs films grown at 700°C at a similar fluence of 4.79 and 5.78 J/cm² (fig 5.12, fig 5.16). As such these films were also of a similar thickness.

5.3 X-ray diffraction characterisation

X-ray diffraction measurements were done on all the Co_2MnGa films to further understand their physical properties. Films from the PLD116 series grown on GaAs substrates are presented in fig 5.17 and fig 5.18.

Film peaks are present in the θ to 2θ scans for all PLD116 samples, as the lattice mismatch of 2% for Co_2MnGa is sufficiently large to resolve film peaks from the proximity of the GaAs substrate peaks. The multiple GaAs substrate peaks are again caused by the Co $K\alpha_1$ and Co $K\alpha_2$ X-rays components. The peaks in fig 5.17 and fig 5.18 have been shifted to align with the largest GaAs substrate peak caused by Co $K\alpha_1$ radiation.

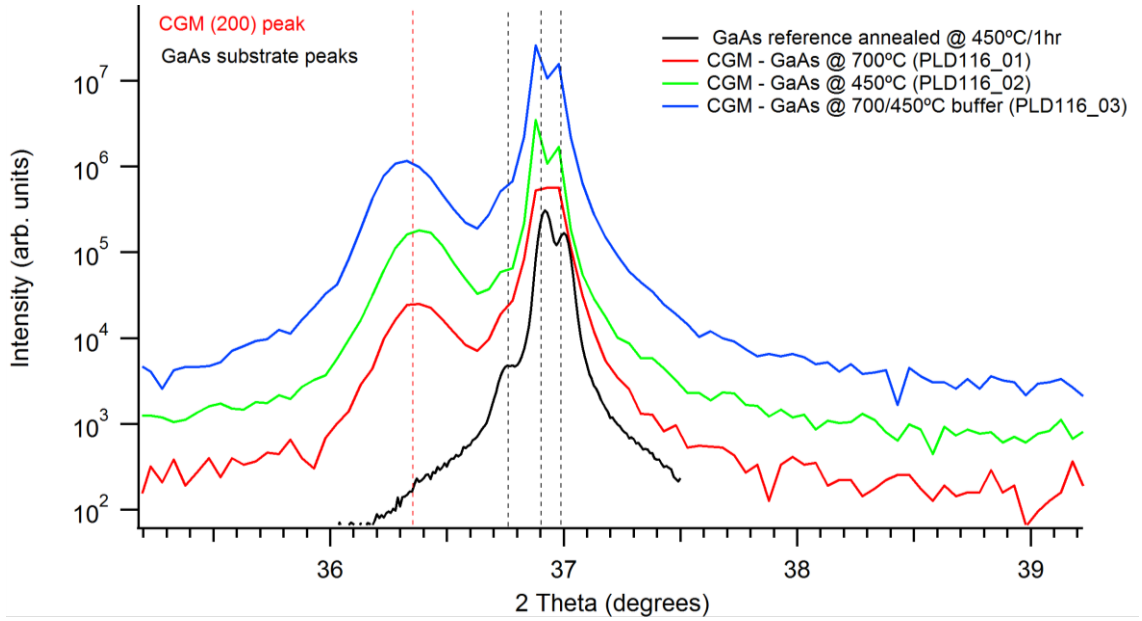

Fig 5.17: XRD of the (200) peak region for Co_2MnGa films grown on GaAs substrates. The peaks have been offset for clarity.

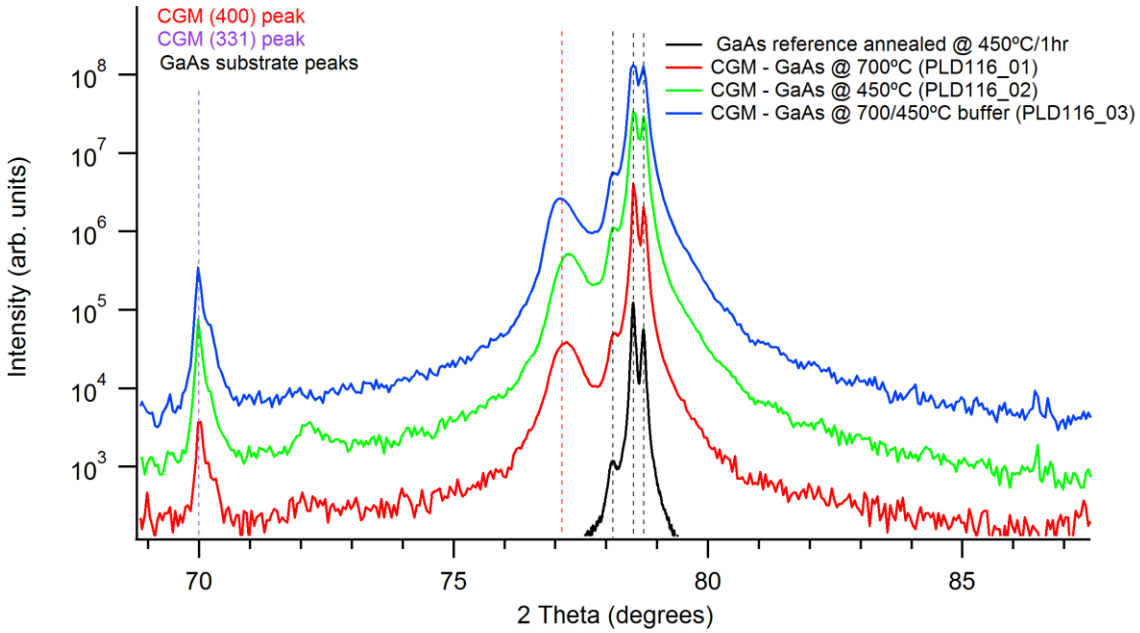

Fig 5.18: XRD of the (400) peak region for Co_2MnGa films grown on GaAs substrates. The peaks have been offset for clarity.

The presence of the (200) peak within all the samples is associated with a high degree of crystal order within the film structure [7]. The superlattice (200) bulk Co_2MnGa peaks are noticeably sharper and more defined than the fundamental (400) peaks [33]. There is a strong peak located at 70° which has been thought to be a (331) film peak that is associated with thin films structured as an L2 crystal structure [34].

Bulk Co_2MnGa crystal has a lattice constant of 5.77Å [10]. A film lattice constant can be calculated from the position of the (200) and (400) XRD film peaks and thus the strain can be calculated. Table 5.4 displays the XRD results for the Co_2MnGa films grown on GaAs substrates.

The strain in table 5.4 suggests a trend where the film peaks of the thin films grown at 700°C shift to the left of the bulk Co_2MnGa reference peak line, and the sample grown at 450°C shifts to the right of the bulk Co_2MnGa reference peak line. Introducing a buffer layer resulted in a film (PLD116_03) with the least strain relative to the bulk Co_2MnGa peak, which consequentially is also visible as a combination between the two peak shifts of PLD116_01 and PLD116_02.

Sample	Substrate	Growth temp (°C)	Dominant peak orientation	200 peak (°)	200 strain (%)	400 peak (°)	400 strain (%)	Dominant peak FWHM (rad)	Crystallite size (nm)	Peak area
PLD116_01	GaAs	700	400	36.42	-0.70	77.25	-0.59	0.0117	18	1597.7
PLD116_02	GaAs	450	400	36.41	-0.69	77.35	-0.69	0.0126	17	11300
PLD116_03	GaAs	450/700	400	36.36	-0.54	77.16	-0.49	0.0165	13	58826

Table 5.4: Summary of the (200) and (400) film peak locations. The strain of these peaks was calculated relative to bulk Co_2MnGa.

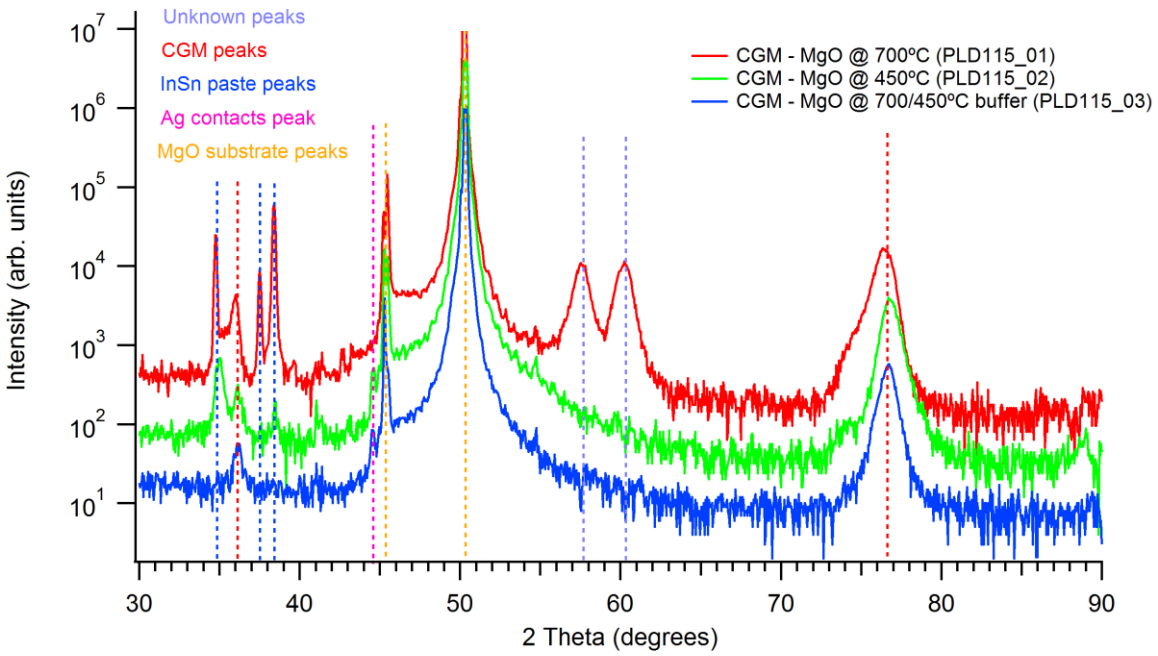

Fig 5.19: Full 2Θ XRD scans of the three Co_2MnGa films grown on MgO substrates. The peaks have been offset for clarity.

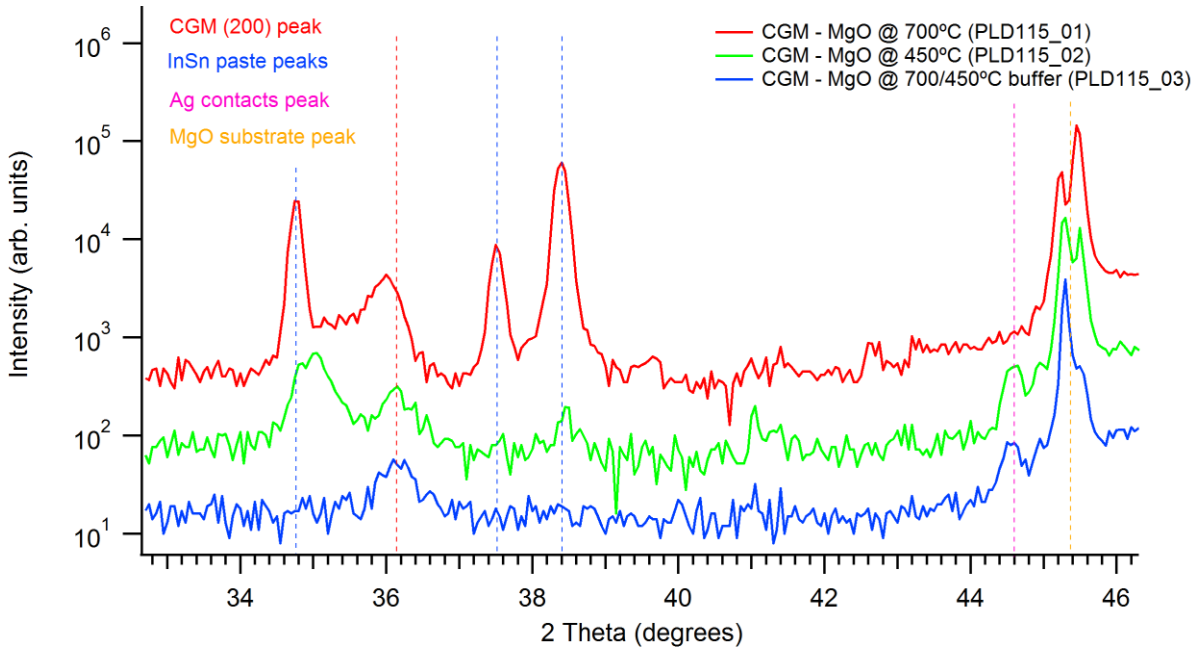

Fig 5.20: XRD of the (200) peak region for Co_2MnGa grown on MgO substrates. The peaks have been offset for clarity.

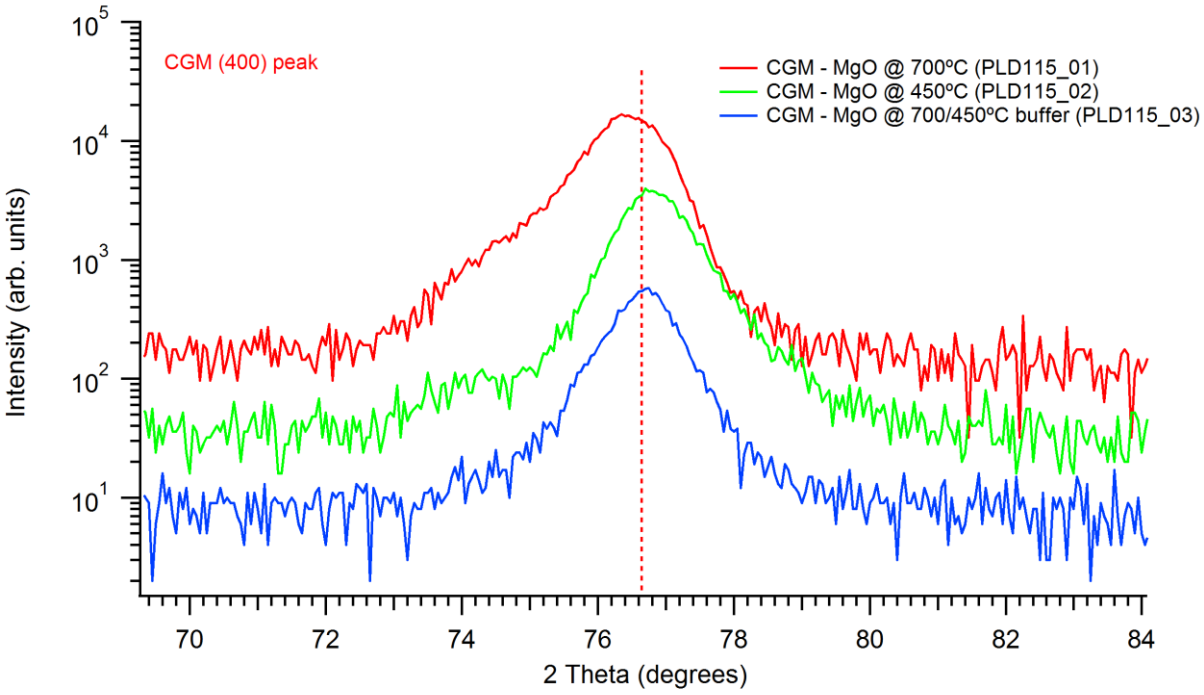

Fig 5.21: XRD of the (400) peak region for Co_2MnGa grown on MgO substrates. The peaks have been offset for clarity.

PLD115_01 includes three extra peaks at 34.8°, 37.55° and 38.4° (fig 5.19) which are solely due to InSn which is used during the growth process to mount the substrate onto the Mo – plate. When mounting the substrate for growth, it is easy for the InSn to gather around the edges of the substrate and at times accidently build up enough to coat the sides or partial surface edge of the substrate. InSn on the film surface is caused purely by accident, hence InSn peaks are not present in all film scans.

PLD115_02 and PLD115_03 include on extra weak peak at 44.5° due to Ag (fig 5.19). These samples were measured using XRD after the films has been prepared for PPMS measurements, which requires four thin contacts of Ag to be evaporated on the surface of the films.

The strength of the Co_2MnGa fundamental (400) film peaks are significantly greater than the Co_2MnGa superlattice (200) film peaks. Comparison of the (200) film peaks in the three PLD115 thin films highlights that both PLD115_02 and PLD115_03 are extremely weak. This result is most likely explained by the ordering of the atoms in the film structure. Having the bulk Co_2MnGa (400) stronger than the (200) peak suggests the film is arranged as a B2 structure [15][33][34].

The peak strain continues to show a trend where the film peak grown at 700°C shifts to the left of the bulk Co_2MnGa peaks, and the sample grown at 450°C shifts to the right of the bulk Co_2MnGa peaks. The PLD115_03 film peak value aligns extremely close (0.002% strain) to bulk Co_2MnGa peak (table 5.5), this suggests that including a buffer layer before growing the main film layer does positively influence the film relaxation.

Sample	Substrate	Growth temp (°C)	Dominant peak orientation	200 peak (°)	200 strain (%)	400 peak (°)	400 strain (%)	Dominant peak FWHM (rad)	Crystallite size (nm)	Peak area
PLD115_01	MgO	700	400	35.95	-2.12	76.42	-0.77	0.0117	18	160.93
PLD115_02	MgO	450	400	36.13	0.06	76.81	-0.11	0.0198	11	1083.9
PLD115_03	MgO	450/700	400	36.15	0.002	76.67	0.04	0.0194	11	606.31

Table 5.5: Summary of the (200) and (400) film peak locations, the strain of these peaks was calculated relative to bulk of Co_2MnGa.

5.4 Magnetic measurements

The magnetic moments of the Co_2MnGa samples were investigated with field sweeps at 10K and 300K in magnetic fields up to 70 KOe using the SQUID magnetometer at Callaghan Innovation.

Field loops up were performed on the entire Co_2MnGa sample series on GaAs and all Co_2MnGa sample series on MgO except for PLD115_01.

Fig 5.22 - 5.25 show the field loop data for the two samples of the Co_2MnGa series grown on MgO substrates. Following in fig 5.26 – 5.29 are the field loops for all three samples of the Co_2MnGa series grown on GaAs substrates.

In general, M_S was the largest for Co_2MnGa thin films grown on MgO substrates and lowest for thin films grown on GaAs substrates. However, uncertainties in the film thickness lead to an overstatement of these values for Co_2MnGa grown on MgO. The maximum M_S found at 10K for each substrate was 6.02±3.01 μ_B/f.u. and 3.60±0.77 μ_B/f.u. for MgO and GaAs respectively.

The M_S value of Co_2MnGa grown on GaAs agrees within uncertainty with the theoretically predicted Co_2MnGa magnetic moment of 4.06 μ_B/f.u. [12] and agrees with other M_S values published in the literature which range from 3.2 – 3.5 μ_B/f.u. [20][21][35].

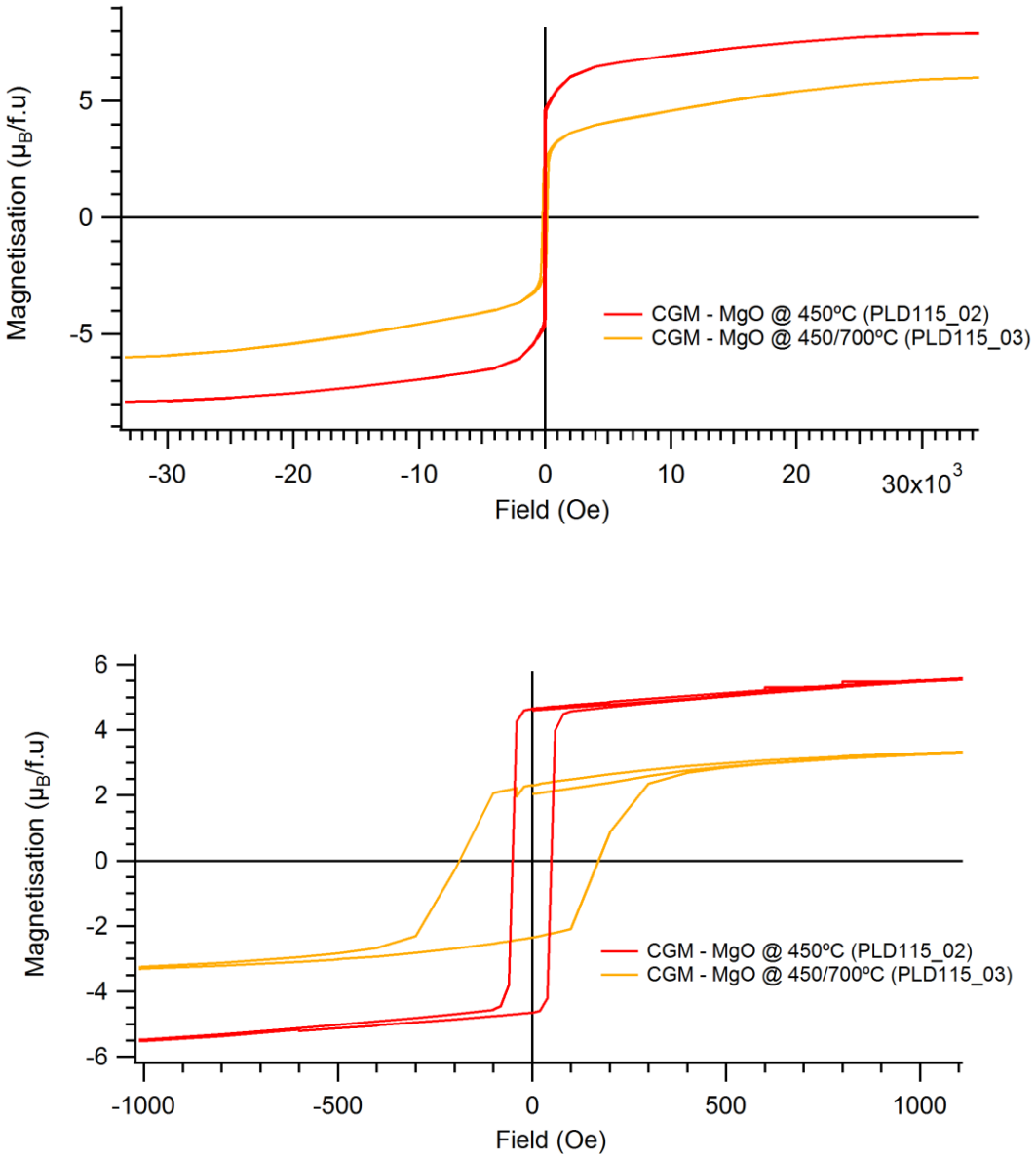

Fig 5.22- 5.23: Hysteresis loops of Co_2MnGa on MgO measured at 10K (above) with a close-up view of the hysteresis loop shape and values of H_C (below).

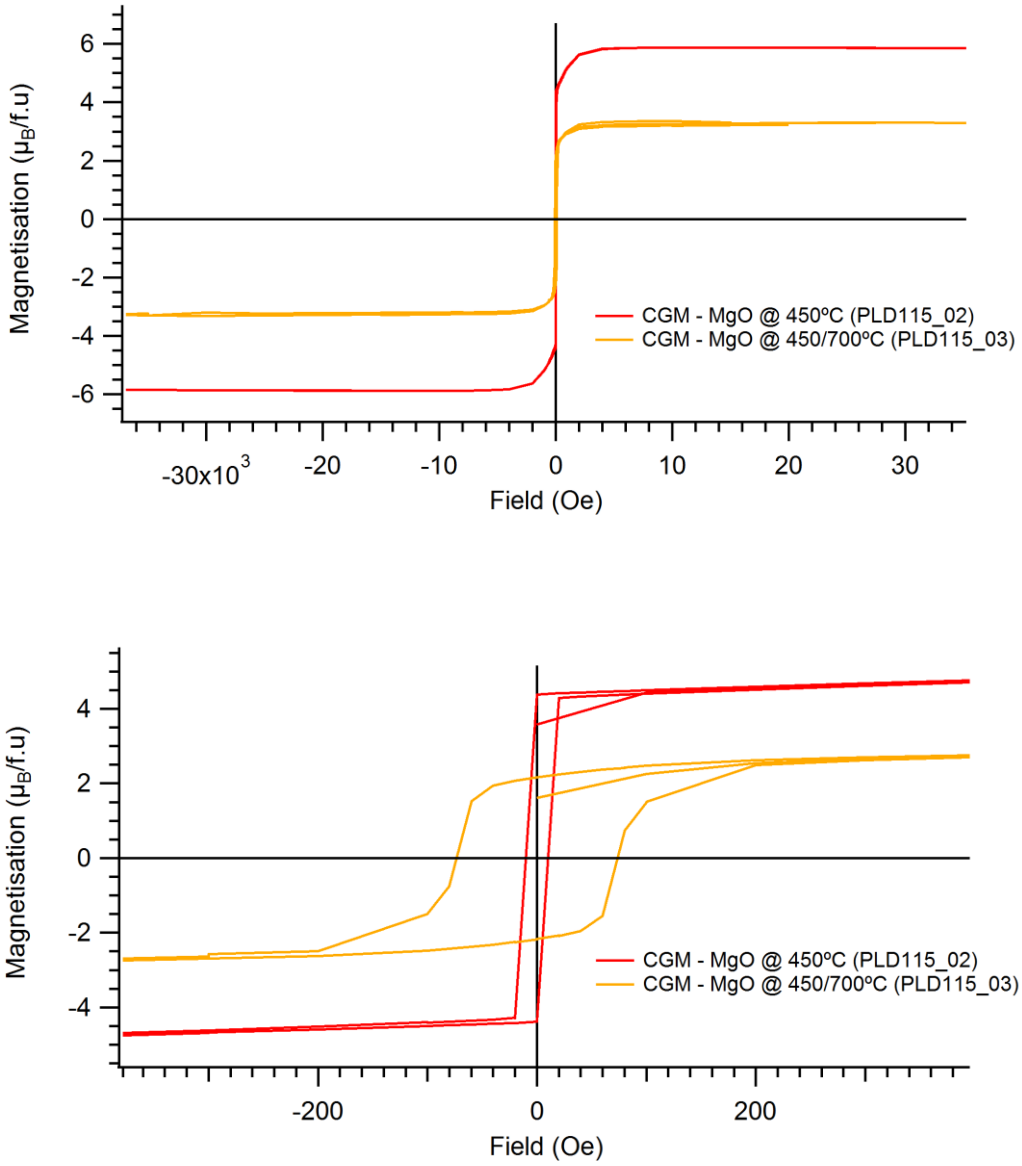

Fig 5.24 – 5.25: Hysteresis loops of Co_2MnGa on MgO measured at 300K (above) with a close-up view of the hysteresis loop shape and values of H_C (below).

The M_S values of the PLD115 series are higher than the stated theoretical value for Co_2MnGa. The overestimation arises from the importance of film thickness when calculating the magnetisation in units of μ_B/f.u., where the film thickness for this series was estimated using RBS to be 20 - 30±10nm. The thickness range contributes to an overall uncertainty of 33 – 50% when determining the magnetic moments in μ_B/f.u.

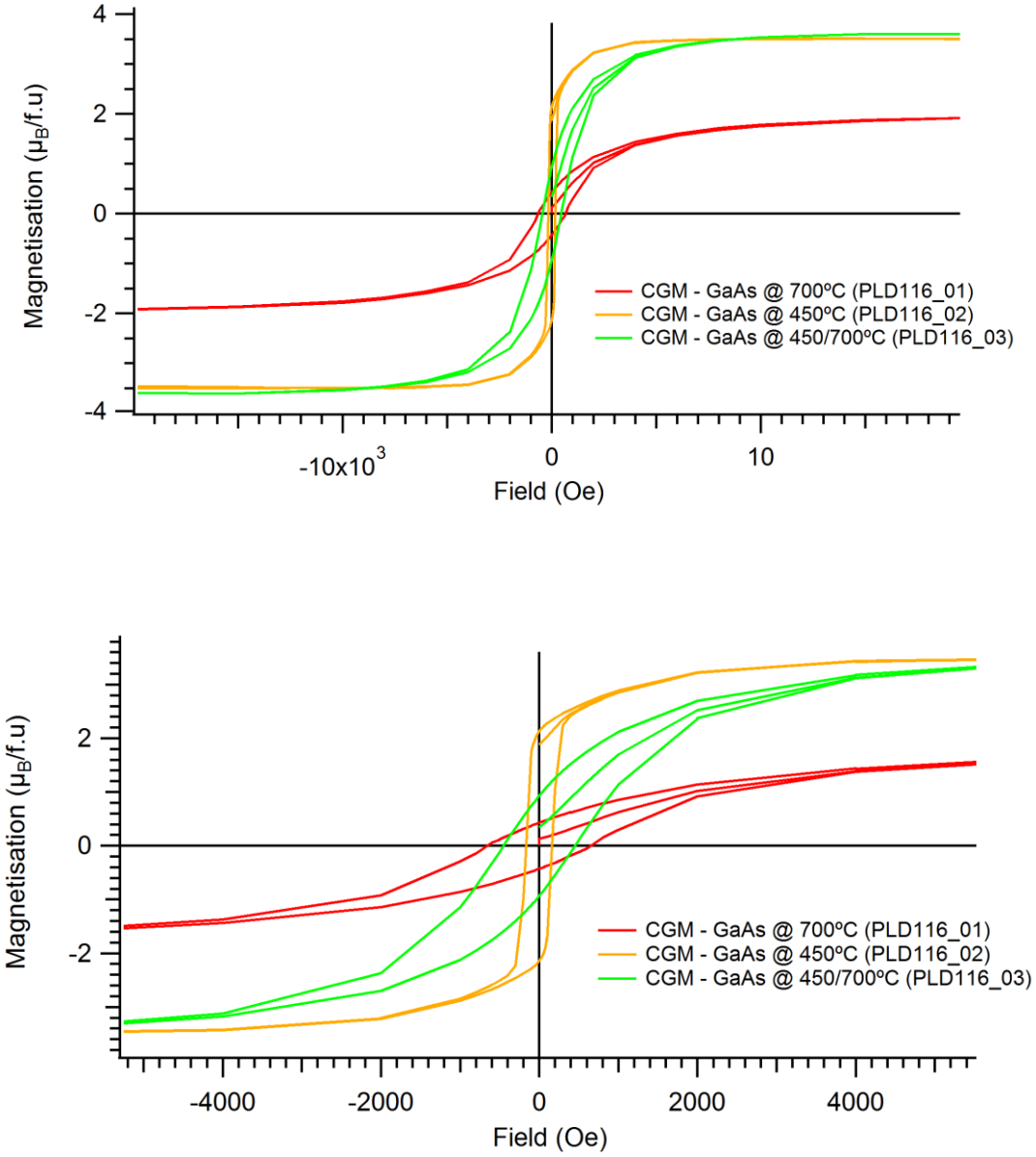

Fig 5.26 – 5.27: Hysteresis loops of Co_2MnGa on GaAs measured at 10K (above) with a close-up view of the hysteresis loop shape and values of H_C (below).

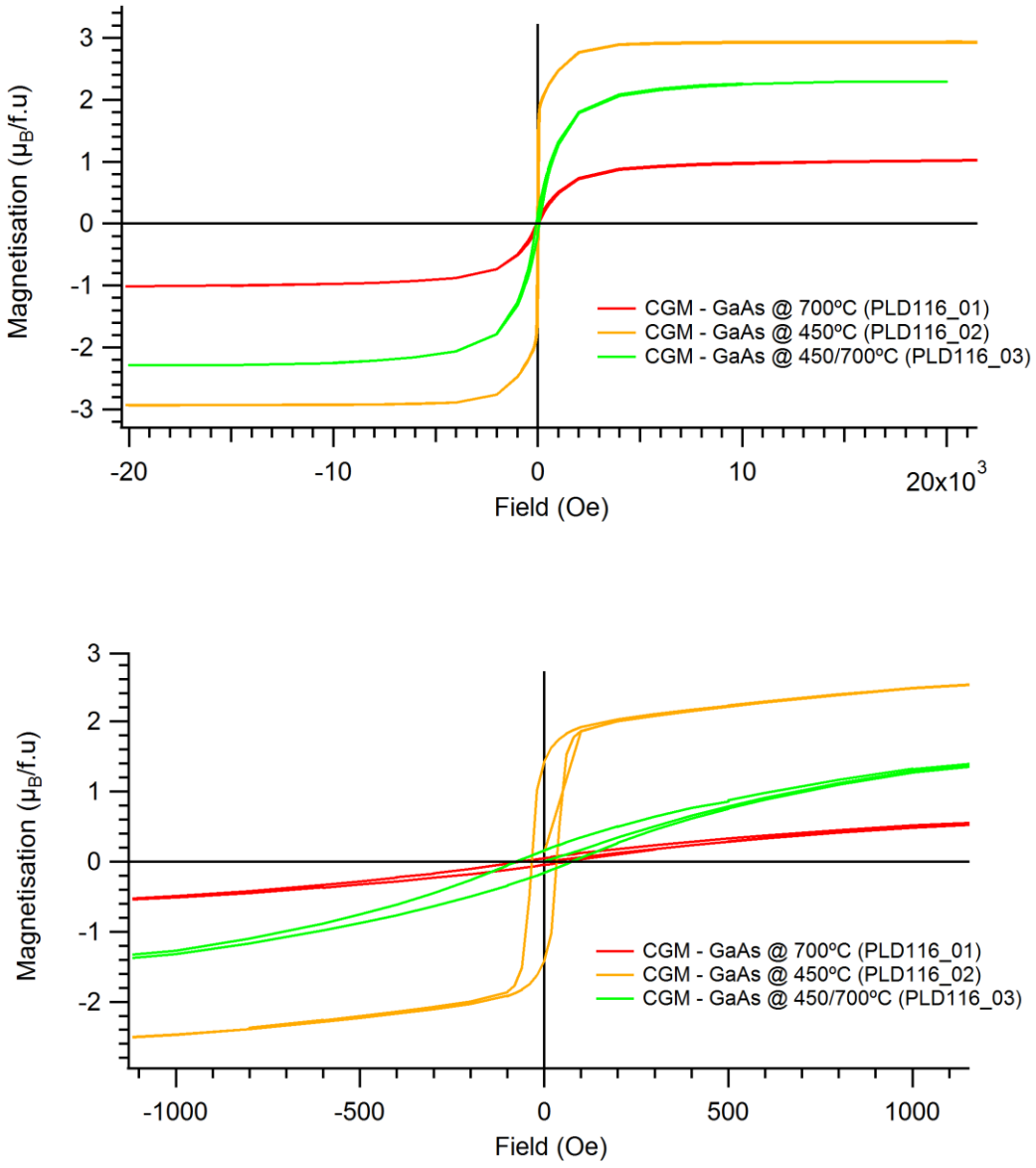

Fig 5.28 – 5.29: Hysteresis loops of Co_2MnGa on GaAs measured at 300K (above) with a close-up view of the hysteresis loop shape and values of H_C (below).

The magnetic hysteresis loops of Co_2MnGa on MgO are square in shape (fig 5.22 – 5.25) and these loops have high M_S values and overall low H_C values. The highest M_S values were produced by the samples grown at 450°C. In particular PLD115_02 has a very square loop profile (fig 5.25) and was grown using a 450°C substrate temperature with a fluence of 2.76 J/cm². These magnetic hysteresis loops are contrasted with the very heavily curved loops of the Co_2MnGa series on GaAs which only has one square profile that is characterised by a large magnetisation (fig 5.29). This sample is PLD116_02 which was also grown at 450°C substrate temperature with slightly higher fluence of 3.30 J/cm².

Each sample of Co_2MnGa grown on MgO and GaAs resulted in a magnetic hysteresis loop at 10K which is a unique feature attributed to ferromagnetic materials. PLD116_01 shows extremely weak ferromagnetic behaviour relative to the other samples in the Co_2MnGa series which is only slightly improved by including a 450°C buffer layer in PLD116_03 (fig 5.26 – 5.29). The main film layer of both samples was grown at a high fluence and a substrate growth temperature of 700°C which is clearly very detrimental to the strong alignment of the magnetic moments in the films and negatively influences the magnetic properties of Co_2MnGa.

Overall, all the Co_2MnGa samples showed ferromagnetic behaviour at 300K, with a decrease in M_S compared to the 10K magnetic hysteresis loops of approximately 34% on average, with 47% being the largest decrease for PLD116_01 and 17% being the smallest decrease for PLD116_02.

Sample	T_S (°C)	10K					300K				
		M_S (μ_B/f.u.)	M_R (μ_B/f.u.)	H_C (KOe)		M_R/M_S	M_S (μ_B/f.u.)	M_R (μ_B/f.u.)	H_C (KOe)		M_R/M_S
PLD115_02	450	7.94	4.65	-50.2	50.2	0.59	5.88	4.38	-10.2	10.1	0.74
PLD115_03	450/700	6.02	2.31	-186.8	169.9	0.38	3.22	2.17	-73.3	74.1	0.67
PLD116_01	700	1.97	0.43	-654.6	654.9	0.22	1.05	0.05	-64.8	65.5	0.05
PLD116_02	450	3.50	2.13	-163.6	163.2	0.61	2.92	1.42	-34.2	33.6	0.49
PLD116_03	450/700	3.60	0.93	-453.0	452.6	0.26	2.29	0.16	-74.8	74.9	0.07

Table 5.6: Summary of the substrate growth temperature and magnetic properties of Co_2MnSi grown on MgO and GaAs. The sample name PLD115 and PLD116 relates to thin films grown on MgO and GaAs respectively.

5.6 Summary

The physical and magnetic properties of a combination of single layer and bi-layer Co_2MnGa thin films were investigated to determine whether a buffer layer of material improved the deposited crystal structure of the films. A combination of *in-situ* RHEED and SEM images determined that all the samples had produced epitaxial films for both MgO and GaAs substrates. Films grown on GaAs in particular were suggested to be of a higher crystalline

quality due to the presence of Kikuchi diffraction lines in some RHEED images, which included the sample with a buffer layer between the film and substrate.

X-ray diffraction images resolved superlattice (200) Co_2MnGa peaks and fundamental (400) Co_2MnGa peaks in each of the films with varying intensities. Every sample possessed film strain and the buffer layer films on MgO and GaAs were characterised as possessing the least peak strain relative to bulk Co_2MnGa.

The maximum M_S found at 10K for each substrate was 6.02±3.01 μ_B/f.u. and 3.60±0.77 μ_B/f.u. for MgO and GaAs respectively. The M_S values of the Co_2MnGa thin films grown on GaAs agreed within uncertainty with the theoretically predicted Co_2MnGa magnetic moment of 4.06 μB/f.u. and agreed with other Ms values published in literature which range from 3.2 – 3.5 μ_B/f.u. The Co_2MnGa thin films grown on MgO did not agree due to the systematic error associated with determining the thickness of the film from RBS values which was approximately 33 – 50%. This large error resulted in an overstated value for the magnetic moment of Co_2MnGa.

The growth parameters which produced the highest M_S values were found to be the thin films grown at 450°C for both MgO and GaAs. The variance of the M_S value did not appear to be very sensitive to fluence, but a film on the order of ~50nm thick was necessary to produce reliable M_S results.

Conclusion

The main goal of this thesis was to establish some of the parameters for successful pulsed laser deposition (PLD) of two half-metallic thin film Heusler alloys, Co_2MnSi and Co_2MnGa. Laser fluence, substrate choice and substrate growth temperature were varied to produce a variety of thin films to investigate the physical characterisation and magnetic properties of these two materials. The main conclusions are presented including ideas to extend and improve this work.

Chapter 1 and 2 discussed the importance of half-metallic thin film Heusler alloys for future spintronic devices in the electronic industry. The nature of 100% polarisation of the density of states at E_F outlined the importance of the high Curie temperatures and crystal structure ordering of these materials for use in room temperature devices. Co_2MnSi and Co_2MnGa are sensitive to crystal disorder and require thin films structured with $L2_1$ order to preserve the strong ferromagnetic behaviour and the half-metallic state.

The use of the PLD thin film growth technique, various instruments and processes for the analysis of the physical and magnetic properties of Co_2MnSi and Co_2MnGa thin films were presented in chapter 3.

Thin films of Co_2MnSi grown on MgO and GaAs substrates were investigated in detail in chapter 4. Evidence from *in-situ* RHEED imaging and SEM images demonstrated that quality films required a high growth fluence above 4.5 J/cm² with a substrate temperature of 450°C and above for the deposited growth to align with the crystalline substrate orientation. Films grown at 200°C were amorphous with low fluence and polycrystalline with high fluence. The 0.02% lattice mismatch between Co_2MnSi and GaAs caused the XRD sample and substrate peaks to be un-resolvable for the superlattice (200) and fundamental (400) peaks. These reflections were resolvable for films grown on MgO for PLD105_07, a sample grown at 700°C with a fluence of 4.57±0.28 J/cm², which demonstrates a highly aligned single crystal structure. For all the films, the intensity of the fundamental (400) peak was stronger than the superlattice (200) peak. This feature is associated with Heusler thin films

orientated in a B2 crystal structure which have disordered Mn and Si atoms in the diffracting plane.

The maximum M_S found at 10K for each substrate was 4.65±0.83 μ_B/f.u. and 3.54±1.36 μ_B/f.u. for MgO and GaAs respectively The MgO value agrees within uncertainty with the theoretically predicted Co_2MnSi magnetic moment of 5.07 μ_B/f.u., whereas Co_2MnSi on GaAs is 3% lower than this value. Both results agree with other M_S values published in the literature which range from 4.95 – 5.10 μ_B/f.u. In general, M_S was the largest for Co_2MnSi thin films grown on MgO substrates and lowest for thin films grown on GaAs substrates.

The temperature dependent resistivity of the Co_2MnSi grown on MgO and GaAs was investigated from 10K to 300K. The general trend confirmed these thin films exhibit ferromagnetic behaviour as the resistivity monotonically increases with temperature. The general equation describing the resistivity behaviour of a metal was compared to the temperature dependent data. Observing different variations of the equation confirmed that including a term for the spin flips with a parameter for the energy gap in the minority state was necessary to produce a good fit to the Co_2MnSi data. This evidence supports the half-metallic nature of Co_2MnSi.

A combination of single layer and bi-layer Co_2MnGa thin films were grown using PLD to investigate whether a buffer layer of material improved the deposited crystal structure. The physical and magnetic properties of the films were presented in chapter 5. *In-situ* RHEED imaging and SEM images showed that all the samples were epitaxial films for both MgO and GaAs substrates. Films grown on GaAs appeared to possess a higher crystalline quality due to the presence of Kikuchi diffraction lines in some RHEED images, which are associated with long range crystal order. This included samples with a buffer layer deposited between the film and substrate. Kikuchi diffraction lines for the bi-layer films are most likely an effect attributed to the high 700°C substrate temperature during growth of the main film layer, not the influence of the buffer layer on the relaxation of the film. X-ray diffraction images resolved fundamental (400) and superlattice (200) Co_2MnGa peaks in each of the films with varying intensity. This suggests the epitaxial films are orientated as highly aligned single crystals. The sample with the least strain relative to bulk Co_2MnGa was

the buffer layer film, PLD115_03 grown on MgO. Most likely the thin films in this series are also ordered in a B2 crystal structure.

Growth parameters for both series agree that a fluence of 4.79 – 7.06 J/cm² and a minimum 450°C substrate growth temperature can produce films ranging from 65 - 153nm in thickness. Film thickness can easily be improved by increasing growth time or increasing growth rate by using a higher fluence. The disadvantage of increasing the fluence was highlighted in the SEM images of both Co_2MnSi and Co_2MnGa. Films grown using a high fluence value such as ~5 J/cm² were very heavily particulated in contrast to the heavily reduced population of particulates for films grown at a fluence below ~3.5 J/cm². Heavily particulated film surfaces are highly undesirable as they negatively affect devices at the surface interface.

The maximum M_S found at 10K for each substrate was 6.02±3.01 μ_B/f.u. and 3.60±0.77 μ_B/f.u. for MgO and GaAs respectively. The M_S values of the Co_2MnGa thin films grown on GaAs agreed within uncertainty with the theoretically predicted Co_2MnGa magnetic moment of 4.06 μB/f.u. and agreed with other Ms values published in literature which ranged from 3.2 – 3.5 μ_B/f.u. The Co_2MnGa thin films grown on MgO did not agree due to the systematic error associated with determining the thickness of the film from RBS values which was approximately 33 – 50%. This large error resulted in an overstated value for the magnetic moment of Co_2MnGa.

PLD successfully produced stoichiometric thin films ranging from 11±10nm to 153±10nm thick. A minimum growth temperature of 450°C was necessary to produce epitaxially deposited thin films for both materials. Co_2MnSi thin films required at least 4.5 J/cm² during growth to produce films with optimal structural and magnetic properties, whereas the properties of the Co_2MnGa thin films did not appear to be very sensitive to fluence.

XRD results suggest the films may be orientated as B2 crystal structure, not $L2_1$ as there are no strong (111), (220), (311) or (331) peaks present for any of the samples. It is possible an unresolved (220) peak at 45° may have been present for the PLD115 series of Co_2MnGa on MgO, however the proximity of the Ag surface contacts and MgO substrate peaks at ~44.6° and ~45.4° respectively hinder any clear evidence.

The magnetisation of both materials was strongest for films grown on 450°C. A reduction of the M_S values measured at 300K relative to 10K was observed to be 23% for Co_2MnSi and 34% for Co_2MnGa. In some cases, the magnetisation was unable to be accurately determined due to the thickness uncertainty on the thinnest (≤30nm thick) films. Two thin films grown on MgO in the Co_2MnGa series should also be subjected to the same caution due to their associated thickness uncertainties. Unfortunately PLD115_01, with a sample thickness of 68±10nm, was not measured. The samples, PLD115_03 and PLD116_03, included a buffer layer equivalent to ~20% of the main layer thickness which was grown at 450°C. The main layer however, was grown at 700°C, and this layer contributes to the majority of the deposited sample. As such this buffer layer combination resulted in M_S values between those of the single layer films grown at 450°C and 700°C and hence did not improve on the magnetic moment of the optimally prepared single layer thin film samples of Co_2MnGa.

In summary, thin films of Co_2MnSi and Co_2MnGa were successfully produced using PLD to be of a good quality from *in-situ* RHEED, SEM and XRD observations. XRD evidence suggests the structure of the films were orientated in B2 order, not $L2_1$. The magnetic properties revealed ferromagnetic behaviour for all the samples in both series by the characteristic magnetic hysteresis loop shape. This is consistent with the expected high Curie temperatures of these materials, which are on the order of 600K and 900K for Co_2MnGa and Co_2MnSi, as the reduction of the M_S of Co_2MnGa at 300K from 10K was larger than the reduction for Co_2MnSi. Each sample produced M_S values which agreed with the theoretical bulk values for each series, despite large errors originating from the RBS thickness measurement for the thinnest samples.

Future work emphasises the need for films at least ~60nm thick and a broader range of substrate growth temperatures at values above 450°C to further characterise the physical and magnetic properties of these films.

Appendix A: Calculating laser fluence

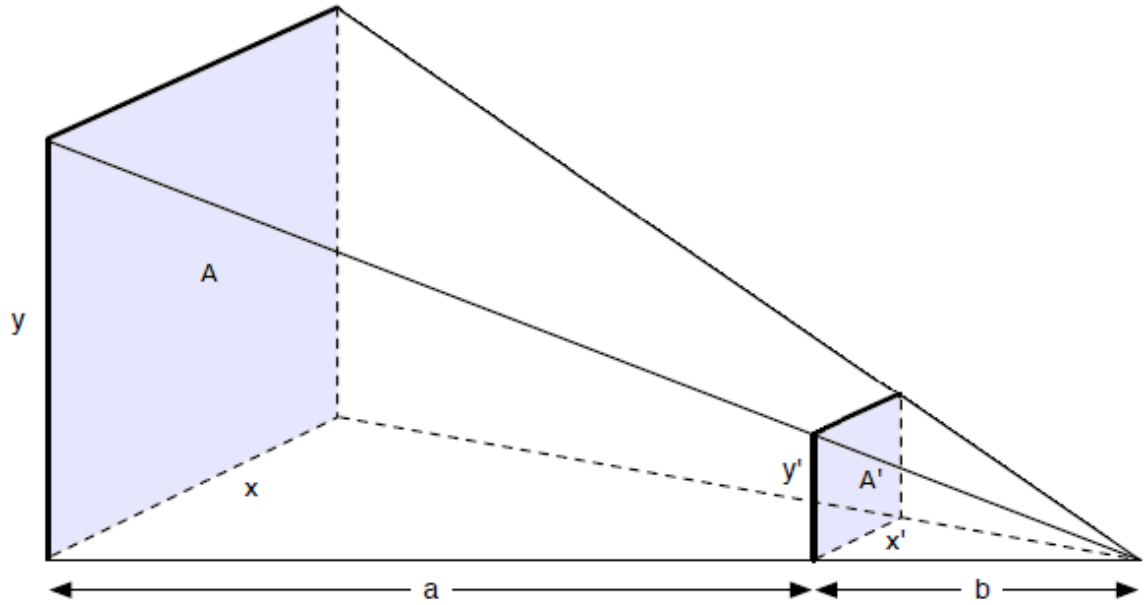

Fig A1: Geometry used to calculate the fluence at the target.

The focal length of the laser is:

$$f = a + b \qquad \text{Equation A1}$$

The fluence of the laser (in J/cm²) is given by the equation:

$$F = \frac{E_L \tau}{A} \qquad \text{Equation A2}$$

where E_L is the energy of the laser (J), τ represents the transmission of the optics and including all mirrors, lenses and the chamber laser window. A is the area of the laser beam at the lens (cm²). Using the geometry in fig A1, area is equivalent to xy. Including this factor, the transmitted laser fluence is:

$$F = \frac{E_L \tau}{xy} \qquad \text{Equation A3}$$

The laser undergoes a projection before it reaches the UHV chamber to reduce to the laser spot on the target. The area of the beam before the projection, A' from the geometry of fig A1 is equivalent to x'y', therefore the area of the beam after the projection is:

$$xy = \frac{x'y'}{sin\theta} \qquad \text{Equation A4}$$

To determine the desired fluence the position of the lens must also be determined. Equation A1 is used to find a, and b is determined by the chamber geometry depending on the desired stage height of the target.

Using the law of similar triangles, the angle between x' and b is equal to the angle between x and a + b (or f). As such equation A1 can be written as:

$$x' = \frac{xb}{f} \quad \text{or} \quad y' = \frac{yb}{f}$$

Multiplying the equations above obtains:

$$x'y' = \frac{xyb^2}{f^2} \qquad \text{Equation A5}$$

To determine the fluence after the laser has undergone the projection, equation A4 can be substituted into equation A3 to obtain:

$$F_{(target)} = \frac{E_L sin\theta\tau}{x'y'} \qquad \text{Equation A6}$$

Substituting equation A5 into equation A6 gives:

$$F_{(target)} = \frac{E_L sin\theta\ f^2\tau}{xyb}$$

Each of these parameters were measured and listed in order of sample series in table A1.

Sample	Growth time (hr)	Laser mode	V (kV)	E (J)	Window to lens distance (cm)	Target distance (inches)	Substrate distance (inches)	Transmission (%)	Fluence (J/cm²)	Fluence uncertainty (J/cm²)
PLD105_03	1	EGY NGR	21.4	0.196	9.1	0.6	1.265	46.30	3.28	0.23
PLD105_04	1	EGY NGR	-	0.200	9.2	0.6	1.265	33.30	2.60	0.21
PLD105_05	1	EGY NGR	-	0.200	9.2	0.6	1.265	30.05	2.35	0.20
PLD105_06	1	HV	27.0	0.184	9.3	0.6	1.265	83.63	6.50	0.38
PLD105_07	1	HV	27.0	0.140	9.3	0.6	1.265	77.26	4.57	0.28
PLD105_08	1	EGY NGR	21.3	0.184	9.2	0.6	1.265	70.88	5.09	0.31
PLD105_09	2	EGY NGR	-	0.200	9.3	0.6	1.365	77.26	6.53	0.39
PLD107_01	1	EGY NGR	21.5	0.196	9.1	0.6	1.265	49.55	3.51	0.24
PLD107_02	1	EGY NGR	22.3	0.200	9.0	0.6	1.272	39.80	2.68	0.20
PLD107_03	1	EGY NGR	22.3	0.200	9.1	0.6	1.265	36.55	2.65	0.21
PLD107_04	1	EGY NGR	22.0	0.200	9.3	0.6	1.265	51.77	4.37	0.30
PLD107_05	2	EGY NGR	21.5	0.200	9.3	0.6	1.265	83.63	7.06	0.41
PLD115_01	1	EGY NGR	21.8	0.190	9.3	0.6	1.265	64.51	5.18	0.33
PLD115_02	1	EGY NGR	24.3	0.200	9.3	0.6	1.265	32.65	2.76	0.22
PLD115_03	0.2/1	HV	26.5	0.176	9.3	0.6	1.265	26.27	1.95	0.18
PLD116_01	1	EGY NGR	-	0.195	9.3	0.6	1.265	58.14	4.79	0.31
PLD116_02	1	EGY NGR	24.4	0.200	9.3	0.6	1.265	39.02	3.30	0.249
PLD116_03	0.2/2	EGY NGR	21.7	0.210	9.3	0.6	1.365	70.88	6.29	0.38

Table A1: Parameters used to determine the value of the fluence at the target for each sample.

HV mode varies the voltage to produce the desired output of laser energy at a fixed value. EGY-NGR mode sets the voltage to a constant value to produce the laser energy, the output energy decreases during growth as the laser gas depletes.

References

[1] Business Standard reporter, “Spintronics: The Answer to Moore’s Law”, *The Business Standard* (2011), <http://www.business-standard.com/article/ technology/spintronics-the-answer-to-moore-s-law-111070500009_1.html>, [accessed 13 March 2014].

[2] S. A. Wolf, D. D. Awschalom, R. A. Buhrman, J. M. Daughton, S. von Molnár, M. L. Roukes, A. Y. Chtchelkanova, D. M. Treger, “A Spin-Based Electronics Vision for the Future”, *Science New Series*, Vol. 294, No. 5546 (2001), pp.1288-1495.

[3] L Sigh, “Co_2MnSi Heusler Alloy Thin Films”, (PhD Thesis, Cambridge University, 2005).

[4] S. F. Cheng, B. Nadgorny, K. Bussmann, “Growth and Magnetic Properties of Single Crystal Co_2MnX (X=Si, Ge) Heusler Alloys”, *IEEE Transactions on Magnetics*, Vol. 37, No. 4, (2001), pp.2176-2178.

[5] M. Belmeguenai, F. Zighem, G. Woltersdorf, Y. Roussigne, S. Cherif, K. Westerholt, G. Bayreuther, “Anisotropy and Dynamic Properties of Co_2MnGe Heusler Thin Films”, *Journal of Magnetism and Magnetic Materials*, Vol. 321 (2009) pp.750–753.

[6] U. Geiersbach, A. Bergmann, K. Westerholt,” Structural, Magnetic and Magnetotransport Properties of Thin Films of the Heusler Alloys Cu_2MnAl, Co_2MnSi, Co_2MnGe and Co_2MnSn”, *Journal of Magnetism and Magnetic Materials*, Vol. 240 (2002), pp. 546–549.

[7] N. Ghaderi et al. “First Principle Study of Co_2MnSi/GaAs(001) heterostructures”, Journal *of Applied Physics*, Vol 102.7 (Oct. 2007).

[8] T. Graf, C. Felser, S. Parkin, “Simple Rules for the Understanding of Heusler Compounds”, *Progress in solid state chemistry*, Vol. 39 (2011) pp1-50.

[9] W. H. Wang et al.”Magnetic and Transport Properties of Epitaxial Co_2MnSi films”, *IEEE Transactions on Magnetics*, Vol. 41.10 (Oct. 2005), pp. 2805-2807.

[10] P J Brown, K U Neumann, P J Webster and K R A Ziebeck, “The Magnetization Distributions in some Heusler Alloys Proposed as Half-Metallic Ferromagnets”, *Journal of Condensed Matter*, Vol. 12 (2000) pp. 1827–1835.

[11] S Kämmerer, “The Heusler alloy Co2MnSi in thin films”, (PhD Thesis, Bielefeld University 2004).

[12] T. Graf, C. Felser, S. Parkin. “Heusler Compounds—A Material Class With Exceptional Properties”, IEEE transactions on magnetic, Vol 47 (2011).

[13] S. Ishida et al. “Theoretical Predictions of Half-Metallic Compounds with the C1b Structure”, *Physica B: Condensed matter*, Vol 239.1-2 (1997), pp. 163-166.

[14] M. Kolbe, S. Chadov, E. Arbelo Jorge, G. Schönhense, C. Felser, H. Elmers, M. Kläui, and M. Jourdan, “Test of Band Structure Calculations for Heusler Compounds by Spin-Resolved Photoemission Spectroscopy”, *Physical review B*, Vol.86, (2012).

[15] M. Obaida, K.Westerholt, H. Zabel, “Magnetotransport Properties of Cu_2MnAl, Co_2MnGe and Co_2MnSi Heusler Alloy Thin Films: from Nanocrystalline Disordered State to Long- Range-Ordered Crystalline State”, *Physical Review B,*Vol 84 (2011), pp 1 – 11.

[16] G E Bacon and J S Plant, “Chemical Ordering in Heusler alloys with the General Formula A2BC or ABC”, *Journal of Metal Physics F, Vol. 1 (1971).*

[17] S. Picozzi, A. Continenza, and A. J. Freeman, “Role of Structural Defects on the Half-Metallic Character of Co_2MnGe and Co_2MnSi Heusler Alloys, *Physics Review B*, Vol 69 (2004).

[18] D. Orgassa, H. Fujiwara, T. C. Schulthess, and W. H. Butler, “First-principles Calculation of the Effect of Atomic Disorder on the Electronic Structure of the Half-Metallic Ferromagnet NiMnSb”, *Physics Review B*, Vol 60 (1999).

[19] C. Grigorescu,, E. Valerio, L. Tortet, R. Notonier, H.J. Trodahl, V.J. Kennedy, A. Markwitz, S.A. Manea, M. Autric, “Co_2MnX (X=Si, Ge, Sn, SbSn) Thin Films Grown by Pulsed Laser Deposition”, *Journal of Crystal Growth*, Vol. 275 (2005), pp.1183–1188.

[20] J. Dubowik, Y. V. Kudryavtsev, V. A. Oksenenko, Y. P. Lee, Y. H. Hyun, J. B. Kim, J. S. Park, and S. Y. Park, "Evolution of the Magnetic Properties of Co_2MnGa Heusler Alloy Films: From Amorphous to Ordered Films", *Physical review,* Vol. 76 (2007).

[21] M. Hahn, G. Schönhense, E. A. Jorge, M. Jourdan, "Significant Spin Polarization of Co_2MnGa Heusler Thin Films on MgO(100) Measured by Ultraviolet Photoemission Spectroscopy", *Applied Physics Letters*, Vol. 98 (2011) pp. 1-3.

[22] D. Dijkkamp, T. Venkatesan, X. D. Wu, S. A. Shaheen, N. Jisrawi, Y. H. Min-Lee, L. McLean, M. Croft, Applied Physics Letters 51, 619 (1987).

[23] I. Farrell, Growth of metal-nitride thin films by pulsed laser deposition, Ph.D Thesis, University of Canterbury (2010).

[24] R. Mendelsberg, "Photoluminescence of ZnO grown by eclipse Pulsed Laser Deposition", (PhD, University of Canterbury, 2009).

[25] Diagrams from UHV chamber blueprints designed by Thermioncs for Canterbury University.

[26] G Wang, Y Liu, C Gaire, W Yuan and T-M Lu. "RHEED Pole Figure Measurements of Biaxial Thin Film Growth Front Evolution". *MRS Proceedings*, Vol. 1308, (2011).

[27] M. Mayer, "Rutherford Backscattering Spectrometry (RBS)", (Max-Planck-Institute of Physics, 2003)

[28] M. McElfresh, "Fundamentals of Magnetism and Magnetic Measurements: Featuring Quantum Designs Magnetic Property Measurement System", Quantum Design (1994) p.8

[29] A. Hyndman, "Growth of Thin Films by Pulsed Laser Deposition for Applications in Spin Transport Electronics", (MSc, Canterbury University, 2009).

[30] "Physical Property Measurement System: Resistivity Option User's Manual", Quantum Design (1999)

[31]: N. Dilley, "Quantum Design Electrical Transport User Training Seminar part 2: Experimental Design", Quantum Design (2011)

[32] “Performing Van Der Pauw Resistivity Measurements”, Quantum design, application note 1076-304 (2007)

[33] G. Wolf, J. Hamrle, S. Trudel, T. Kubota, Y. Ando, B. Hillebrands, “Quadratic Magneto-Optical Kerr Effect in Co_2MnSi”, *Journal of applied physics*, Vol. 110 (2011).

[34] G. Li, E. Liu, Y. Zhang, Y. Du, H. Zhang, W. Wang, G. Wu, “Structure, Magnetism, and Magnetic Compensation Behaviour of Co_2MnGa Heusler alloys”, *Journal of applied physics*, Vol. 113 (2013).

[35] A.S. Manea, O. Monnereau, R. Notonier, F. Guinneton, C. Logofatu, L. Tortet, A. Garnier, M. Mitrea, C. Negrila, W. Branford, C. Grigorescu, “Heusler Bulk Materials as Targets for Pulsed Laser Deposition Growth and Characterisation”, *Journal of Crystal Growth,* Vol. 275 (2005) pp1787–1792.

[36] D. Bombor, C. Blum, O. Volkonskiy, S. Rodan, S. Wurmehl, C. Hess, B. Büchner, “Half-Metallic Ferromagnetism with Unexpectedly Small Spin Splitting in the Heusler Compound Co_2FeSi”, *Physical review letters*, Vol. 110 (2013).

[37] S. Hashemifar, P. Kratzer, M. Scheffler, “Preserving the Half-Metallicity at the Heusler Alloy Co2MnSi_001_ Surface: A Density Functional Theory Study”, *Physical review letters*, Vol. 94 (2005).

[38] Dr S. Granville, private communication.

[39] T. Ambrose and O. Mryasov, “Growth and Magnetotransport Properties of Thin Co_2MnGe Layered Structures”, Half-Metallic Alloys: Fundamentals and Applications (2005), pp 187-220.

[40] M. Raphael, B. Ravel, M. Willard, S. Cheng, B. Das et al., “Magnetic, Structural, and Transport Properties of Thin Film and Single Crystal Co_2MnSi”, *Applied physics letters,* Vol.79 (2001).